

Universidade de São Paulo
Instituto de Física de São Carlos
Departamento de Física e Ciência dos Materiais

TÓPICOS EM CRESCIMENTO DE CRISTAIS

USP/IFSC/SBI



8-2-001409

Antonio Carlos Hernandes

Trabalho apresentado ao
Instituto de Física de São Carlos
para o Concurso de Livre-Docência.

São Carlos, SP, março/2001.

A minha família de coração.

Agradecimentos

Difícil agradecer a todos nominalmente, especialmente, nessa fase de minha vida, em que os trabalhos realizados e as novas experiências de vida foram compartilhadas com um grande número de pessoas queridas. Mas, sem a presença dos alunos, pessoal técnico e administrativo e colegas pesquisadores nada disso seria possível. Assim, a todos, o meu muito obrigado.

Também não posso deixar de registrar meus agradecimentos às agências de fomento FAPESP, CNPq, FINEP e CAPES pelos auxílios financeiros.

Minha gratidão especial vai para minha família, pela compreensão e paciência, durante todos esses anos de dedicação ao meu trabalho.

RESUMO

O presente trabalho mostra parte das pesquisas desenvolvidas pelo autor nos últimos anos, no Grupo Crescimento de Cristais e Materiais Cerâmicos, do Instituto de Física de São Carlos, USP. O trabalho aborda os aspectos experimentais de solidificação direcional, puxamento de cristais e crescimento de cristais a partir de uma solução. As publicações consideradas mais representativas em cada tópico são parte integrante desse trabalho, como uma forma de sistematizar os resultados alcançados.

ABSTRACT

The present work shows several researches performed by the author during the last years in the Ceramic Materials and Crystal Growth Group of the Institute of Physics of Sao Carlos, USP. The work reports experimental aspects on directional solidification, crystal pulling and growth of crystal by solution. The most representative papers published about crystal growing processes and properties are attached.

ÍNDICE

AGRADECIMENTOS	i
RESUMO	ii
ABSTRACT	iii
1. Introdução	1
2. Técnicas de crescimento de cristais implantadas no IFSC	5
2.1 A técnica de solidificação direcional com aquecimento a laser	7
2.2 Técnica de evaporação controlada do solvente	11
3. Puxamento de cristais	14
3.1 A técnica Czochralski	15
3.2 Taxa de puxamento do cristal	18
3.3 Forma da interface	21
3.4 Artigo: Large $\text{Bi}_{12}\text{TiO}_{20}$ single crystals: a study of intrinsic defects and growth parameters	25
3.5 Artigo: Synthesis, crystal growth and characterization of γ -phase bismuth titanium oxide with gallium	31
3.6 Artigo: $\text{Yb}^{2+}/\text{CN}^-$ doped KBr absorption and emission structure	36
3.7 Artigo: Optical and ESR study of Er^{3+} in LiNbO_3	43

4. Solidificação direcional com aquecimento a laser	48
4.1 Artigo: Dielectric crystal growth for devices applications	54
4.2 Artigo: Growth of single crystal photorefractive fibers of $\text{Bi}_{12}\text{SiO}_{20}$ and $\text{Bi}_{12}\text{TiO}_{20}$ by the laser-heated pedestal growth method	68
4.3 Artigo: Laser heated pedestal growth of orthorhombic SrHfO_3 single crystal fiber	75
5. Solidificação direcional pela técnica de Bridgman	79
5.1 Artigo: Tellurium-rich phase in n-type bismuth telluride crystals grown by the Bridgman technique	82
5.2 Artigo: Growth and characterization of HgI_2 , PbI_2 and $\text{PbI}_2:\text{HgI}_2$ layered semiconductors	90
6. Crescimento de cristais a partir de solução	95
6.1 Artigo: LAP single crystals growth free of micro-organisms by accurately controlled solvent evaporation technique	98
6.2 Artigo: Control of the concentration gradient during crystal growth from solution	103
6.3 Artigo: Preparação de monocrristais de TGS por solução aquosa	107
6.4 Artigo: Growth and homogeneity of Cr^{3+} doped GdAlO_3 single crystals	110
7. Trabalhos de pesquisa em andamento	116
8. Conclusões	121

CAPÍTULO 1

INTRODUÇÃO

I. INTRODUÇÃO

O objetivo desse trabalho é apresentar de modo sistematizado os resultados alcançados em crescimento de cristais nos laboratórios sob nossa coordenação. Essencialmente, o trabalho aborda os aspectos experimentais de solidificação direcional, puxamento de cristais a partir de uma fase líquida e o crescimento de cristais a partir de uma solução.

Crescimento de cristal é um termo geral que representa um processo de obtenção de uma fase sólida, com átomos organizados geometricamente em determinadas redes tridimensionais, sujeitos a interações de longo alcance, a partir de uma fase de origem (líquido, vapor ou sólido). Nesse trabalho, no entanto, estaremos tratando somente de materiais monocristalinos obtidos a partir de uma fase líquida. Denominamos monocristalino um sólido que apresenta somente um único grão do material.

É importante, para a preparação de um material cristalino, o conhecimento de seu diagrama de fases de equilíbrio. Naturalmente, o crescimento de cristal não acontece em equilíbrio termodinâmico, mas a partir dessas informações podemos analisar a sua viabilidade e quais os parâmetros macroscópicos que deverão ser mais precisamente controlados para otimizar os processos.

O problema associado ao processo de crescimento de cristal é a determinação dos mecanismos responsáveis pela incorporação dos átomos (moléculas ou íons) na interface cristalina. Em outras palavras, precisamos saber o modo de crescimento e a velocidade a partir do ponto de vista atômico. Isto requer, a princípio, a determinação da morfologia da interface da face cristalina a ser crescida.

[A física de crescimento de cristais pode ser didaticamente dividida em dois estágios: a *nucleação* (*precursora do processo de cristalização*) e o *próprio crescimento da nova fase sólida*.]

A nucleação designa um conjunto de processos que conduz à formação de uma nova fase estável dentro de uma fase de origem instável. Gibbs foi o primeiro a compreender que a formação de pequenos aglomerados com algum tamanho crítico era um pré-requisito para ocorrer uma transformação de fase macroscópica. Estes aglomerados, denominados núcleos críticos, tem uma probabilidade de sobreviver e produzir entidades macroscópicas da nova fase somente em sistemas longe do equilíbrio (supersaturados ou superresfriados). Logo, a nucleação de uma nova fase é um processo descontínuo.

[O crescimento de um cristal é um processo dinâmico e envolve uma troca recíproca de átomos, ou moléculas, ou íons entre a fase cristalina e a fase de origem. No equilíbrio termodinâmico, o balanço efetivo desta troca é zero, ou seja, uma fase não cresce em relação à outra. Para que o crescimento possa ocorrer este equilíbrio deve ser perturbado por uma mudança controlada em uma ou em mais variáveis termodinâmica do processo, como por exemplo, temperatura, pressão, concentração, campo elétrico, etc. Nessa condição de “quase-equilíbrio” o sistema então pode trocar energia com sua vizinhança para compensar a diminuição da entropia ocasionada pelo ordenamento das unidades de crescimento no cristal com a liberação do calor de cristalização. Crescer um cristal é, então, uma ação controlada, e cuidadosa, de uma transição de fase de primeira ordem. O processo deve ser mantido tão próximo do equilíbrio e do estado estacionário quanto possível uma vez que, controlar o ambiente do processo de crescimento e as considerações de cinética, a níveis macroscópicos e microscópicos, é de vital importância para o sucesso de um experimento de obtenção de um monocrystal homogêneo e de alta qualidade estrutural.

No domínio macroscópico de um processo de crescimento as variáveis de estado termodinâmico são fixadas ou alteradas dinamicamente de acordo com um programa particular pré-determinado. É através da otimização dos valores dessas variáveis macroscópicas que os mecanismos microscópicos de crescimentos, na interface do cristal – líquido, são controlados. A estes estão associados todos os fenômenos morfológicos, de segregação, de defeitos estruturais e de composição que surgem num evento de cristalização. O entendimento científico de todo o processo, portanto, requer uma completa descrição em termos das variáveis de estado termodinâmico e de seus gradientes na interface. A conexão entre as condições na interface e as de regiões distantes dela ocorre via um conjunto de equações diferenciais parciais e suas condições de contorno. Simulações computacionais têm possibilitado, recentemente, analisar algumas situações experimentais mais realisticamente desse tratamento teórico.

Uma característica inevitável de um Grupo de Pesquisa que cresce cristais é a forte cooperação científica que se estabelece com outros pesquisadores, particularmente com os que se especializaram em técnicas de caracterização e de medidas de propriedades físicas de materiais e não tiveram contato com o processo de preparação. Nos capítulos posteriores desse trabalho, procurarei evidenciar essa forte cooperação científica.

Bibliografia

- [1] Antonio Carlos Hernandes – “Estudo in situ do perfil de concentração do soluto durante o processo de crescimento e dissolução de monocrystal de $\alpha\text{-HgI}_2$ ”. Tese de doutoramento, IFQSC – USP, 1993.
- [2] Peter Rudolph – “Thermodynamic fundamentals of crystal growth processes”. Lecture Notes, pag. 1, 1999. First Int. School on Crystal Growth and Advanced Materials in Brazil, July 18-23, 1999, Campinas, SP.
- [3] Antonio Carlos Hernandes – “ Fenômenos de segregação em crescimento de cristais”, I Escola de Verão em Crescimento de Cristais, 1997, IPEN, SP.

CAPÍTULO 2

**TÉCNICAS DE CRESCIMENTO DE
CRISTAIS IMPLANTADAS NO IFSC**

II. TÉCNICAS DE CRESCIMENTO DE CRISTAIS/IFSC

Diversas técnicas para a produção de cristais foram por nós implantadas nesse período em nossos laboratórios, como a técnica de Bridgman para crescimento de cristais semicondutores com estrutura cristalina em camadas, a Top Seed Solution Growth – TSSG – para o desenvolvimento do projeto de produção de cristais fotorrefrativos, a Czochralski com aquecimento resistivo de platina para obtenção de cristais óxidos. No entanto, as duas mais importantes foram a de solidificação direcional com aquecimento a laser e a técnica de evaporação controlada do solvente.

A tecnologia laser vem sendo empregada há muito anos no processamento de diversos materiais. As características que fazem da radiação laser atrativa para este propósito são a coerência e a colimação, que permitem ajustar a distribuição de energia com elementos ópticos convencionais. No estágio atual, nós aplicamos a tecnologia laser para: solidificação direcional aplicada ao crescimento de fibras monocristalinas e a produção de materiais eutéticos, cristalização superficial e texturização em materiais vítreos, desenvolvimento e desenho de componentes ópticos em vidros transparentes na região do visível e na sinterização de cerâmicas.

A técnica de evaporação controlada do solvente (TECS) foi usada para a produção de cristais de aminoácidos, do tipo L-arginina fosfatada, para o estudo de propriedades ópticas não-lineares. Também implantamos essa técnica no Laboratório de Cristalografia e Materiais, do Instituto de Física de Goiás (IF-UFG) e no Laboratório de Raios-X do Departamento de Física, da Universidade Federal

do Ceará (DF-UFC). Isto permitiu aos pesquisadores dessas instituições a produzir suas próprias amostras.

2.1 – A TÉCNICA DE SOLIDIFICAÇÃO DIRECIONAL COM AQUECIMENTO A LASER

Nosso equipamento, projetado e montado durante a realização do mestrado do estudante Marcello Rubens Barsi Andreatta, sob nossa orientação, é semelhante ao desenvolvido por R. S. Feigelson, no Center for Materials Research, Stanford University; com o qual mantemos cooperação científica. Na oportunidade, o Brasil tornou-se o quinto país a implantar a técnica de solidificação direcional com aquecimento a laser, conhecida como Laser Heated Pedestal Growth - LHPG. Durante este período, centenas de fibras foram produzidas, como: $\text{Bi}_{12}\text{SiO}_{20}$, $\text{Bi}_{12}\text{TiO}_{20}$, LiNbO_3 , LiTaO_3 , Al_2O_3 , GdAlO_3 , BiSrCaCuO , YAlO_3 , $\text{GdAlO}_3/\text{Al}_2\text{O}_3$, SrTiO_3 , ZrO_2 , Sr_2RuO_4 , SrTiO_3 entre outras, puras e dopadas, nas mais diferentes atmosferas de crescimento.

A figura 2.1 mostra em diagrama de blocos a configuração de nosso sistema. O processo de fusão é efetuado focalizando-se sobre o pedestal (nutriente) um feixe de laser de CO_2 (Synrad 57-1; MPB Technologies), operando num comprimento de onda de 10.6 μm continuamente e com potência nominal controlada de 0 a 100 W. A cavidade do laser é refrigerada a água, através de um circuito fechado com controle termostático, a fim de se evitar grandes flutuações na potência nominal de saída. Na maioria dos experimentos de solidificação direcional a temperatura da água é mantida em $(19.0 \pm 0.5)^\circ\text{C}$. Um feixe de laser de He-Ne, propagando-se paralelo ao de infravermelho, é usado

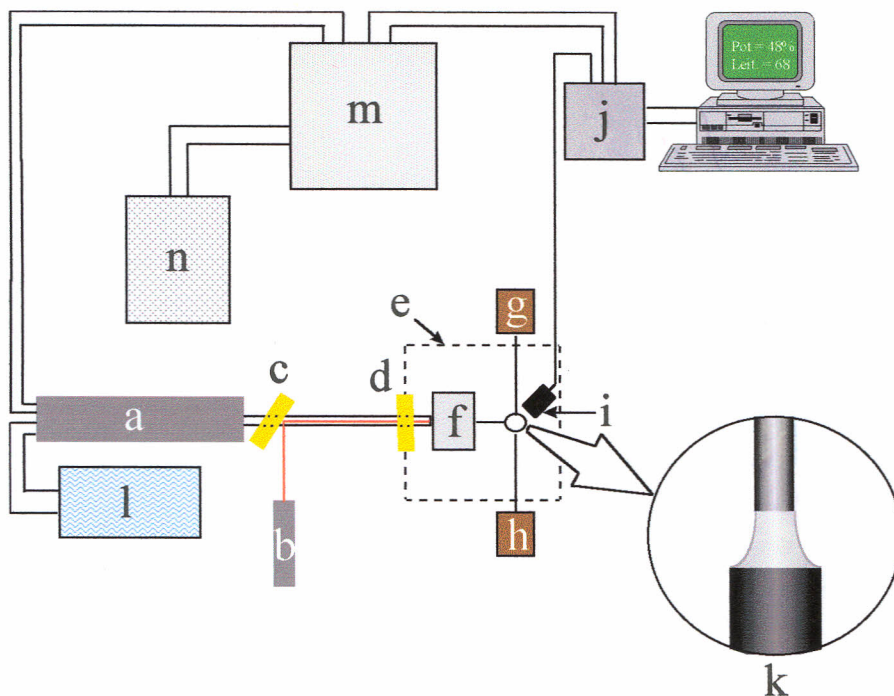


Figura 2.1 - Diagrama de blocos do sistema de solidificação direcional para a produção de fibras monocristalinas por fusão a laser. a - Laser de CO₂, b - Laser de He-Ne, c - Divisor de feixe de ZnSe, d - Janela de ZnSe, e - Câmara de crescimento, f - Sistema de focalização, g e h - Sistema de puxamento da fibra e elevação do pedestal, respectivamente, i - Fototransistor, j - Sistema de controle e estabilização da potência do laser, k - Sistema de visualização via vídeo (zona fundida), l - Sistema de refrigeração do laser de CO₂, m e n - Fontes de RF e alimentação respectivamente.

como guia no alinhamento óptico do sistema. Os feixes dos lasers penetram na câmara de solidificação, construída em aço inoxidável e com possibilidade de controle da atmosfera (gases especiais ou vácuo), através de uma janela de ZnSe e propagam-se diretamente para o sistema de focalização fixado dentro da câmara. Todo o sistema de crescimento é montado sobre uma mesa óptica para eliminar as vibrações mecânicas.

O sistema de focalização consiste de um reflaxicon (dois cones acoplados), um espelho plano e um esférico, figura 2.2. O feixe de CO₂ ao incidir no reflaxicon é convertido de um formato cilíndrico para uma casca cilíndrica. Ao atingir o

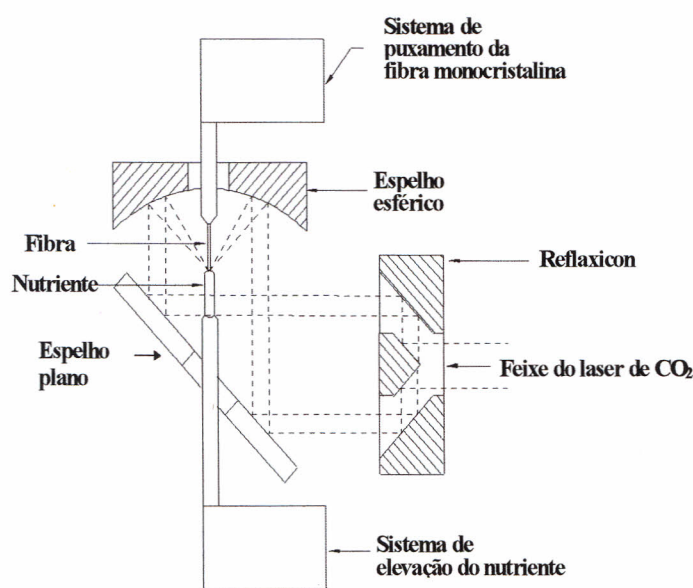
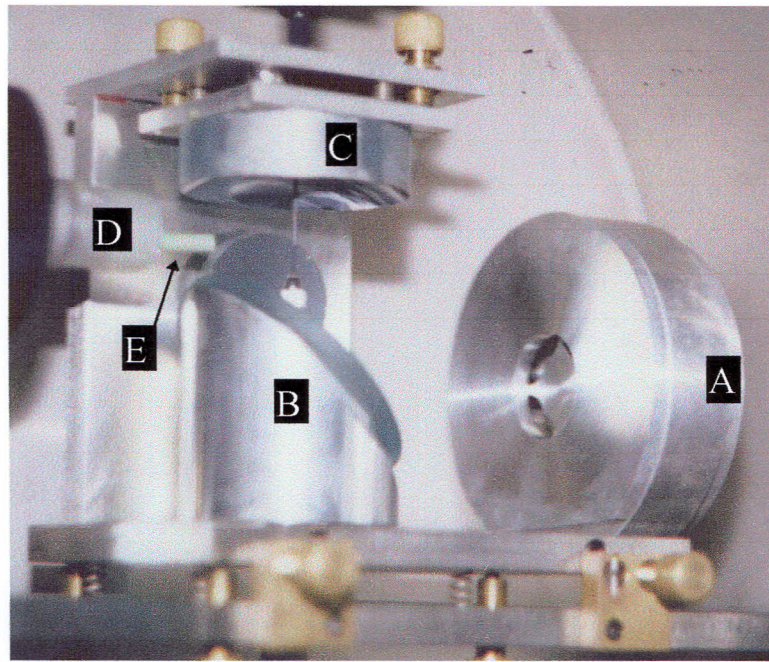


Figura 2.2 - Sistema de focalização fixado dentro da câmara de crescimento de fibras monocristalinas e sua representação esquemática. A - Reflaxicon, B - Espelho plano com furo elíptico posicionado a 45° em relação ao feixe, C - Espelho esférico, D - Objetiva do sistema de visualização, E - Fototransistor.

espelho esférico é, então, focalizado sobre o pedestal, e a zona fundida produzida posicionada em seu eixo óptico. É essencial obter um ótimo alinhamento dos feixes para não gerar na fase líquida elevados gradientes de temperatura radial e, consequentemente, desestabilizar a interface de solidificação.

Algumas das vantagens dessa técnica são as altas velocidades de solidificação, a não utilização de cadiinhos, a visualização da forma da interface sólido-líquido durante o processo de solidificação de materiais transparentes e a pequena quantidade de compostos necessária para a realização de um experimento. A principal desvantagem é que o material a ser produzido deve absorver a radiação do laser usado na fusão.

Duas características intrínsecas da técnica de fusão a laser são:

- *a possibilidade de uso de pedestais extrudados a frio. Nesse caso, três etapas do processo de preparação (síntese, sinterização e solidificação) são reduzidas a uma, economizando-se tempo e, em alguns casos, gerando uma condição única para a obtenção de materiais estequiométricos.*
- *a multidopagem em um único experimento. A figura 2.3 ilustra uma região de uma fibra de $LiNbO_3$ multidopada com Cr_2O_3 , Fe_2O_3 e Eu_2O_3 respectivamente. A principal vantagem deste procedimento é a rapidez com que novos materiais podem ser preparados ou, ainda, a facilidade de se estudar a influência de diferentes dopantes na mesma matriz cristalina.*

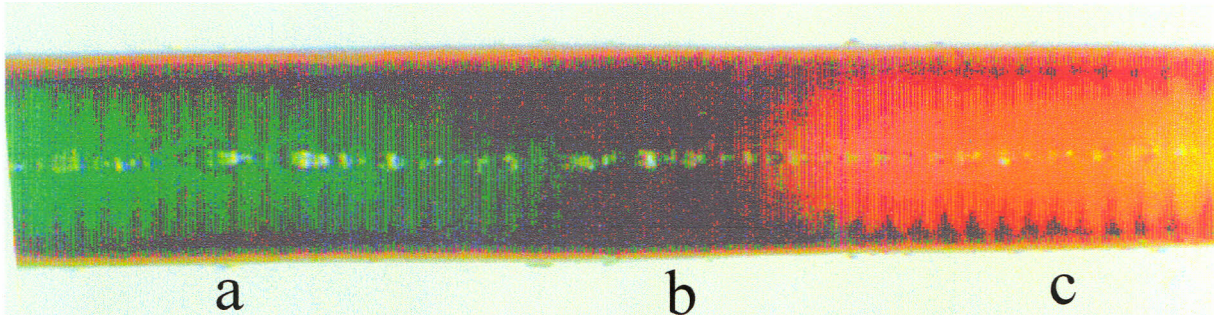


Figura 2.3 - Fotografia da região de uma fibra de LiNbO₃ multidopada com: a) Cr₂O₃, b) Fe₂O₃ e c) Eu₂O₃. A multidopagem foi efetuada através da técnica de “paint-on”.

2.2 - TÉCNICA DE EVAPORAÇÃO CONTROLADA DO SOLVENTE

A técnica de evaporação controlada do solvente, TECS, a temperatura constante, foi por nós desenvolvida e utilizada com sucesso no crescimento de cristais inorgânicos e aminoácidos, durante a realização do mestrado da estudante Liana Bueno Oliveira Amorim de Moraes, sob nossa orientação. Na figura 2.4 apresentamos uma representação esquemática da câmara de crescimento.

Na TECS estabelecemos duas regiões com pressões de vapor diferentes no interior da câmara de crescimento por intermédio da manutenção de temperaturas diferentes nas mesmas. Como o solvente evapora (à temperatura T₁), ele flui para a zona de pressão mais baixa e se condensa sobre as paredes pouco umidificantes (isto é, com elevado ângulo de molhamento) de uma peça cônica cuja temperatura (T₂ < T₁) é mantida por fluxo de água. O solvente condensado desliza pelas paredes do condensador até uma calha na base do cone onde é coletado numa bureta graduada (0.1ml). Controlamos a taxa de evaporação, responsável pela velocidade de crescimento, ajustando a temperatura do cone de condensação.

O baixo custo dessa técnica e a possibilidade de seu uso para a preparação de uma grande variedade de materiais fez com que outros pesquisadores do País e um da Colômbia adquirissem a câmara de crescimento por nós desenvolvida.

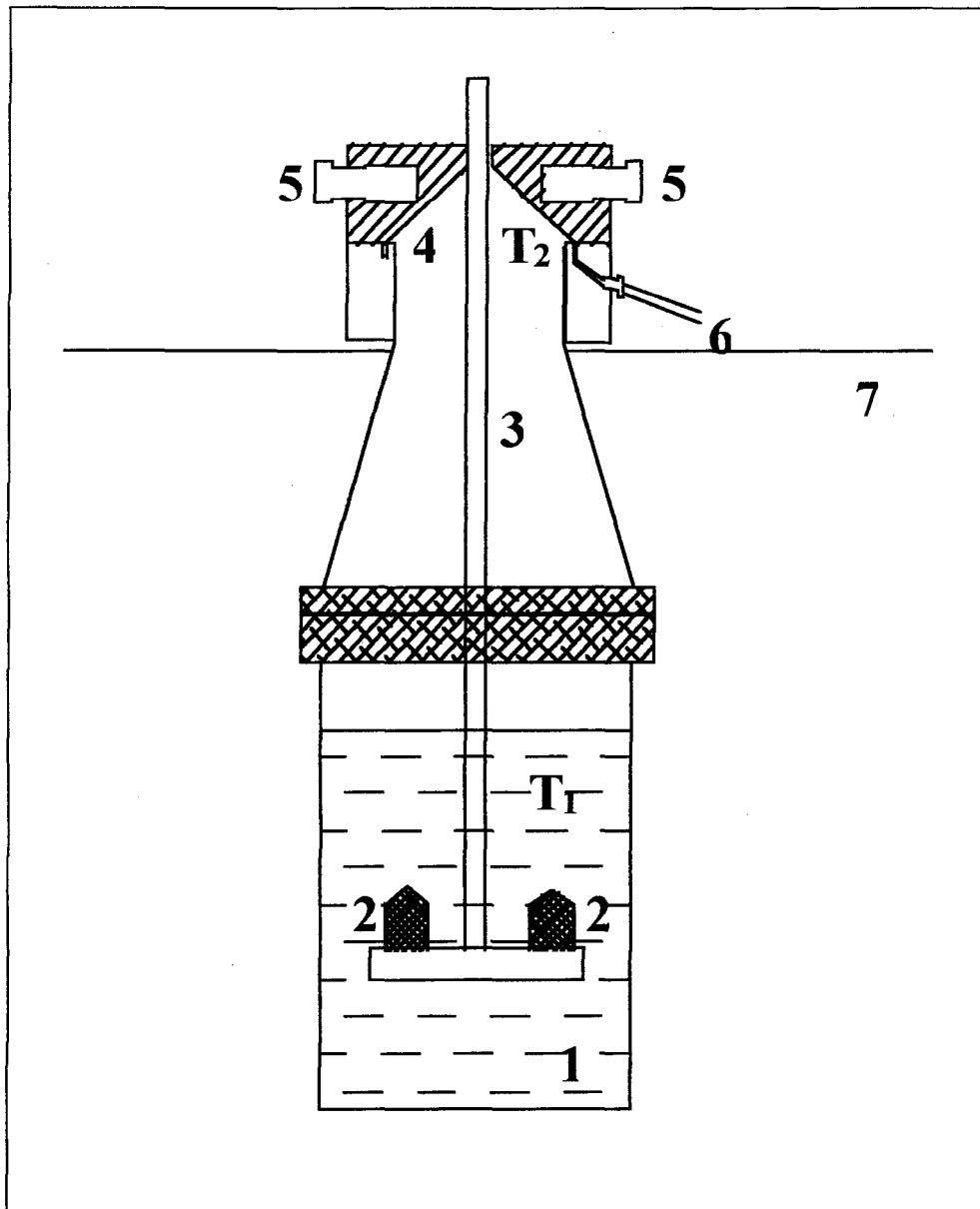


Figura 2.4 – Representação esquemática da câmara de crescimento de cristais por evaporação controlada do solvente. (1)Solução de crescimento, (2)cristal, (3)haste rotatória, (4)cone de condensação, (5)fluxo de água para controle da temperatura do cone, (6)saida de água para a bureta, (7)nível de água do banho térmico.

Bibliografia

- [1] Marcello Rubens Barsi Andreeta – “Implantação da técnica de crescimento de cristais por fusão a laser e a preparação de fibras monocristalinas”.
Dissertação de mestrado, IFSC – USP, 1996.
- [2] Liana Bueno Oliveira Amorim de Moraes – “Crescimento de cristais orgânicos e a avaliação de suas qualidades para aplicações em óptica não-linear”.
Dissertação de mestrado, IFSC-USP, 1998.
- [3] R.S. Feigelson – “Growth of fiber crystals, in: “Crystal Growth of Electronic Materials, Part II (North-Holland, Amsterdam, 1985) p.127.

CAPÍTULO 3

PUXAMENTO DE CRISTAIS

III. PUXAMENTO DE CRISTAIS

A técnica de puxamento de cristais tem sido usada para a preparação de cristais de $\text{Bi}_{12}\text{MO}_{20}$ ($\text{M} = \text{Si}, \text{Ti} \text{ e } \text{Ge}$), LiNbO_3 e compostos de halogenetos alcalinos. A exceção dos cristais da família $\text{Bi}_{12}\text{MO}_{20}$, os demais inserem-se dentro de projetos de cooperação científica com outros Grupos de Pesquisa do País. Em particular, as caracterizações físicas desses cristais tem sido efetuada pelos Profs. Drs. Máximo Siu Li, Maria Cristina Terrile, Luiz Antônio de Oliveira Nunes, Tomás Catunda, todos do IFSC-USP e pelo Prof. Dr. Jaime Frejlich, da UNICAMP, SP e Prof. Dr. A. Sérgio B. Sombra, Depto. de Física, UFC, Ceará. Nessa técnica o fundamental é controlar a dissipação do calor latente de fusão na interface sólido/líquido para a obtenção de um monocrystal. Alguns aspectos fundamentais serão brevemente abordados.

3.1 – A TÉCNICA CZOCHRALSKI

A técnica de puxamento de cristais a partir de um material fundido foi desenvolvida por Czochralski, CZ, (1917) para o crescimento de filamentos metálicos de cristais de baixo ponto de fusão, tais como: estanho, chumbo e zinco. Durante muito tempo a técnica foi usada para fundir congruentemente compostos de todas as classes, mas somente tornou-se popular em 1950 quando foram produzidos, pela primeira vez, monocrristais de germânio. Desde então tornou-se uma importante técnica de preparação de cristais e é largamente usada na indústria de materiais óxidos e semicondutores.

No método CZ o material a ser crescido é totalmente fundido num cadiinho (inerte à fase líquida), que é aquecido com elementos resistivos ou por indução (radio-freqüência). O puxador, também conhecido como dedo-frio, contendo a semente, parte de um cristal, fixada em sua extremidade inferior, é posicionado axialmente acima do cadiinho. A semente é levada a tocar a fase líquida, para servir de ponto de nucleação e dar orientação ao monocristal. A temperatura do sistema é ajustada até que o menisco permaneça inalterado. O dedo-frio é então girado a uma dada freqüência angular, previamente determinada, para produzir simetria axial e convecção forçada na fase líquida. Nessas condições temos um equilíbrio dinâmico entre as fases sólida (semente) e líquida. Abaixando a temperatura lentamente, a condição de equilíbrio dinâmico passa para uma outra condição de “quase equilíbrio dinâmico”, favorecendo a fase sólida, uma vez que a redução da temperatura causa esse sentido preferencial para o fluxo das unidades de crescimento (moléculas, íons, átomos) devido a alterações dos potenciais químicos das fases. Quando o puxamento e a taxa de crescimento do cristal são adequadas é obtido um cristal com boa qualidade óptica e estrutural.

A versatilidade deste método e sua fácil adaptação para uma grande variedade de materiais faz com que seja, atualmente, um método extremamente atrativo.

Algumas características relevantes são:

- cristal em crescimento não entra em contato com quaisquer superfícies contaminantes;
- uma variedade de orientações cristalográficas podem ser crescidas alterando-se a orientação da semente;
- cristal pode ser visualizado durante o processo de crescimento, e
- dopantes, em alguns casos, podem ser adicionados durante o processo.

Existem, entretanto, muitos problemas associados ao puxamento de cristais. O material a ser cristalizado deve ser cuidadosamente preparado para evitar sua contaminação e após a fusão, a superfície da fase líquida deve estar límpida para evitar nucleação parasita. Essas e outras dificuldades associadas ao método de CZ requerem somente um esforço experimental suplementar para serem sanadas. No entanto, um outro conjunto de problemas é encontrado quando estamos interessados no crescimento de cristais de alta qualidade óptica. Alguns desses problemas estão relacionados com a rotação da semente, a forma da interface, as instabilidades convectivas, a segregação de impurezas e são, muitas vezes, difíceis de serem resolvidos. A forma da interface pode estar ligada às instabilidades convectivas e acabam por gerar uma série de defeitos tanto macroscópico quanto microscópico no cristal. Em alguns casos é possível eliminar estas dificuldades impondo uma rotação ideal à semente.

Apesar do método de puxamento CZ ter sido inicialmente mais utilizado para compostos com fusão congruente, compostos com fusão incongruente também tem sido crescidos por um método conhecido como “Top Seed Solution Growth”. Neste caso um outro problema é introduzido; a composição da fase líquida é muito diferente do material a ser cristalizado. Como o cristal é removido da fase líquida, a composição do líquido restante altera-se e, consequentemente, as temperaturas de equilíbrio em que as fases sólida e líquida coexistem variam. A temperatura do sistema deve, então, ser alterada para compensar a essa variação da temperatura da interface para manter a taxa de crescimento constante.

3.2 - TAXA DE PUXAMENTO DO CRISTAL

Um dos parâmetros experimentais importantes no processo de crescimento de cristais, utilizando-se o método CZ, é a taxa de puxamento. Para ocorrer uma progressiva solidificação do material é necessário remover o calor latente gerado na interface e, nos casos de compostos com fusão incongruente, também remover o solvente segregado da interface de crescimento.

Para a obtenção de cristais com poucas imperfeições é desejável que a interface sólido/líquido seja plana e a isoterma aproximadamente normal à direção de crescimento; o que implica em um gradiente de temperatura radial nulo ($dT/dr = 0$). Fixando-se uma direção, (a direção y , por exemplo), na interface cristal/líquido, o balanço de calor pode ser escrito como função dos parâmetros térmicos e das propriedades do cristal como:

$$A\rho_s \Delta H_f \frac{dy}{dt} = AK_s \left(\frac{dT}{dy} \right)_{S,i} - AK_L \left(\frac{dT}{dy} \right)_{L,i} \quad (3.1)$$

onde A é área da seção transversal, que será admitida constante, dy/dt é a velocidade de crescimento, $K_{S,L}$ são as condutividades térmicas das fases sólida e líquida, respectivamente, $(dT/dy)_{S,L}$ é o gradiente térmico axial no sólido e no líquido na interface, respectivamente, ρ_s é a densidade do sólido e ΔH_f é o calor latente de fusão. A partir da equação (3.1) podemos concluir que uma velocidade de crescimento máxima ocorrerá quando tivermos um maior gradiente de temperatura na fase sólida e um gradiente de temperatura na fase líquida nulo ou

negativo. Um gradiente de temperatura negativo na fase líquida não favorece ao crescimento, uma vez que o líquido torna-se instável (superresfriado) e, normalmente, um crescimento dendrítico é observado. No entanto, se o gradiente de temperatura na fase líquida for nulo, a velocidade de crescimento máxima será:

$$\left(\frac{dy}{dt} \right)_{\max} = \frac{1}{\rho_s \Delta H_f} K_s \left(\frac{dT}{dy} \right)_{s,i} \quad (3.2)$$

Da equação (3.2) verificamos que a velocidade de crescimento máxima depende do gradiente de temperatura através do monocrystal e da sua condutividade térmica. Desta forma o parâmetro mais importante que devemos analisar, se quisermos comparar as taxas de crescimento para diferentes materiais, é a condutividade térmica do sólido. Ela pode variar de 0.1W/mK para materiais orgânicos a 300W/mK para os metais. Logo, as mais altas velocidades de crescimento podem ser encontradas em crescimento de metais puros e, no outro extremo, as menores em materiais orgânicos. A partir do conhecimento das propriedades do sólido e o gradiente de temperatura axial na interface sólido/líquido podemos determinar a velocidade de crescimento.

Numa situação em que o gradiente de temperatura no líquido não é nulo, podemos fazer a aproximação de que na região de menisco o gradiente de temperatura é linear, ou seja:

$$\left(\frac{dT}{dy} \right)_{L,i} = \frac{T_l - T_f}{L} \quad (3.3)$$

onde T_l é a temperatura do líquido na região do menisco, T_f é a temperatura de fusão na interface sólido/líquido e L é o comprimento da coluna de líquido suspensa sob a interface por tensão superficial.

Assumindo que a força de tensão superficial é igual à resultante da força gravitacional que age sobre a coluna de líquido, podemos reescrever o gradiente de temperatura axial na interface líquido/sólido como:

$$\left(\frac{dT}{dy} \right)_{L,i} = \frac{(T_l - T_f)}{2\gamma} r \rho_l g \quad (3.4)$$

onde γ é a tensão superficial do líquido, ρ_l é a densidade do líquido e g é a aceleração da gravidade.

Substituindo (3.4) na equação (3.1), admitindo-se que a área da seção transversal é a mesma para o sólido e o líquido, encontramos que o raio do cristal será:

$$r = \left(\frac{2\gamma}{\rho_l g K_l} \right) \left(\frac{1}{T_l - T_f} \right) \left[K_s \left(\frac{dT}{dy} \right)_{s,i} - \Delta H_v \frac{dy}{dt} \right] \quad (3.5)$$

Logo, o raio do sólido formado é inversamente proporcional à $(T_l - T_f)$, ou seja, com o aumento da temperatura da fase líquida ocorre a diminuição do raio do cristal em crescimento. Da equação (3.5) também pode-se concluir que aumentando a velocidade de crescimento, o raio do cristal diminui e vice-versa. Ainda pode-se inferir que flutuações em alguns parâmetros do processo de crescimento, acarretará numa variação do diâmetro do cristal, o que poderá levar a variação de composição e do seu índice de refração.

Na condição de solidificação progressiva do material o volume da fase líquida diminui com o crescimento do cristal para uma determinada taxa de puxamento imposta ao sistema.

Considerando que o sólido está sendo puxado com velocidade v_p e o nível do líquido no cadinho abaixa com velocidade v_L , progressivamente, não havendo perda por evaporação, podemos escrever que a velocidade de crescimento real do cristal f será:

$$f = v_p + v_L \quad (3.6)$$

Levando em conta a conservação de massa, podemos escrever f como função do parâmetros geométricos e densidades do sólido e do líquido:

$$f = v_p \left(\frac{R^2 \rho_L}{R^2 \rho_L - r^2 \rho_s} \right) \quad (3.7)$$

Essa equação relaciona então a velocidade de crescimento real com a taxa de puxamento.

Se considerarmos o raio de um cristal $r \approx 10\text{mm}$ (típico para muito de nossos experimentos de $\text{B}_{12}\text{SiO}_{20}$ - BSO) raio do cadinho $R \approx 30\text{mm}$, a razão $\rho_s / \rho_L = 1,18$ e considerando o valor de ρ_L ($\rho_L = 7,63\text{g/cm}^3$) do BSO, a velocidade de crescimento do cristal será 1,15 maior que a taxa de puxamento.

3.3 – FORMA DA INTERFACE

Experimentalmente verificamos que as formas das interfaces podem ser convexa, plana ou côncava. Para se conseguir manter uma interface plana é de fundamental importância entender a hidrodinâmica do processo de crescimento de um cristal. O movimento do fluido estabelece a forma da interface e o surgimento de diversos defeitos, como estrias, variação da composição, etc.

Em um material fundido puro, três tipos de fluxos podem ser considerados: *convecção livre*; *fluxos dirigido por tensão superficial (fluxos de Marangoni)*, *convecção forçada*; causada pela rotação do cristal e/ou pela rotação do cadrinho. Os dois mais importantes são devido a convecção livre e a forçada.

Convecção livre em um material fundido puro pode surgir devido à gradientes de temperaturas contrários ou instáveis ou ainda por inomogeneidade de temperatura na fase líquida. Em geral, na condição de convecção livre, o movimento do fluido é dado por uma componente que se desloca do fundo à superfície, ao longo da parede do cadrinho, cuja temperatura é maior que no centro. Como a interface livre de crescimento, líquido/ambiente, possui temperatura menor do que na parede do cadrinho, o fluxo advindo do fundo é empurrado em direção ao eixo de simetria, abaixo do cristal. Sendo a temperatura próxima ao eixo de simetria ainda menor do que a próxima da parede do cadrinho ocorrerá um fluxo (com componente) no sentido contrário àquele existente nas proximidades da parede. Este padrão de fluxo é circularmente mantido e é direcionado para cima ao longo da parede do cadrinho e para baixo ao longo do eixo de simetria.

Por outro lado a *convecção forçada* é considerada como uma mistura de fluxos provocados por forças de suspensão, associada à convecção livre, e pela rotação do cristal. Quando o cristal sofre uma rotação, o fluido abaixo do cristal é espalhado devido à força centrífuga que age contra a convecção livre. Com o aumento da taxa de rotação do cristal, o contra – fluxo, provocado por esta rotação, supera parcialmente o fluxo associado à convecção livre. O fluido abaixo do cristal começa a ser espalhado enquanto que os fluxos ao longo da parede do cadrinho e ao longo dos eixos fazem um movimento helicoidal. Da mesma forma

que existe um limite superior para a taxa de puxamento existe uma limitação para a taxa de rotação do cristal. A máxima taxa de rotação é função do gradiente de temperatura axial no líquido, da viscosidade, do raio do cristal e da taxa de puxamento.

Variações no padrão de fluxo com a rotação do cristal influencia o perfil de temperatura na região líquida. Para o cristal em crescimento com taxa de rotação nula, o fluxo decorrente de convecção livre deforma para baixo, na direção do fundo do cadrinho, as isotermas, podendo com isso aumentar a curvatura da interface. Por outro lado, com a rotação do cristal, a convecção livre é significativamente suprimida e um contra-fluxo, formado nas proximidades do cristal, deforma para cima, diretamente no material fundido, as isotermas.

3.4 Artigo: Large $\text{Bi}_{12}\text{TiO}_{20}$ single crystals: a study of intrinsic defects and growth parameters.

3.5 Artigo: Synthesis, crystal growth and characterization of γ -phase bismuth titanium oxide with gallium.

3.6 Artigo: $\text{Yb}^{+2}/\text{CN}^{-1}$ doped KBr absorption and emission structure.

3.7 Artigo: Optical and ESR study of Er^{+3} in LiNbO_3 .

Bibliografia

- [1] JESIEL FREITAS CARVALHO - Crescimento e propriedades ópticas de cristais de $\text{Bi}_{12}\text{TiO}_{20}$ puro e com V, Pb e Ce. Tese de doutoramento, Universidade de São Paulo, IFSC, 1999.
- [2] ARILSON REGES LOBATO - Síntese, crescimento e caracterização de cristais de $\text{Bi}_{12}\text{Ti}_{1-x}\text{Ga}_x\text{O}_{20}$ para aplicações em dispositivos optoeletrônicos. Dissertação de mestrado, Universidade de São Paulo, IFSC, 1998.
- [3] JOSÉ PEDRO ANDREETA – Crescimento de cristais uma abordagem fenomenológica. Tese de Livre-Docência, Universidade de São Paulo, IFSC, 1997.
- [4] V.V. PROKOFIEV; J.F. CARVALHO; J.P. ANDREETA; N.J.H.GALLO; A.C. HERNANDES; J.FREJLICH; A.A. FESCHI; P.M.GARCIA; J.MACAIBA; A.A. KAMSHILIN; T. JÄÄSKELAINEN - Growth and characterization of photorefractive $\text{Bi}_{12}\text{TiO}_{20}$ single crystals. Crystal Research Tech., 30(2): 171-176, 1995.
- [5] W.A. TILLER – The science of crystallization – Macroscopic phenomena and defect generation. Cambridge University Press, Cambridge, 1991.
- [6] J.P. van der EERDEN, O.S.L. BRUINSMA – Science and technology of crystal growth. Kluwer Academic Publishers, The Netherlands, 1995.
- [7] MULLER, M.; FABRIS, L.; HERNANDES, A.C.; SIU LI, M. - "Strong and broad 570 nm Emission in $\text{KCl} : \text{Yb}^{2+} : \text{CN}^{1-}$ ". Phys. Stat. Sol. (b), 180 (2): K93-K96, 1993.
- [8] de PAIVA, J.A.C.; DE ARAUJO, E.B.; HERNANDES, A.C.; SOMBRA, A.S.B. - "KiloHertz relaxation process in $\text{LiNbO}_3 : \text{Fe}$ single crystals" - Phys. Stat. Sol. (a), 147(2): 585-589, 1995.

De acordo com as políticas editoriais, este artigo não pode ser depositado em repositório de acesso aberto. Para acesso ao artigo completo entre em contato com o(a) autor(a) ou com o Serviço de Biblioteca e Informação IFSC - USP (bib@ifsc.usp.br)

CARVALHO, J. F.; HERNANDES, A. C. Large $\text{Bi}_{12}\text{TiO}_{20}$ single crystals: a study of intrinsic defects and growth parameters. **Journal of Crystal Growth**, Amsterdam, v.205, p.185-190, 1999.

Synthesis, Crystal Growth and Characterization of γ -Phase Bismuth Titanium Oxide with Gallium

A.R. Lobato^a, S. Lanfredi, J.F. Carvalho^a, A.C. Hernandes^{a*}

^a*Universidade de São Paulo, Instituto de Física de São Carlos. C.P. 369,
13560-970 São Carlos - SP, Brasil*

^b*Universidade Federal de Goiás, Instituto de Física. C.P. 131,
94001-970 Goiânia - Go, Brasil*

Received: May 29, 2000; Revised: August 13, 2000

Gallium solubility in the $\text{Bi}_{12}\text{TiO}_{20}$ (BTO) matrix was investigated by solid state reaction synthesis and $\text{Bi}_{12}\text{Ti}_{(1-x)}\text{Ga}_x\text{O}_{20}$ (BTGaO) single crystals were grown by Top Seeded Solution Growth (TSSG). We determined that it is possible to obtain a continuous solid solution from $(x)\text{Bi}_{12}\text{TiO}_{20}:(1-x)\text{Bi}_{12}[\text{Ga}_{0.7}\text{Bi}_{0.3}]\text{O}_{20}$ and that Ga replaces Ti in the BTO matrix giving $\text{Bi}_{12}\text{Ti}_{(1-x)}\text{Ga}_x\text{O}_{20}$ up to $x < 0.2$. BTGaO single crystals grown with an excess of Bi_2O_3 were transparent, a bleaching effect was observed due to the presence of gallium in the crystalline sillenite structure and their lattice parameter was higher than for pure BTO. The results for BTGaO single crystals showed an increase in the optical activity from $\rho_0 = 6.4^\circ \pm 0.3^\circ/\text{mm}$, for BTO, to $\rho_0 = 9.7^\circ \pm 0.3^\circ/\text{mm}$, for BTGaO grown with $x = 0.30$ in the melt. The BTGaO crystal presented an activation energy value of $0.48 \pm 0.02 \text{ eV}$ for $100^\circ\text{C} \leq T \leq 300^\circ\text{C}$.

Keywords: *crystal growth, bismuth titanium oxide, optical material*

1. Introduction

Bismuth oxide (Bi_2O_3) is an interesting dielectric material with potential applications such as optical coatings, in metal/insulator/semiconductor (MIS) capacitors and integrated microwave circuits¹. The Bi-O system is rather complicated and can have four different main crystalline phases, usually indicated by the letters α , β , γ and δ . Recently, a new polymorphic form of Bi_2O_3 with the A-type rare-earth sesquioxide structure was synthesized by a high-pressure technique². Each of these phases has different electrical and optical properties³. The γ -phase bismuth oxide is a very important material for optical applications when stabilized at room temperature. The γ -phase can be stabilized by adding some ions to its crystalline structure. When this is done, the resulting compounds are known as sillenite, named after Sillen, who discovered this special class of materials^{4,5}.

Sillenite crystals are of the $\text{Bi}_{12}\text{MO}_{20}$ type, where M = Si, Ge, Ti and others, and crystallize in the I23 space group. They have a number of interesting properties, including piezoelectric, electro-optical, elasto-optical, optical activity and photoconductivity. Of particular interest is the

combination of electro-optical and photoconductivity properties, which results in the so-called photorefractive effect, consisting of a reversible light-induced change in the refractive index⁶. Because of these properties, sillenite crystals are useful for many advanced and potentially promising applications, such as a reversible recording medium for real-time holography or for image processing applications^{7,8}. Bismuth titanium oxide, $\text{Bi}_{12}\text{TiO}_{20}$ (BTO), has some practical advantages in terms of its isomorphous $\text{Bi}_{12}\text{SiO}_{20}$ (BSO) and $\text{Bi}_{12}\text{GeO}_{20}$ (BGO), including lower optical activity, higher electro-optic coefficient and increased sensitivity to red light⁸.

In recent years, many articles have been published about the influence of impurities added to these crystals in the attempts that have been made to improve their optical properties⁹. Gallium doped BTO crystals (BTO:Ga) and pure $\text{Bi}_{12}\text{Ga}_x\text{Bi}_{1-x}\text{O}_{19.5}$ (BGaO), in particular, have lately been prepared but few reports discuss the synthesis, growth process and properties of these crystals¹⁰⁻¹¹. This paper discusses our investigation of the solubility of gallium in the BTO matrix using solid state reaction synthesis, the growth of $\text{Bi}_{12}\text{Ti}_{(1-x)}\text{Ga}_x\text{O}_{20}$ (BTGaO) single crystals by the Top Seeded Solution Growth (TSSG) method and struc-

tural (X-ray powder diffraction technique, differential thermal analysis (DTA), electron probe microanalysis, optical microscopy), optical (optical absorption, optical activity, electro-optic coefficient, photocurrent response) and electrical (impedance spectroscopy) characterization.

2. Experimental

Bismuth oxide (Johnson Matthey, 99.9995%), titanium oxide (Johnson Matthey, 99.995%) and gallium oxide (Trikol/Ventron Division, 99.99%) were employed as starting materials in the solid state reaction used as synthesis process. After being weighed in suitable molar proportions, the compounds were mechanically mixed to obtain a homogeneous product, which was put into a pure platinum crucible, placed in a resistive furnace and heated to 800 °C. After one hour at this temperature, the material was removed and finely ground with a mortar, after which it was returned to the furnace. This procedure was repeated eleven times over a 96-hour period. In the first grinding procedure, isopropyl alcohol was used as a liquid medium to improve the mixing. In this case, the material was air dried before being returned to the furnace.

The crystals were made through the Top Seeded Solution Growth method using a resistive heating furnace equipped with an 808 Eurotherm microprocessor-based digital temperature controller unit attached to a Pt-Pt10%Rh thermocouple. The temperature fluctuations were typically lower than 0.3 °C, as measured near the crucible. An axial temperature gradient above the melt of about 10 °C/cm was measured with a platinum thermocouple attached to the seed holder. High purity cylindrical platinum crucibles, with approximate dimensions of 35 x 35 mm, were used. The starting batch melt was prepared by thoroughly mixing appropriate amounts of bismuth oxide (Johnson Matthey, 99.9995%), titanium oxide (Johnson Matthey, 99.995%) and gallium oxide (Trikol/Ventron Division- 99.99%), followed by melting. All runs were carried out in an open-air environment. BGO seeds oriented along the [001] direction, contained in a pure platinum seed holder, were used to initiate crystal growth. Pulling rates ranging from 0.25 to 0.30 mm/h and 25 to 30 rpm rotation rates were used. After their growth was completed, the crystals were annealed at 700 °C in an appropriate furnace to reduce thermal stresses.

X-ray powder diffraction spectra were collected using CuK α radiation from an automatic diffractometer RIGAKU-ROTAFLEX RU-200B equipped with a rotatory anode. Data collection was made in the step scan mode in the 2 θ range from 5 to 120° with 0.02° step interval and a step time of 3 s. The samples were very fine powder. Lattice parameters were calculated by the least square method using a computational program. Differential Thermal Analysis (DTA) measurements were carried out in a TA

Instrument DSC 2090 at 10 °C/min. The samples (~35 mg) used were very fine powder obtained from single crystals. Pure platinum crucibles were used in all the trials.

Single crystal optical quality was evaluated using an optical microscope with and without polarized light. The presence of gallium in the crystals was verified with a ZEISS Digital Scanning Electron Microscope (DSM960) equipped with a QX 2000 Link Energy Dispersive Spectrometer (EDS).

All optical measurements were performed at room temperature using carefully polished BTGaO samples. Optical absorption in the visible region was measured with a Cary 17 spectrophotometer. The photocurrent response was measured in a transverse geometry with silver electrodes arranged as two strips separated by 1 mm. The applied d.c. voltage was of 100 V. A Keythley 602 electrometer was used for current detection. The spectral range of excitation light used was from 700 to 400 nm. For optical activity measurements the crystal was placed between a polarizer and an analyzer and was illuminated by a 633 nm line of a He-Ne laser. The angle of rotation of the polarization plane was measured by rotating the analyzer until extinction. The rotatory power (p_0) was obtained by the ratio of the rotation's angle and the crystal's thickness. The effective electro-optic coefficient (r_{41}) was measured for $\lambda = 633$ nm, by using the method described in the literature^{12, 13}.

The electrical characterization was performed by impedance spectroscopy on 8 x 8 x 2 mm samples oriented along [100] direction. The samples were cleaned with acetone in an ultrasonic cleaner for 3 min and dried at 100 °C. The electrodes required for the electrical measurements were deposited on both faces of the sample by applying silver paste, which was dried at 400 °C for 15 min.

The electrical measurements were made from 5 Hz to 13 MHz, with an applied potential of 500 mV, using a Solartron 1260 Impedance Analyzer controlled by a personal computer. The samples were placed in an appropriate sample holder with a two-electrode configuration. The ac measurements were made from 100 °C to 300 °C with a 20 °C temperature step. A 30-minute interval was adopted prior to thermal stabilization after each measurement. All the measurements were carried out in atmospheric air.

The data were analyzed using the "Equivalent Circuit" (Equivcrt) software, a package for the analysis of complex immittance spectra.

3. Results and Discussion

3.1. Solid state reaction synthesis

An initial series of solid state reaction experiments was made using the molar proportion 6Bi₂O₃: (1-x)TiO₂: x/2Ga₂O₃ for x = 0.10, 0.20, 0.45 and 0.50. We verified that gallium can replace titanium in the BTO matrix giving the chemical formula Bi₁₂Ti_(1-x)Ga_xO₂₀ for x = 0.10 and 0.20.

Under these conditions, a homogeneous phase with sillenite structure is obtained, as verified by X-ray powder diffraction. For higher values of x ($x = 0.5$) another phase appears in addition to the sillenite. Some X-ray reflections resulting from this new phase, not identified, are shown in the insert in Fig. 1. This suggests that, for lower concentrations of gallium, the BTO structure can easily accommodate the gallium ions in the tetrahedral position, partially replacing the titanium ions. However, higher concentrations of gallium in the solid solution require an excess of bismuth oxide in comparison with the stoichiometric composition to obtain a single sillenite structure. This is due to the non-stoichiometric character of BGaO, whose chemical formula should be written $\text{Bi}_{12}[\text{Ga}_x\text{Bi}_{(1-x)}]\text{O}_{19.5}$, where x can range from 0.5 to 0.7¹⁰.

Considering the non-stoichiometric character of BGaO it was possible to obtain a homogeneous solid sillenite structure solution with the $\text{Bi}_{12}\text{Ti}_{0.5}[\text{Ga}_{0.35}\text{Bi}_{0.15}]\text{O}_{19.75}$ and $\text{Bi}_{12}\text{Ti}_{0.05}[\text{Ga}_{0.665}\text{Bi}_{0.285}]\text{O}_{19.525}$ compositions. The X-ray powder patterns of the materials thus obtained are shown in Fig. 1. Table 1 shows the lattice parameters values for different gallium concentrations. The diffraction lines due to $K\alpha_2$ radiation were extracted by software to calculate ones. The lattice parameters of BTO and BGaO are also given for comparison. Our results show that it is possible to obtain a continuous solid solution of the $(x)\text{Bi}_{12}\text{Ti}_{0.20}:(1-x)\text{Bi}_{12}[\text{Ga}_{0.70}\text{Bi}_{0.30}]\text{O}_{19.5}$ type with x ranging from 0 to 1. However, there is a solubility limit if one attempts to directly substitute Ti with Ga in the $\text{Bi}_{12}\text{Ti}_{(1-x)}\text{Ga}_x\text{O}_{20}$ chemical formula.

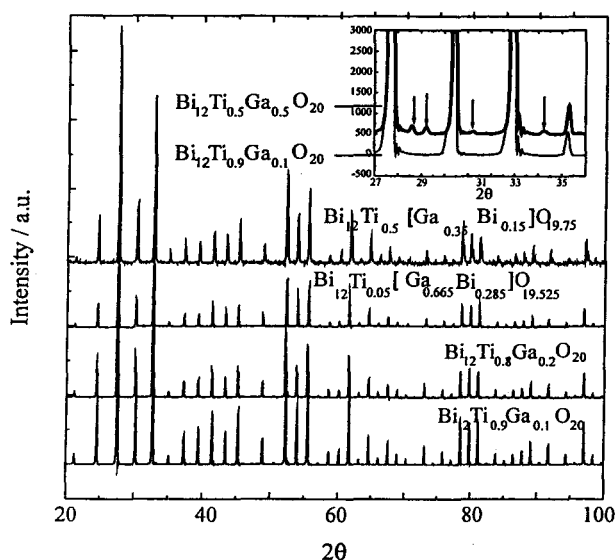


Figure 1. X-ray powder diffraction of $\text{Bi}_{12}\text{Ti}_{0.9}\text{Ga}_{0.1}\text{O}_{20}$; $\text{Bi}_{12}\text{Ti}_{0.8}\text{Ga}_{0.2}\text{O}_{20}$; $\text{Bi}_{12}\text{Ti}_{0.05}[\text{Ga}_{0.665}\text{Bi}_{0.285}]\text{O}_{19.525}$; $\text{Bi}_{12}\text{Ti}_{0.5}[\text{Ga}_{0.35}\text{Bi}_{0.15}]\text{O}_{19.75}$. Insert see details in text. In $\text{Bi}_{12}\text{Ti}_{0.5}[\text{Ga}_{0.35}\text{Bi}_{0.15}]\text{O}_{19.75}$ the $K\alpha_2$ diffraction lines are present.

Table 1. Lattice parameter for materials with different gallium concentrations obtained by solid state reaction synthesis.

Samples	Lattice parameter (Å)
$\text{Bi}_{12}\text{TiO}_{20}$ (BTO)	10.173(5)
$\text{Bi}_{12}\text{Ti}_{0.9}\text{Ga}_{0.1}\text{O}_{20}$	10.177(6)
$\text{Bi}_{12}\text{Ti}_{0.8}\text{Ga}_{0.2}\text{O}_{20}$	10.182(3)
$\text{Bi}_{12}\text{Ti}_{0.05}[\text{Ga}_{0.665}\text{Bi}_{0.285}]\text{O}_{19.525}$	10.182(6)
$\text{Bi}_{12}\text{Ti}_{0.5}[\text{Ga}_{0.35}\text{Bi}_{0.15}]\text{O}_{19.75}$	10.183(4)
$\text{Bi}_{12}\text{GaO}_{20}$ (BGaO)	10.182(3)

3.2. Crystal growth

BTGaO single crystals were grown from a liquid phase with the $10\text{Bi}_2\text{O}_3$: $(1x)\text{TiO}_2$: $x/2\text{Ga}_2\text{O}_3$ composition, where $x = 0, 0.10$ and 0.30 . The melting point of the crystals decreases from 875°C for nominally pure BTO to 822°C for BGaO, as determined by DTA. Figure 2 shows a BTGaO crystal as grown. An evident characteristic of BTGaO crystals was the bleaching effect associated to the presence of gallium.

Only around one third of the starting charges in all growth experiments were crystallized. Figure 3 shows the X-ray emission spectrum of a BTGaO sample, obtained by EDS, where $K\alpha$ gallium line is noticed. An accurate quantitative gallium concentration measurement using EDS was not possible because of the superimposition of the gallium $K\alpha$ and bismuth L_1 lines. Despite the difficulties involved in the growth of these crystals, good optical quality samples were obtained from the principal crystal body parts.

Growth defects such as striations, core and inclusions are frequent in sillenite family crystals. Optical microscopy was used to analyze these defects in our crystals. We found that the greater the gallium content, the more difficult the growth process and that there was a drastic increase in the occurrence of such defects. Growth striations are frequent in doped-crystals or in crystals that show some degree of non-stoichiometry. They correspond to compositional variations associated to the growth rate fluctuations that derive from changes in the solid-liquid interface temperature due to the convective process in the liquid phase¹⁴. The striations in our crystals are more evident owing to the higher gallium content in the liquid phase. The inclusions and voids that appear are associated mainly to the highly con-



Figure 2. BTGaO single crystal grown by top seeded solution growth.

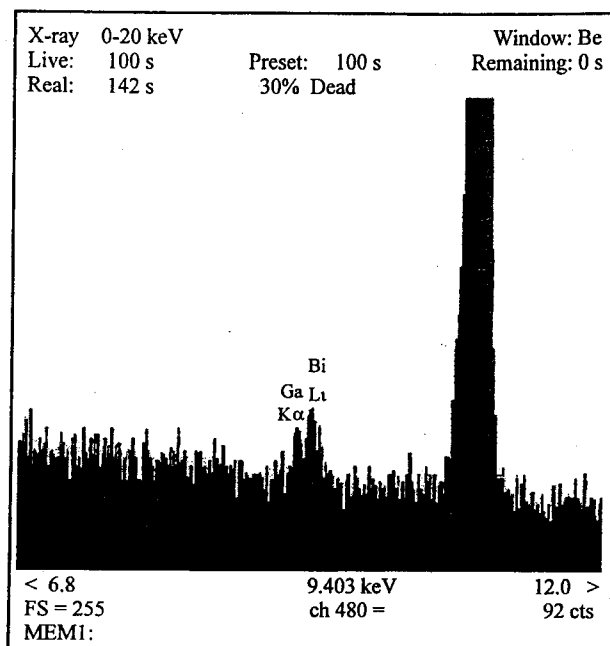


Figure 3. Characteristic X-ray emission spectrum of BTGaO sample.

vex growth interface, which is characteristic of the crystal shoulder region. They can also appear during the interface shape transition from convex to planar owing to growth interface instabilities produced by changes in the liquid convective fluxes that occur during this process. The core, a darker central column, is a characteristic defect in sillenite family crystals when the solid/liquid interface is convex. A core with a markedly darker coloration in comparison with nominally pure BTO appears in crystals with a high concentration of gallium. The core is absent in regions of crystals with a planar or slightly concave solid/liquid interface.

3.3. Optical properties

The optical activity grows linearly with the increase of the gallium content in the crystals from $\rho_0 = 6.4 \pm 0.3 \text{ g/mm}^3$, for nominally pure BTO, to $\rho_0 = 9.7 \pm 0.3 \text{ g/mm}^3$, for BTGaO grown with $x = 0.30$ in the melt. The gallium doping decreases the optical absorption coefficient by about 80% in the wavelength range of 700 to 550 nm and it causes the displacement of the absorption edge to smaller wavelengths. The dark current is increased approximately by four orders of magnitude in gallium-doped crystals, and no photocurrent response was detected in the range of 700 to 400 nm. The gallium presence doesn't cause significant change in the electro-optic coefficient value of BTO crystals ($r_{4f} = 5.6 \text{ pm/V}$).

3.4. Electrical properties

The electrical characterization of BTGaO, grown with $x = 0.30$ in the melt, was carried out by impedance spectroscopy. Figure 4 shows the impedance spectra present in the Z'' vs. Z' plots of the BTGaO obtained at different

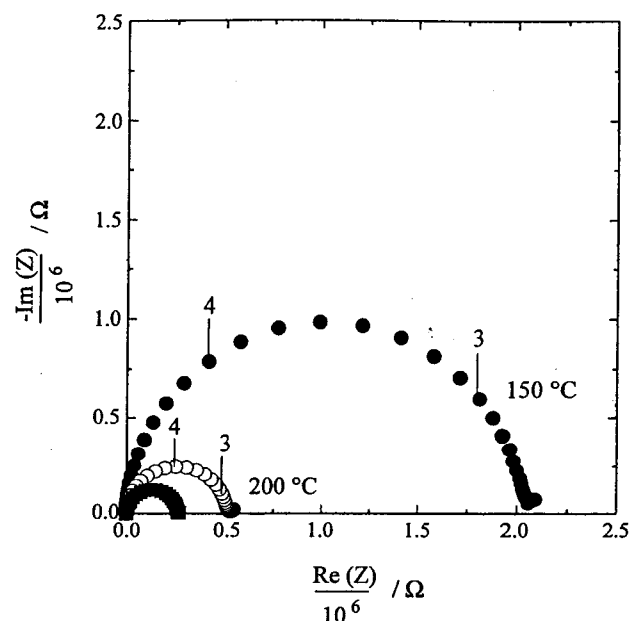


Figure 4. Complex impedance data at several temperatures of BTGaO single crystal. The smallest semicircle corresponds to a measurement taken at 250 °C. In this figure the numbers, 3, 4 give the \log_{10} (signal frequency) for the corresponding point.

temperatures. The diagrams show only the contribution in the high frequency region assigned to bulk response. No electrode effect was seen in the analyzed frequency range. The fitting curve showed good agreement with experimental data. The electric response was further fitted by a parallel RC equivalent circuit in the frequency range analyzed, where R represents the bulk resistance and C the bulk or geometric capacitance of the samples.

The electric conductivity of the bulk was plotted as a function of the temperature in an Arrhenius plot (Fig. 5). The activation energy for conduction was derived from slope plot was equal to $0.48 \pm 0.02 \text{ eV}$. Only one slope is apparent over an entire set of the measurements. By extrapolation of the curve $\log \sigma \propto 1/T$ (Fig. 5) the resistivity value of $2.9 \times 10^9 \Omega \text{ cm}$ at room temperature was obtained.

The $\text{Bi}_{12}\text{TiO}_{20}$ phase presents an activation energy value of 0.99 eV for $400 \text{ }^\circ\text{C} \leq T \leq 700 \text{ }^\circ\text{C}$ with a resistivity of $8.5 \times 10^{14} \Omega \text{ cm}$ at room temperature^{16,17}. Thus, the gallium doped BTO exhibit a significant change in the activation energy and resistivity values (four orders of magnitude for $100 \text{ }^\circ\text{C} \leq T \leq 300 \text{ }^\circ\text{C}$). By comparison with the $\text{Bi}_{12}\text{TiO}_{20}$ phase, a certain disorder level in the BTGaO structure should be expected. The Ti-vacancy complex defect in the $\text{Bi}_{12}\text{TiO}_{20}$ lattice has been suggested¹⁸. More recently, a complex defect formed by pair $(\text{Bi}_{\text{Ti}}^{3+} + \text{h}^+)$ has been hypothesized¹⁹. This intrinsic defect is associated with the improper occupation of the tetrahedrally coordinated Ti^{4+} site, of an Bi^{3+} coupled with a hole h^+ in the surrounding oxygen tetrahedron.

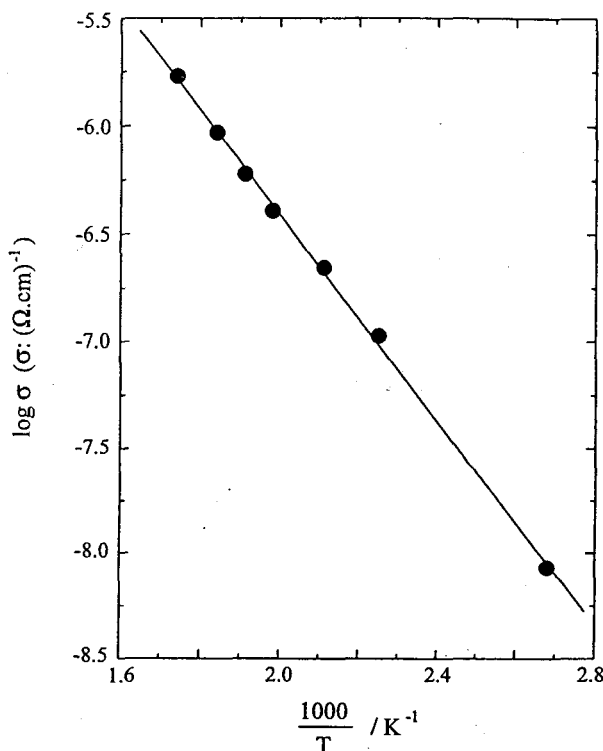


Figure 5. Arrhenius plot of electrical conductivity of BTGaO single crystal.

According to literature⁸, the $(\text{BiSi}^{3+} + \text{h}_0^+)$ defect is observed in $\text{Bi}_{12}\text{SiO}_{20}$ in view of the ultrasonic attenuation center with tetrahedral symmetry, which has been associated with an absorption shoulder. In gallium doped $\text{Bi}_{12}\text{SiO}_{20}$ this absorption shoulder is absent. This bleaching effect have been explained by assuming the transformation of the intrinsic defect $(\text{BiSi}^{3+} + \text{h}_0^+)$ to BiSi^{5+} . Considering the $\text{Bi}_{12}\text{TiO}_{20}$ structure similar to the $\text{Bi}_{12}\text{SiO}_{20}$ one, the addition of the gallium can result in the BiTi^{5+} defect in $\text{Bi}_{12}\text{TiO}_{20}$, as suggested by Oberschmid¹⁹. Substitution of Ga on Ti sites, however, result in acceptors levels responsible for the p type conduction. Thus, the activation energy value of 0.48 ± 0.02 eV can be associated to the sub-level in band gap edge below the conduction band.

4. Conclusions

In solid state reaction synthesis process gallium can replace titanium in the BTO matrix giving $\text{Bi}_{12}\text{Ti}_{(1x)}\text{Ga}_x\text{O}_{20}$ chemical formula for x up to 0.20. A continuous solid solution was possible when considered the non-stoichiometric character of BGaO. BTGaO single crystals of optical quality were grown from a liquid phase with up to 30% of gallium ions in the nominal liquid composition. Growth defects as striations were more evident in crystals with higher gallium content in the liquid phase. A bleaching effect was observed due to the presence of gallium in the crystalline sillenite structure. Its optical absorption was decreased for holographic applications. The electrical

properties of BTGaO single crystal can be described as parallel RC circuits. The electrical conductivity follows an Arrhenius law with an activation energy of 0.48 ± 0.02 eV, which can be associated to the sub-level in band gap edge below the conduction band.

Acknowledgments

The financial support of CNPq and FAPESP is gratefully acknowledged.

References

- Schuisky, M.; Härsta, A. *Chem. Vapor Deposition*, v. 2, n. 9, p. 235, 1996.
- Atou, T.; Faqir, H.; Kikuchi, M.; Chiba, H.; Syono, Y. *Mat. Res. Bull.*, v. 33, n. 2, p. 289, 1998.
- Bandoli, G.; Barreca, D.; Brescacin, E.; Rizzi, G.A.; Tondello, E., *Chem. Vapor Deposition*, v. 2, n. 9, p. 238, 1996.
- Levin, E.M.; Roth, R.S. *J. Res. Nat. Bureau of Standards-A. Physics and Chemistry*, v. 68A, n. 2, p. 189, 1964.
- Levin, E.M.; Roth, R.S. *J. Res. Nat. Bureau of Standards-A. Physics and Chemistry*, v. 68A, n. 2, p. 197, 1964.
- Buse, K. *Appl. Phys. B*, v. 64, p. 273, 1997.
- Buse, K. *Appl. Phys. B*, v. 64, p. 391, 1997.
- Arizmendi, L.; Cabrera, J.M.; Agulló-López, F. *Internat. J. Optoelectronics*, v. 7, p. 149, 1992.
- Carvalho, J.F.; Franco, R.W.A.; Magon, C.J.; Nunes, L.A.O.; Pellegrini, F.; Hernandes, A.C. *Mat. Research*, v. 2, p. 87, 1999.
- Coya, C.; Zaldo, C.; Volkov, V.V.; Egorysheva, A.V.; Polgár, K.; Péter, A. *J. Opt. Soc. Am.(B)*, v. 13, n. 5, p. 908, 1996.
- Riehemann, S.; Rickermann, F.; Volkov, V.V.; Egorysheva, A.V.; Von Bally, G. *J. Nonlinear Opt. Phys. and Mat.*, v. 6, n. 2, p. 235, 1997.
- Henry, M.; Mallick, S.; Rouède, D. *J. Appl. Phys.*, v. 59, p. 2650, 1986.
- Dias, M.A.F.; Hernandes, A.C.; Carvalho, J.F.; Frejlich, J. *Proceedings of the Symposium on Laser and their Applications*, Campinas - SP, Brazil, p. 272, 1997.
- Carvalho, J.F.; Hernandes, A.C. *J. Crystal Growth*, v. (1-2), p. 185, 1999.
- Cockayne, B. *J. Crystal Growth*, v. 42, p. 413, 1977.
- Efendiev, SH.M.; Bagiev, V.E.; Aliev, R.A.; Mustafaev, E.R. *Phys. Stat. Sol. (a)*, v. 109, p. 345, 1988.
- Lanfredi, S.; Carvalho, J.F.; Hernandes, A.C. *J. Appl. Phys.*, v. 88, p. 283, 2000.
- Efendiev, SH.M.; Bagiev, V.E.; Zeinally, A.C.H.; Balashov, V.A; Lomonov, V.A.; Majer, A.A. *Phys. Stat. Sol. (a)*, v. 63, p. K19, 1981.
- Oberschmid, R. *Phys. Stat. Sol. (a)*, v. 89, p. 263, 1985.

De acordo com as políticas editoriais, este artigo não pode ser depositado em repositório de acesso aberto. Para acesso ao artigo completo entre em contato com o(a) autor(a) ou com o Serviço de Biblioteca e Informação IFSC - USP (bib@ifsc.usp.br)

CASTRO, A. C.; HERNANDES, A. C.; SIU LI, M. $\text{Yb}^{2+}/\text{CN}^-$ doped KBr absorption and emission structures. **Radiation Effects & Defects in Solids**, London, v. 146, p. 349-355, 1998.

D. M. B. P. Milori, I. J. Moraes, A. C. Hernandes, R. R. de Souza, M. Siu Li, M. C. Terrile, and G. E. Barberis

The following corrections to the figures must be made. Figure 1 must be replaced by Fig. 3, Fig. 2 must be replaced by Fig. 1, and Fig. 3 must be replaced by Fig. 2. The captions are correct.

~~LiNbO_3 is occupied by Er^{3+} within the experimental sensitivity, in agreement with recent x-ray standing-wave measurements.~~

I. INTRODUCTION

Much interest in studying LiNbO_3 by physical methods has recently arisen, due to the unique physical properties presented by this ferroelectric material, such as photovoltaic, piezoelectric, elasto-optic, and photorefractive effects. Some of these properties are drastically affected by the presence of impurities, growing conditions, or thermal treatment, thus determining or affecting the particular technical application for the material. A large amount of papers has been published on this subject in the last decade, particularly oriented to the use of LiNbO_3 as a laser active medium, and monolithic integration of active electro-optic devices within the laser material.¹⁻⁷ The development of Er^{3+} amplifiers in optical fibers, and the great improvement that this gave to communications, have increased the research in materials such as $\text{LiNbO}_3:\text{Er}^{3+}$ that could be used as an active medium for the Er^{3+} frequencies.

Electron-spin resonance (ESR) studies of other rare-earth and 3d ions in LiNbO_3 (Gd^{3+} , Yb^{3+} , Nd^{3+} , Fe^{3+} , and Cr^{3+}) (Refs. 2, 3) show trigonal symmetry, as expected from magnetic ions substituting for Li or Nb in the lattice, or located as interstitial ions in the most probable position of the unit cell. One of the existing examples² shows that two different sites were found for Gd^{3+} in LiNbO_3 , but our ESR experiments and the optical data here presented show only one unique site for the Er^{3+} ion in LiNbO_3 within the experimental error. Very recently, Gog *et al.*,⁴ using the x-ray standing-wave (XSW) technique, determined that the site occupied by Er^{3+} is a position near the Li site, with the same trigonal symmetry, displaced slightly in the $-c$ axis direction. They used nearly perfect single crystals, with Er^{3+} introduced by diffusion, in very small concentrations. Our work corroborates the statement made in Ref. 4, in the sense that only one trigonal site is occupied by the rare earth.

II. EXPERIMENTAL DETAILS

The samples used in our experiments were grown by the Czochralski method, using an automatic crystal growth system from Cambridge Instruments. They were prepared by melting optically pure Li_2CO_3 and Nb_2O_5 in the correct congruent proportions obtained from the phase diagram (48.6% of the first and 51.4% of the second). Seeds were oriented with the c axis in the vertical direction, to obtain oriented single crystals. Er_2O_3 was diluted in the melt to obtain Er^{3+} as impurity. The nominal Er concentration was 0.05 mol % in all our samples. As the fusion temperature of the melt (1253°C) is higher than the ferroelectric critical temperature ($T_c \approx 1210^\circ\text{C}$) the crystals grow in the paraelectric phase, giving origin to multidomains as they are cooled, with their optical and magnetic characteristics altered. To avoid that, we applied a small electric field to the melt during the growing ($|\vec{E}| = 0.2 \text{ V/cm}$, corresponding to a current of 1.2 mA/cm^2) obtaining single domain single crystals. As Fe and the ions OH^- are natural impurities in the samples, we did a study of annealing methods, oriented to purify the samples. After shaping and polishing the samples thoroughly, we annealed them in an oxygen atmosphere, in a ceramic crucible at 700°C , for eight hours. The resulting samples are perfectly transparent, and neither the ESR nor the optical measurements show the presence of Fe. OH^- ions were not detected by optical means, either.

The fluorescence spectrum was obtained by exciting the samples with an argon-ion laser using the 4880 and 4765 Å lines at room temperature and liquid nitrogen in a classical experimental arrangement. We used a 0.5 m Jarrel-Ash 82-000 monochromator, and a Thorn Emi 9558 QA photomultiplier as detector.

Polarized absorption experiments in the range from 33 330 to 5000 cm^{-1} were done with a Cary-17 spectrophotometer with a Glan-Thompson calcite polarizer.

D.M.B.P. Milori, I.J. Moraes,* A.C. Hernandes, R.R. de Souza, M. Siu Li, and M.C. Terrile

*Instituto de Física de São Carlos, Universidade de São Paulo-São Carlos, Caixa Postal 369,
13560 São Carlos, São Paulo, Brazil*

G.E. Barberis

Instituto de Física "Gleb Wataghin," Universidade Estadual de Campinas, 13083-970 Campinas, São Paulo, Brazil
(Received 1 July 1994)

We report laser-excited optical transitions between the $^4S_{3/2}$ and $^4I_{15/2}$ multiplets of Er³⁺ as an impurity in the LiNbO₃ host, together with the optical-absorption spectra at liquid-helium and liquid-nitrogen temperatures. The optical data allow us to determine the crystal-field splittings of those levels and the spin-Hamiltonian parameters for the $^4I_{15/2}$ lower multiplet. The observed electron-spin resonance and the angular variation of this spectrum agree with the parameters obtained by optical techniques. Both techniques show that only one of the three possible trigonal sites in LiNbO₃ is occupied by Er³⁺ within the experimental sensitivity, in agreement with recent x-ray standing-wave measurements.

I. INTRODUCTION

Much interest in studying LiNbO₃ by physical methods has recently arisen, due to the unique physical properties presented by this ferroelectric material, such as photovoltaic, piezoelectric, elasto-optic, and photorefractive effects. Some of these properties are drastically affected by the presence of impurities, growing conditions, or thermal treatment, thus determining or affecting the particular technical application for the material. A large amount of papers has been published on this subject in the last decade, particularly oriented to the use of LiNbO₃ as a laser active medium, and monolithic integration of active electro-optic devices within the laser material.¹⁻⁷ The development of Er³⁺ amplifiers in optical fibers, and the great improvement that this gave to communications, have increased the research in materials such as LiNbO₃:Er³⁺ that could be used as an active medium for the Er³⁺ frequencies.

Electron-spin resonance (ESR) studies of other rare-earth and 3d ions in LiNbO₃ (Gd³⁺, Yb³⁺, Nd³⁺, Fe³⁺, and Cr³⁺) (Refs. 2, 3) show trigonal symmetry, as expected from magnetic ions substituting for Li or Nb in the lattice, or located as interstitial ions in the most probable position of the unit cell. One of the existing examples² shows that two different sites were found for Gd³⁺ in LiNbO₃, but our ESR experiments and the optical data here presented show only one unique site for the Er³⁺ ion in LiNbO₃ within the experimental error. Very recently, Gog *et al.*,⁴ using the x-ray standing-wave (XSW) technique, determined that the site occupied by Er³⁺ is a position near the Li site, with the same trigonal symmetry, displaced slightly in the -c axis direction. They used nearly perfect single crystals, with Er³⁺ introduced by diffusion, in very small concentrations. Our work corroborates the statement made in Ref. 4, in the sense that only one trigonal site is occupied by the rare earth.

II. EXPERIMENTAL DETAILS

The samples used in our experiments were grown by the Czochralski method, using an automatic crystal growth system from Cambridge Instruments. They were prepared by melting optically pure Li₂CO₃ and Nb₂O₅ in the correct congruent proportions obtained from the phase diagram (48.6% of the first and 51.4% of the second). Seeds were oriented with the c axis in the vertical direction, to obtain oriented single crystals. Er₂O₃ was diluted in the melt to obtain Er³⁺ as impurity. The nominal Er concentration was 0.05 mol % in all our samples. As the fusion temperature of the melt (1253 °C) is higher than the ferroelectric critical temperature ($T_c \approx 1210$ °C) the crystals grow in the paraelectric phase, giving origin to multidomains as they are cooled, with their optical and magnetic characteristics altered. To avoid that, we applied a small electric field to the melt during the growing ($|\vec{E}| = 0.2$ V/cm, corresponding to a current of 1.2 mA/cm²) obtaining single domain single crystals. As Fe and the ions OH⁻ are natural impurities in the samples, we did a study of annealing methods, oriented to purify the samples. After shaping and polishing the samples thoroughly, we annealed them in an oxygen atmosphere, in a ceramic crucible at 700 °C, for eight hours. The resulting samples are perfectly transparent, and neither the ESR nor the optical measurements show the presence of Fe. OH⁻ ions were not detected by optical means, either.

The fluorescence spectrum was obtained by exciting the samples with an argon-ion laser using the 4880 and 4765 Å lines at room temperature and liquid nitrogen in a classical experimental arrangement. We used a 0.5 m Jarrel-Ash 82-000 monochromator, and a Thorn Emi 9558 QA photomultiplier as detector.

Polarized absorption experiments in the range from 33 330 to 5000 cm⁻¹ were done with a Cary-17 spectrophotometer with a Glan-Thompson calcite polarizer.

to 200 cm^{-1} , a Perkin-Elmer 180 was employed. The minimum spectral resolution was 1 cm^{-1} . Cooling of the samples was obtained by immersion. The ESR measurements were carried out with an X- and Varian E-109 spectrometer, using 100 kHz magnetic field modulation. The power applied to the samples was 1 mW in most of the experiments. We cooled the samples with an APD Cryogenics Inc. model LTR-3 Helitran, adapted to the microwave cavity. We used liquid helium cryogenic liquid.

III. RESULTS AND DISCUSSION

The LiNbO_3 crystal belongs to the C_{3v}^6 ($R\bar{3}c$) space group, where Li^+ is in the $[0,0,1/4]$ position, and Nb^{5+} in the $[0,0,0]$, both in the trigonal axis. Cationic impurities enter into the lattice by substituting for those ions, or in an interstitial position also belonging to the axis $[0,0,1/6]$. Always, the point symmetry of the impurity is C_3 , and it produces an angular variation of the SR spectra that is axial in every case. Group theory can be used to predict the optical and electron paramagnetic resonance (EPR) spectra. As is known, for the D_3 point group, the lower $^4I_{15/2}$ multiplet of Er^{3+} splits completely into eight Kramers doublets.

Figure 1 shows partially the experimental fluorescence spectra of Er^{3+} in LiNbO_3 , where the so-called π (parallel to the ferroelectric axis) and σ (perpendicular to it) polarizations of the light are indicated with dashed and full lines, respectively. The numbering of the peaks identifies the transitions between the $^4S_{3/2} \rightarrow ^4I_{15/2}$ Er^{3+} multiplets. Figure 2 shows the absorption spectra obtained at liquid-helium temperature, where only the lowest level of the Er^{3+} ion is highly populated. Only two peaks can be seen, with different intensities for each of the polarization directions. Figure 3 shows the absorption spectra at

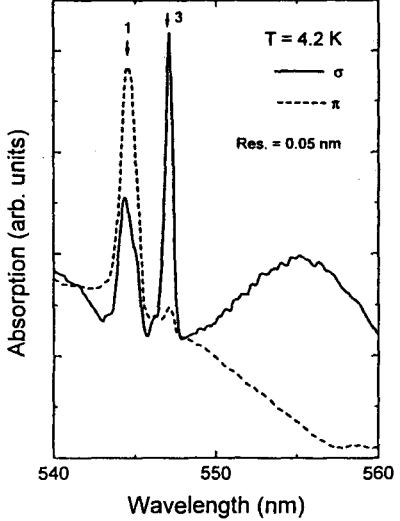


FIG. 1. Fluorescence spectra of $\text{LiNbO}_3:\text{Er}^{3+}$ where the transitions are numbered in accordance with Fig. 4 below.

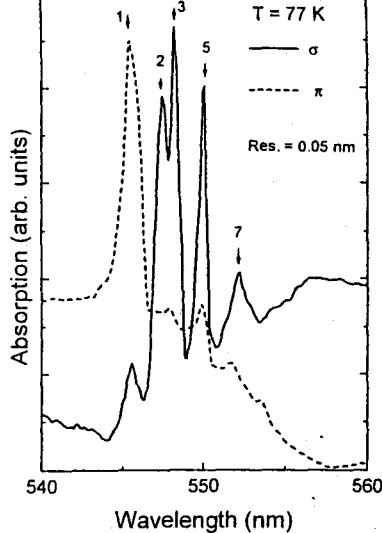


FIG. 2. Absorption spectra of $\text{LiNbO}_3:\text{Er}^{3+}$ at liquid-helium temperature for both polarization directions. The peaks are numbered in accordance with Fig. 4 below.

liquid-nitrogen temperature, where other than the lowest level of the $^4I_{15/2}$ multiplet are populated: several peaks, numbered to be identified, can be seen for both polarization directions in the same wavelength region. Figure 4 summarizes the level diagram obtained from the optical spectra together with the levels calculated by fitting the Hamiltonian

$$\hat{H}_{cc} = \frac{B_2^0}{\sqrt{3}} [O_2^1(c) + O_2^1(s) + O_2^2(s)] + B_2 O_2^0 + B_4 O_4 + B_6 O_6 \quad (1)$$

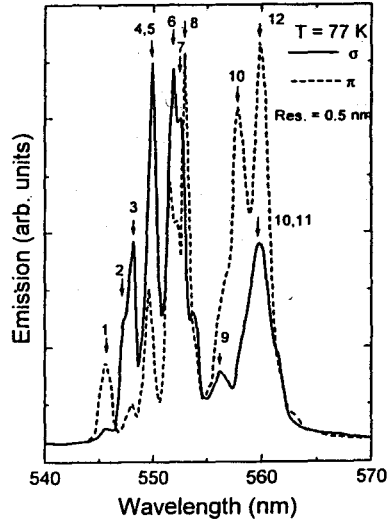


FIG. 3. Absorption spectra of $\text{LiNbO}_3:\text{Er}^{3+}$ at liquid nitrogen temperatures. Some of the lines are numbered, and are identified as transitions in Fig. 4 below.

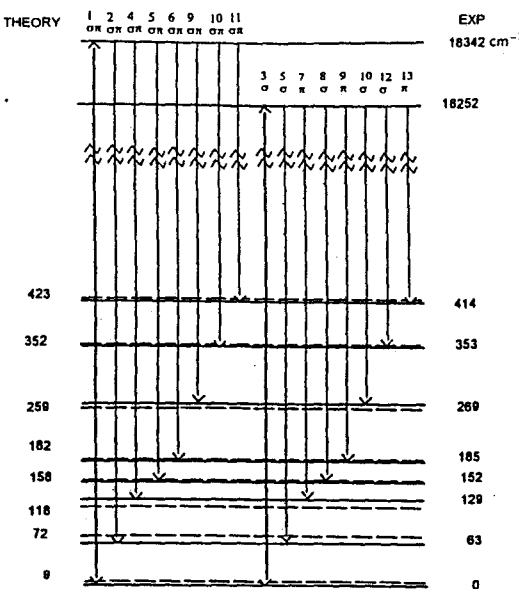


FIG. 4. Levels of $\text{LiNbO}_3:\text{Er}^{3+}$ as obtained from the analysis of the spectra of Figs. 1-3. The numbering allows one to identify the transitions observed by absorption or fluorescence. The polarization allowed is also indicated at the top of each transition.

to the $^4I_{15/2}$ experimental energies. As the number of independent parameters in the crystal-field energy, for the C_3 point symmetry and $4f$ electrons, is 7, and the number of observed levels is of the same order, we needed to make some assumptions. Looking at the crystal sites allowed for the Er^{3+} ion, we see that they can be considered as octahedral, distorted in the direction of the C_3 axis, and with, further, a small tetragonal distortion. On this basis, we wrote the first term in the right hand side

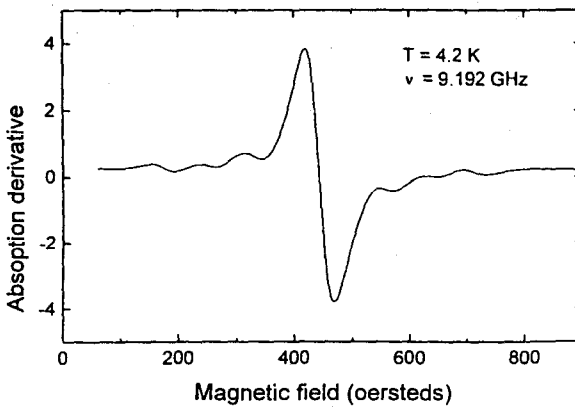


FIG. 5. The $\text{LiNbO}_3:\text{Er}^{3+}$ EPR spectrum, consisting of the lowest doublet resonance. The satellite lines are the hyperfine transitions corresponding with ^{167}Er ($I = 7/2$). The ordinate axis is in arbitrary units.

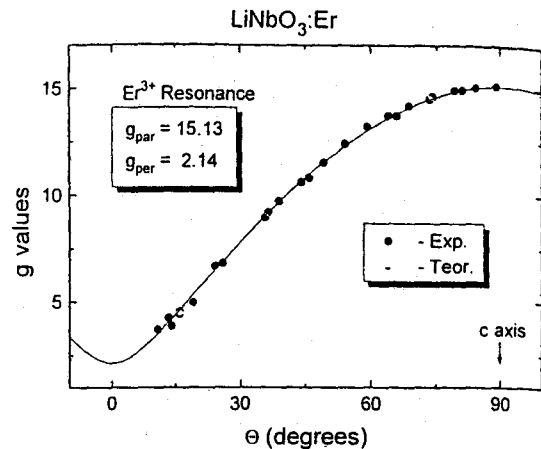


FIG. 6. Angular variation of the central line in Fig. 5. The g values obtained experimentally agree well with those corresponding with the lowest level of Fig. 4 (see text).

of Eq. (1) that corresponds to an axial distortion in the c -axis direction; the second term represents a distortion in the tetragonal direction, and the last two terms are the cubic crystal field. The $O_n^m(c)$ and $O_n^m(s)$ are Stevens' spin operators transforming as the real combinations of spherical harmonics C_n^m and S_n^m tabulated by Prather.⁸ The last two terms correspond to the cubic crystal field, and O_4 and O_6 are the fourth and sixth order cubic linear combinations of operators.⁹ We choose to write down Eq. (1) in the cubic axes, instead of the trigonal axes, for better understanding of the fitting parameters. We obtain

$$\begin{aligned} B_2^0 &= (1.30 \pm 0.05) \times 10^{-1} \text{ cm}^{-1}, \\ B_2 &= (6.51 \pm 0.05) \times 10^{-1} \text{ cm}^{-1}, \\ B_4 &= (5.21 \pm 0.08) \times 10^{-3} \text{ cm}^{-1}, \\ B_6 &= (3.75 \pm 0.10) \times 10^{-5} \text{ cm}^{-1}. \end{aligned}$$

The ESR spectra of Er^{3+} in LiNbO_3 present a single line, accompanied by the corresponding satellites of the ^{167}Er isotope, with $I = 7/2$, as can be seen in Fig. 5. The hyperfine parameter is isotropic, within the experimental error, and its value is $^{167}A = 77 \pm 3$ G. Figure 6 shows the angular variation of the isotope ^{168}Er with the magnetic field in the plane (110) of the crystal. We fit the g values of this transition by $g_{\parallel} = 15.14$ and $g_{\perp} = 2.15$. These values agree within the calculation error with that of a Kramers doublet with a wave function obtained from the diagonalization of the 16×16 crystal-field matrix of Eq. (1) for the lower $J = 15/2$ multiplet. However, the g values obtained are very much dependent on small variations in the crystal-field parameters; for this reason, the induced g shifts originating in the ferroelectricity of the crystals¹⁰ could not be evaluated.

Rutherford backscattering¹¹⁻¹³ and extended x-ray-absorption fine-structure^{14,15} experiments show that the most probable site for the rare-earth impurities is the Li^+ site. The fact that the Li^+ ions are less strongly bonded to the lattice, as is shown in early x-ray diffraction experiments¹⁶ and by thermal reduction of the crystals,¹⁷

es force to this result. XSW experiments by Gog *et al.*⁴ demonstrate, using this powerful spectroscopic technique, that the site occupied is a trigonal site near the site. This is completely confirmed by our experimental results, both optical and ESR. This one is a very sensitive tool to study magnetic impurities, and, as was said above, we did not find any other resonance in our samples. We cannot, from our results, define the site occupied by Er³⁺, but we can be sure that most of the Er³⁺ ions are in only one trigonal site, as Ref. 4 demonstrates.

IV. CONCLUSIONS

Summarizing, we obtained the crystal-field parameters fitting the optical spectra of Er³⁺ in LiNbO₃. From the calculation, we obtained the corresponding ESR *g* values, in good agreement with the experimental data. We observed the optical and ESR spectra corresponding to a single site for the Er³⁺ ion; we conclude that it enters in a trigonal site of the lattice, but we were not able

to decide which is the site. Gog *et al.*⁴ assert that the site occupied by Er³⁺ is that defined by them as site 1. Total energy calculations¹⁸ showed that this site is energetically favorable. We believe that this work completes previous ESR and optical studies of LiNbO₃, and that it can help in future analysis of this system, and induce theoreticians to develop models to explain the distortion about the Er³⁺ ion. This can be useful in the future use of this system for solid state lasers or communications.

ACKNOWLEDGMENTS

The authors acknowledge financial help by Fundação de Amparo à Pesquisa do Estado de São Paulo, Conselho Nacional de Pesquisas, Coordenação de Aperfeiçoamento de Pessoal do Ensino Superior e Financiadora de Estudos e Pesquisas, Brazil. We also thank João Frigo for help with the sample growing and Professor O. R. de Nascimento for suggestions about the ESR experiments.

-
- Permanent address: Dept. de Física, Universidade Federal de Goiás, Brazil.
 N.L. Evlanova, A.S. Kovalev, V.A. Koptskik, L.S. Kornienko, A.M. Prokhorov, and L.N. Rashkovich, JETP Lett. **5**, 291 (1967).
 G. Burns, D.F. O'Kane, and R.S. Title, Phys. Rev. **167**, 314 (1968).
 B. Dischler, J.R. Herrington, A. Rauber, and J. Schneider, Solid State Commun. **12**, 737 (1973).
 Th. Gog, M. Griebenow, and G. Materlik, Phys. Lett. A **181**, 417 (1993), and references therein.
 L. Arizmendi and J.M. Cabrera, Phys. Rev. B **31**, 7138 (1985).
 V.G. Grachev and G.I. Malovichko, Sov. Phys. Solid State **27**, 424 (1985).
 R. Duchowicz, L. Nuñez, J.O. Tocho, and F. Cussó, Solid State Commun. **88**, 439 (1993), and references therein.
 J.L. Prather, U.S. National Bureau of Standards Monograph No. 19 (U.S. GPO, Washington, DC, 1961).
 K.R. Lea, M.J.M. Leask, and W.P. Wolf, J. Phys. Chem Solids **23**, 1381 (1962).
 W.B. Mims, *The Linear Electric Field Effect in Paramagnetic Resonance* (Oxford University Press, Oxford, 1976).

- ¹¹ L. Kovacs, L. Rebouta, J.C. Soares, and M.F. da Silva, Radiat. Eff. Def. Solids **119-121**, 445 (1991).
¹² L. Rebouta, J.C. Soares, M.F. da Silva, J.A. Sanz-Garcia, E. Dieguez, and F. Agullo-Lopez, J. Mater. Res. **7**, 130 (1992).
¹³ L. Rebouta, M.F. da Silva, J.C. Soarez, J.A. Sanz-Garcia, E. Dieguez, and F. Agullo-Lopez, Nucl. Instrum. Methods Phys. Res. Sect. B **84**, 189 (1992).
¹⁴ C. Prieto, C. Zaldo, P. Fessler, H. Dexpert, J.A. Sanz-Garcia, and E. Dieguez, Phys. Rev. B **43**, 2594 (1991).
¹⁵ C. Zaldo, F. Agullo-Lopez, J. Garcia, A. Marcelli, and S. Mobilio, Solid State Commun. **71**, 243 (1989); C. Prieto, C. Zaldo, and J.A. Sanz-Garcia (unpublished).
¹⁶ S.C. Abrahams, J.M. Reddy, and J.L. Bernstein, J. Phys. Chem. Solids **27**, 997 (1966).
¹⁷ A. Garcia-Cabanéz, J.A. Sanz-Garcia, J.M. Cabrera, F. Agullo-Lopez, C. Zaldo, R. Pareja, K. Polgár, K. Raksányi, and I. Földvari, Phys. Rev. B **37**, 6085 (1988).
¹⁸ O.F. Schirmer, O. Theimann, and M. Wöhlecke, J. Phys. Chem. Solids **52**, 185 (1991); H.J. Donnersberg, S.M. Tomlinson, and C.R.A. Catlow, *ibid.* **52**, 201 (1991).

CAPÍTULO 4

**SOLIDIFICAÇÃO DIRECIONAL COM
AQUECIMENTO A LASER**

IV. Solidificação direcional com aquecimento a laser

O processo de solidificação de fibras monocristalinas é constituído de quatro etapas distintas: A primeira é o alinhamento mecânico da semente e do nutriente (pedestal), em seguida, ele é aquecido até que uma pequena região fundida seja formada; a semente é, então, levada em contato com a fase líquida. O puxamento da fibra somente inicia-se quando uma condição estável entre a fusão do nutriente e a cristalização da semente (volume da fase líquida constante) é obtida. Após atingir a condição estável a semente e o pedestal são transladados simultaneamente, com velocidades que podem ser iguais ou não, dependendo do diâmetro final da fibra monocristalina desejada.

Na técnica de crescimento pedestal com aquecimento a laser, mostrado esquematicamente na figura 4.1, a fase líquida mantém-se presa entre duas regiões sólidas (nutriente e semente) por tensão superficial. O crescimento da fibra é, então, um processo controlado pelo menisco.

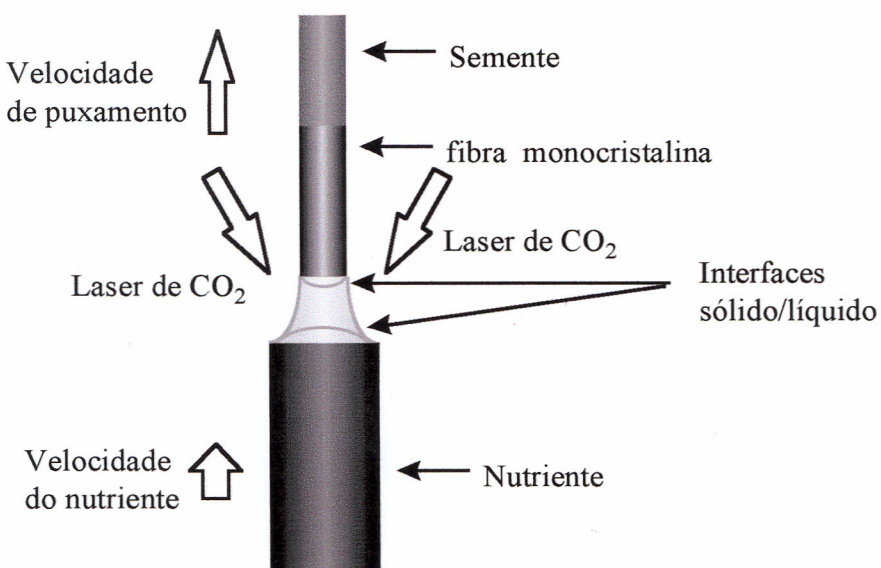


Figura 4. 1 - Representação esquemática do processo de crescimento de fibra com aquecimento a laser.

Um dos problemas operacionais associado com esta técnica é controlar as flutuações de diâmetro da fibra em crescimento devido as perturbações envolvidas no processo. O diâmetro da fibra em crescimento altera-se em resposta a variações no ângulo de contacto entre o valor de equilíbrio e o instantâneo na interface líquido/sólido.

Em solidificação a partir de técnicas de fusão, o parâmetro de controle fundamental está associado aos fluxos de calor. Uma representação esquemática dos vários fluxos de calor existentes durante o processo está ilustrado na figura 4.2. Todo o calor fornecido pelo laser de CO₂ é utilizado para a fusão do material, conduzido por difusão através da fibra e pedestal, irradiado para o ambiente devido à emissão do material e, ainda, perdido por convecção natural para o fluido existente dentro da câmara de crescimento. Somando a este balanço de energia temos o calor de solidificação na interface sólido/líquido.

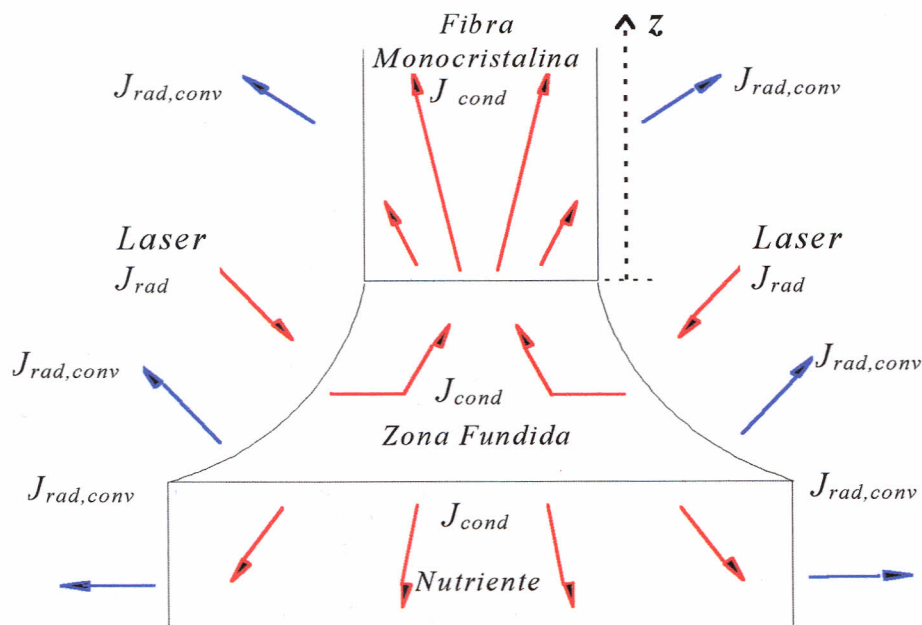


Figura 4.2. - Representação esquemática dos fluxos de calor existentes durante o processo de solidificação. J_{cond} , J_{rad} e o $J_{rad,conv}$ são respectivamente os fluxos de calor por condução, radiação e radiativo mais o convectivo.

Neste processo, podemos considerar a transferência de calor durante a solidificação em uma dimensão como uma primeira aproximação. De uma maneira geral, para um sólido opaco, isotrópico, com interface plana e movendo-se com uma velocidade f , na direção z , a solução da equação de transferência de calor para a temperatura axial em função da distância da interface sólido/líquido e do raio da fibra é dada por [1]:

$$T(z) = T_o + (T_i - T_o) \exp \{-\{[P_t^2 + (Bi_{conv} + Bi_{rad})]^{1/2} - P_t\}(z/a)\}$$

onde T_o é a temperatura do ambiente de crescimento, T_i é a temperatura na interface, P_t é o número de Peclet, Bi_{conv} e Bi_{rad} são os números de Biot convectivo e radiativo e a o raio da fibra. Deste modo, o gradiente de temperatura axial na interface sólido/líquido ($z=0$), que é um importante parâmetro macroscópico de controle do processo de solidificação, é:

$$G'(0) = (dT/dz)_{z=0} = -(T_i - T_o) \{[P_t^2 + 2(Bi_{conv} + Bi_{rad})]^{1/2} - P_t\}(1/a)$$

É interessante ressaltar a dependência explícita do gradiente de temperatura axial na interface de crescimento com o raio do cristal. Um mesmo material crescido com diferentes diâmetros estará, portanto, sujeito a diferentes gradientes de temperatura e, consequentemente, a diferentes velocidades reais de crescimento. Em crescimento de materiais eutéticos, sob condições estacionárias, existe uma relação clássica, $\lambda^2 f = \text{constante}$, entre a velocidade de crescimento (f) e a distância entre as interfases (λ). Portanto, em situações reais, variações na velocidade de crescimento ou no gradiente de temperatura axial

acarretarão em flutuações de diâmetro das fibras, que por conseguinte afetarão a sua microestrutura.

4.1 Artigo: Dielectric crystal growth for devices applications.

4.2 Artigo: Growth of Single Crystal Photorefractive Fibers of $\text{Bi}_{12}\text{SiO}_{20}$ and $\text{Bi}_{12}\text{TiO}_{20}$ by the laser-heated pedestal growth method.

4.3 Artigo: Laser heated pedestal growth of orthorhombic SrHfO_3 single crystal fiber

Bibliografia

- [1] MARCELLO RUBENS BARSI ANDREETA – Implantação da técnica de crescimento de cristais por fusão a laser e a preparação de fibras monocristalinas. Dissertação de mestrado, IFSC – USP, 1996.
- [2] I.A. SANTOS, D.U. SPINOLA, D. GARCIA, J.A. EIRAS, E.R. MANOEL, A.C. HERNANDES, J.A.G. CARRIO, Y.P. MASCARENHAS – Dielectric characterisation of SBN single-crystal fibers and non-doped and La doped ceramics. *Ferroelectrics*, 238 (1-4): 711-718, 2000.
- [3] de VICENTE, A.C. HERNANDES, A.C.de CASTRO, M.F. de SOUZA, M.R.B. ANDREETA, M.S. LI – Photoluminescence spectrum of rare earth doped zirconia fibre and power excitation dependence. *Rad. Eff. Defects in Solids*, 149(1-4):153-157, 1999.
- [4] ARDILA, D.R.; ANDREETA, M.R.B.; CUFFINI, S.L.; HERNANDES, A.C.; ANDREETA, J.P.; MASCARENHAS, Y.P. - SrTiO_3 single crystal fiber grown by Laser Heated Pedestal Growth method: Influence of the ceramic feed rod preparation in the fiber quality. *Materials Research*, 1(1):1-6, 1998.
- [5] ARDILA, D.R.; ANDREETA, M.R.B.; CUFFINI, S.L.; HERNANDES, A.C.; ANDREETA, J.P.; MASCARENHAS, Y.P. - "Laser heated pedestal growth of Sr_2RuO_4 single crystal fibers from SrRuO_3 ". *J. Crystal Growth*, 177 (1-2): 52-56, 1997.

Dielectric crystal growth for devices applications

Antonio Carlos Hernandes

Instituto de Física de São Carlos, Universidade de São Paulo, CP. 369, 13560-970 São Carlos, SP, Brasil
E-mail: hernandes@ifsc.sc.usp.br

ABSTRACT

Recent results of dielectric crystal growth obtained by the Grupo de Crescimento de Cristais (Crystal Growth Group), Universidade de São Paulo, are reported. Related in this review are the specific features of the experimental conditions required to obtain $\text{Bi}_{12}\text{TiO}_{20}$, L-arginine phosphate semiorganic material and oxide single crystal fiber by Laser Heated Pedestal Growth.

INTRODUCTION

Dielectric crystals, which have long been researched for different purposes, are very important in many technological applications. Of these, one class consists of the nonlinear-optic crystals that are usually prepared by the melt and solution techniques. However, laser technology has long been applied in the preparation of a wide range of materials and devices, particularly for dielectric crystals such as sapphires. In this review paper, recent results of dielectric crystal growth obtained by the Crystal Growth Group, at the University of São Paulo, will be reported. The focus will be on the study of the

experimental conditions required to obtain bulk crystal and single crystal fibers of a quality suitable for the development of solid state devices.

1. LASER TECHNOLOGY APPLIED TO CRYSTAL GROWTH

The characteristics that make laser radiation so attractive for this purpose are its coherence and collimation, which permit adjustment of energy distribution with conventional optical elements and placement of the heat source outside the preparation chamber. Currently, the main applications of laser materials processing technology are in the areas of perforation, cutting and welding, sintering, surface thermal treatment, unidirectional solidification applied to single crystal fiber growth, material textures, and the production of aligned eutectic materials. Up to 1980, the laser heated technique applied to crystal growth used only two laser beams focused on the source material [1]. This condition generated a high radial thermal gradient in the molten zone, which caused process instability. Even the four-beam techniques [2] did not solve the problem, although they did improve the growth process. The main

contribution to the laser heated crystal growth technique was made by Fejer et al.[3], who incorporated a special optical component known as the *reflaxicon*, consisting of an inner cone surrounded by a larger coaxial cone section, both with a reflecting surface, that converted the cylindrical laser beam into a larger diameter hollow cylinder surface. This optical component permits radial distribution of energy over the molten zone, reducing the radial thermal gradients.

The Laser Heated Pedestal Growth (LHPG) technique has become one of the most powerful tools in both new and conventional materials research [2-8]. The advantages of this crystal growth technique are its high pulling rates (60 times greater than the conventional Czochralski technique) and the possibility of growing very high melting point materials. Moreover, it is a crucible-free technique, allowing for the growth of high purity single crystals and avoiding mechanical stress and contamination from the crucible during the growth process. Another important factor is the possibility it offers of obtaining metastable phases resulting from the high thermal gradients generated at the solid/liquid interface, which are caused by the extremely localized heat source.

In addition to all the advantages the LHPG technique offers, the crystal's geometric shape, its flexibility in small diameters and its low cost make single crystal fibers (SCF) produced by LHPG even more suitable to replace many of today's bulk devices, particularly with respect to the high melting point materials. However, the SCF must have equal or superior optical and structural qualities when compared to the bulk devices in order to substitute them. Understanding the growth process is a must to ensure and improve SCF

quality.

1.1 - Fiber growth equipment

At the Grupo de Crescimento de Cristais (Crystal Growth Group), University of São Paulo, work on the growth of single crystal fibers began in 1992 with the implementation of the LHPG technique similar to the system developed by Feigelson [2]. Our LHPG system uses a CO₂ laser (CW, $\lambda=10.6 \mu\text{m}$) with nominal controlled power ranging from 0 to 100 W. The laser cavity is water cooled by means of a closed loop system and the temperature is maintained at (19.0 ± 0.5) °C. An He-Ne laser, propagating parallel to the CO₂ laser beam, is used as a guide in the optical alignment. The laser beams are guided into a stainless steel chamber through a ZnSe window. The two laser beams hit the *reflaxicon*, where they are diverted, as explained earlier, onto a cylindrical surface, which is then guided onto a spherical mirror, from where it is focused onto the source material, **figure 1**. The spherical mirror has a hole in its center to allow the seed holder to be held in its optical axis and to avoid the deposition of vapour material in the optical system. The stainless steel chamber allows crystals to grow under a controlled atmosphere (special gases or vacuum) and to see the molten zone through magnifying lenses or with a video system mounted 90 degrees off-axis from the first one. The video system has a microscope attached to it that provides a view of the molten zone and can also be used for diameter control. In the case of transparent materials, the interface shape can be observed directly during growth. Our system does not allow rotation of either the fiber or the source rod. The pulling rate can be changed in the 0,01-10

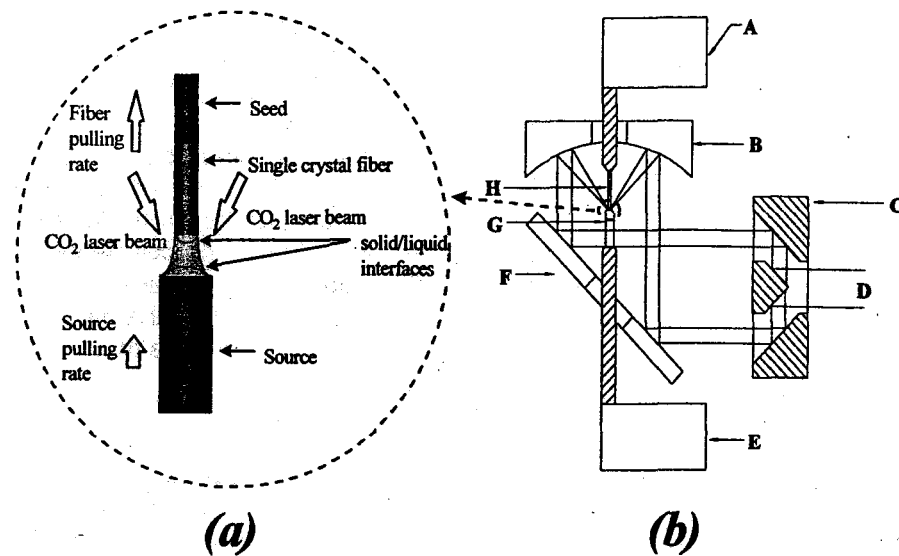


Figure 1 - Schematic drawing of the Laser Heated Pedestal Growth technique. (a) The growth process; (b) The focalization system. A is the pulling system; B is a spherical mirror; C the reflexicon; D the laser beam; E is the pedestal pulling system; F is a plane mirror; G the source material, and H is the single crystal fiber.

mm/min range.

1.2 - Source and seed preparation

The source material (pedestals) used to grow SCF can be prepared either by cutting a previously bulk grown crystal or ceramics, or it can be produced by the cold extrusion process. In the cold extrusion process, an organic solvent is added to the material until it reaches a plastic-like consistency, which is then forced through a 5 mm long and 1 mm diameter stainless steel tube using a manual press. This source material does not need to be cut, as it already has a convenient geometric shape. It is allowed to dry at an ambient temperature and atmosphere for 3 hours, and can then be used to grow the crystal.

This method for producing source materials offers many advantages over the conventional methods, i.e. the small amount of materials needed and the possibility of producing reagent source rods (green-rods). When green-rods are used in the LHPG system, three of the material preparation steps (synthesis, sinterization and crystal growth) are reduced to just one. Figure 2 shows the diameter reduction of the $ZrO_2 \cdot Y_2O_3$ green-rod as a function of the distance from the melting interface. The synthesis and sinterization process only starts near the melting interface (below 1000 μm). The seeds can be prepared from a bulk single crystal, whenever possible, or from pedestal ceramics. In the latter case, is necessary to form a little neck to obtain a

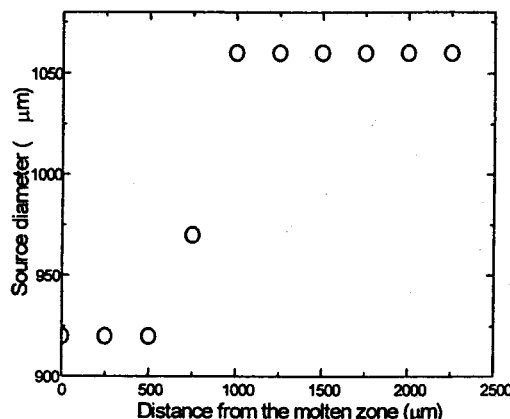


Figure 2 - $\text{ZrO}_2:\text{Y}_2\text{O}_3$ source diameter variation as a result of the molten zone distance. The diameter decreases near the molten zone, indicating that a sinterization process is occurring.

single crystal fiber.

1.3 - Crystal Growth

In the LHPG technique, the growth process comprises four different steps. The first step is mechanical alignment between the seed and source material, after which the CO_2 laser is powered on, slowly heating the source until it melts. The seed is then lowered to touch the molten material. The actual growth process starts only after wetting and temperature equilibrium is reached. After that, the seed and source starts its upward movement at speeds that may be either equal to or different from each other, depending on the desired single crystal fiber diameter and according to some conditions that will be discussed below. All growth systems are mounted over a damped optical table to avoid mechanical vibrations.

The growth of a controlled diameter SCF requires a stable molten zone volume and

shape. In this growing process, three basic conditions must be fulfilled in order to achieve a steady state:

(i) Mass conservation

The mass flux that reaches the growing interface must be equal to the mass that leaves the source-melting interface. Considering that there is no loss by evaporation and that the density of solids is constant, we can state that:

$$V_p = V_s (A_s/A_f) \quad (1)$$

V_p is the fiber pulling rate, V_s is the source pulling rate, and A_f and A_s are the transversal section areas of the fiber and source, respectively. The A_s/A_f ratio is known as the reduction ratio and is an important experimental parameter.

(ii) Stability of the molten zone shape

The stability of the molten zone shape is controlled mainly by the surface tensions at the solid-liquid-gas junction. If one considers a cylindrical shape, one can neglect surface tension dependence with respect to the crystallographic orientations. One can then find an analytical expression for the wetting angle, for the equilibrium of the three coexisting surface tensions is expressed thus:

$$\cos \varphi_0 = (\sigma_{l,g}^2 + \sigma_{s,g}^2 - \sigma_{s,l}^2) / (2\sigma_{l,g}\sigma_{s,g}) \quad (2)$$

where $\sigma_{l,g}$, $\sigma_{s,g}$ e $\sigma_{s,l}$ are the liquid/gas, solid/gas and solid/liquid surface tensions, respectively, and φ_0 is the wetting angle at which an equilibrium between the three surface tensions is achieved. For lithium niobate, for example, this wetting angle is considered to be 4° and can be achieved by controlling the fiber-source reduction rate.

(iii) Energy conservation at the growth interface

The heat flux entering the crystal through the growing interface (J_s) must be equal to the latent heat of crystallization (J_c) plus the heat flux on the liquid through the interface (J_l). Thus, considering a flat interface:

$$J_s = J_c + J_l \equiv \rho_s \Delta H_f V + K_l G_{s,i} = K_s G_{l,i} = \text{cte} \quad (3)$$

where ρ_s is the solid density, ΔH_f is the latent melting heat, K_l and K_s are the thermal conductivities of the liquid and solid, respectively, and V , $G_{s,i}$ and $G_{l,i}$ are, respectively, the growth rate, the temperature gradient at the solid interface and the temperature gradient at the liquid interface. If one considers that the temperature gradient in the liquid is negligible compared to the temperature gradient in the solid, one obtains:

$$\rho_s \Delta H_f V = K_s G_{s,i} = \text{cte} \quad (4)$$

These considerations indicate that the crystal growth rate is controlled by the extraction of latent heat from the interface. Without heat extraction there is no solidification. In the LHPG system there is a high axial thermal gradient at the growing interface due to localized heat and it is, therefore, possible to extract a large amount of heat (high crystal pulling rate). The axial thermal gradient in the solid/liquid interface can be estimated considering the heat fluxes in a semi-infinite cylinder moving at speed V in the z direction [9,10]:

$$G_{s,i} = - (T_r - T_o) \{ [P_c^2 + 2Bi]^{1/2} - P_c \} / (1/a) \quad (5)$$

where T_o is the temperature in the surroundings of the growing crystal, T_r is the solid/liquid interface temperature, a is the

fiber radius, P_c is the Pécelt number, defined as $\rho c_p V a / 2 K$, where ρ is the solid density, c_p is thermal capacity and K is solid thermal conductivity, $Bi = ha$ is the total Biot number and h is the effective cooling constant (convective + radiative). It is interesting to note that a given material grown with a different fiber radius has different solid/liquid interface temperature gradients that could affect the growth process by introducing high thermal stress.

1.4 – Materials studied

As stated previously, the LHPG technique is a very powerful tool for producing single crystals of various compounds for evaluation. An important characteristic is the ability to grow incongruently melting and evaporating materials. The growth of incongruently melting bulk oxide single crystals is usually carried out by the high temperature solution growth, which is a slow and complicated technique. The source material in this technique must be rich in one or more elements to compensate the incongruent melt, as we will see from $\text{Bi}_{12}\text{TiO}_{20}$ bulk crystals.

By using the LHPG technique, one can grow materials such as $\text{Bi}_{12}\text{TiO}_{20}$ (BTO), for example, without the need to enrich the source with an excess of Bi_2O_3 [4,6,7]. In other words, it is possible to grow incongruently melting materials from a source with the same composition of the grown crystal. This result, at first glance, contradicts the phase diagram. However, there are two hypotheses to explain this effect. The first was suggested by Saifi et al. [13], who proposed the growth of BaTiO_3 using the tetragonal seed structure of SrTiO_3 , in which the BaTiO_3 grew epitaxially and, owing to the high temperature gradients, the tetragonal phase of BaTiO_3

was frozen, allowing for the growth of tetragonal BaTiO_3 . Another hypothesis, propounded by Feigelson [2], considers that the liquid composition in such growth experiments changes gradually until it naturally reaches the composition needed for crystal growth, according to the phase diagram. This indicates that, at the beginning of the process, the solid must have a different composition from the stoichiometry to allow the liquid phase to change gradually. Indeed, both mechanisms could act together, depending on the materials to be considered. In the case of $\text{Bi}_{12}\text{TiO}_{20}$ growth, where a $\text{B}_{12}\text{SiO}_{20}$ seed was used, we also measured a change in the liquid composition from stoichiometry, figure 3. Using the LHPG technique, it was possible to grow single crystal fibers of 300 to 1200 μm in diameter and up to 70 mm in length. The pulling rates typically used in this process were 6 to 18 mm/h , much higher than the few millimeters

per day in the high temperature solution methods.

Another interesting result arising from the LHPG characteristics is the additional possibility of growing materials with incongruent evaporation, such as Sr_2RuO_4 . To date, the conventional method for growing Sr_2RuO_4 single crystals was the floating zone melting method. However, due to the high evaporation rates of the Ru_2O_3 , single crystals of a few millimeters have been grown. Using the LHPG technique and an extruded reacted powder material of SrRuO_3 composition as a source, it was possible to grow crystals of up to 30 mm in length and 0.8-1.0 mm in diameter [5]. This was possible due to the high temperature gradients at the interface, allowing for higher growth speeds than in the conventional floating zone technique. Moreover, only a small amount of material remains at a high temperature for a short period of time, thus minimizing the ruthenium oxide evaporation. By changing

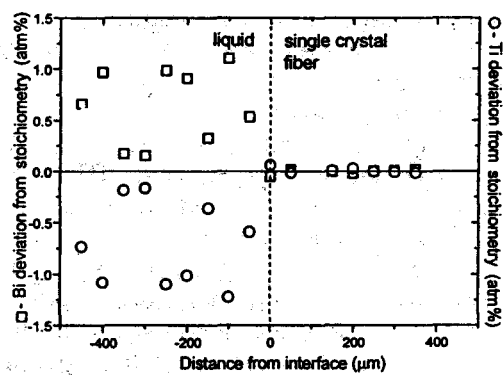


Figure 3 - Energy Dispersive X-Ray composition measurements of the $\text{Bi}_{12}\text{TiO}_{20}$ fiber grown by LHPG and of a part of the frozen molten zone. Only the stoichiometric composition deviation is shown. An excess of Bi_2O_3 in the molten zone predicted by the phase diagram can be seen.



Figure 4 - $\text{GdAlO}_3:\text{Yb}^{3+}$ single crystal fiber grown in our LHPG equipment.

the pulling and, particularly, the source velocity, it was possible to compensate the evaporation of ruthenium. The best results were obtained with pulling rates of 0.3 mm/min, with a feeding rate (source) of 0.4 mm/min.

Other different dielectric oxide materials have been grown by the LHPG technique by our Crystal Growth Group, among them pure and doped $\text{Bi}_{12}\text{SiO}_{20}$, $\text{Bi}_{12}\text{GeO}_{20}$, Bi-Sr-Ca-Cu-O , LiNbO_3 , LiTaO_3 , Al_2O_3 , SrTiO_3 , SrHfO_3 , $\text{ZrO}_2\text{:Y}_2\text{O}_3$, GdAlO_3 , LaAlO_3 , $\text{Y}_3\text{Fe}_5\text{O}_{12}$ and some eutectic compounds such as $\text{GdAlO}_3\text{:Al}_2\text{O}_3$, $\text{ZrO}_2\text{:CaO}$. As an example, figure 4 shows a $\text{GdAlO}_3\text{:Yb}^{+3}$ single crystal fiber grown in our equipment.

1.5 – Critical fiber diameter

The effect of the steep temperature gradient on fiber growth for sillenite single crystal fiber was recently reported by us [6,7]. Moreover, using 40 mm long and 300-1200 μm diameter LiNbO_3 single crystal fibers pulled along the c axis, with a reduction rate of 1.7 between the source and fiber, we were able to measure these high thermal gradients at the solid/liquid interface [12,13]. The measurements of the temperature profile during the single crystal growth process were taken using a 60 μm diameter Pt-Pt10Rh thermocouple in an ambient atmosphere. After stabilization of the temperature and wetting, the pulling process was initiated and the thermocouple was then trapped in the solid phase as the growing process proceeded. One important parameter to calculate the temperature gradient is the ambient temperature. This temperature was also measured in the same way as the crystal temperature profile, but in this case, the thermocouple was at an approximate distance of 1 mm, radially, from the fiber surface.

Ambient temperature values were obtained by averaging the temperature over a distance of 1 mm from the solid/liquid interface, but no dependence on the fiber radius could be predicted by our data. The average ambient temperature value for different fiber radii was found to be $T_0 = 370 \pm 50^\circ\text{C}$. This value was used as a starting value for the experimental axial profile fitting based on **equation 5**. The effective cooling constant found by our data was equal to $(0.8 \pm 0.1) \text{ cm}^{-1}$. This result is different from that determined for the Czochralski LiNbO_3 single crystal growth process (0.5 cm^{-1}) [10]. This is understandable when one considers that, in this process, the loss of heat to the ambient is much higher than in the conventional Czochralski growth technique, with all its thermal shields. The high temperature gradient at the growing interface is responsible for the high pulling rate in this technique, as shown earlier, in **equation 4**, allowing it to be counted by one millimeter per minute instead one millimeter per hour, which is the typical pulling rate for conventional crystal growth methods.

Thermal stress generated by a steep temperature gradient in the solid/liquid interface is the main cause of defects and cracks in grown single crystal fibers. The fiber cracks when the thermal stress (ϵ) exceeds the breaking strength of the material (ϵ_b) during the growth process. Based on an approximate temperature distribution in a cylindrical crystal geometry, Brice [10] has shown the existence of a maximum thermal gradient that the material can handle before it cracks. This maximum thermal gradient can be expressed, in our case, as:

$$\left(\frac{dT}{dz} \right)_{\max} = \frac{4\epsilon_b}{\alpha(a)^2} \sqrt{\frac{1}{h}} \left(1 - \frac{1}{2}ha \right) \quad (6)$$

where α is the linear expansion coefficient. The dependence of the thermal gradient at the solid/liquid interface and the maximum thermal gradient are shown in figure 5. One can clearly see that there is a critical radius (a_c) which, if exceeded, causes the fiber to crack due to the high thermal gradients in the solid/liquid interface. In the case of LiNbO_3 , this critical radius was found to be $460 \pm 20 \mu\text{m}$. Fibers with radius values below $460 \mu\text{m}$ were obtained without any cracks.

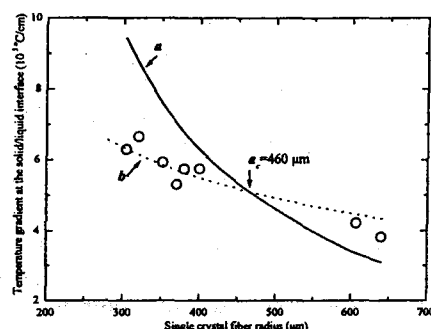


Figure 5 - Temperature gradient at the solid/liquid interface during LiNbO_3 single crystal fiber growth. The dashed line represents the maximum thermal gradient that the material can handle before it cracks and the continuous line is the fitting of the temperature gradient measurements based on equation 5. a_c is the critical radius.

2. $\text{Bi}_{12}\text{TiO}_{20}$ BULK CRYSTAL

Bismuth oxide (Bi_2O_3) is an interesting dielectric material with potential applications such as optical coatings, in metal/insulator/semiconductor (MIS) capacitors and integrated microwave circuits [14]. The Bi-O system is rather complicated and can have four different

main crystalline phases, usually indicated by the letters α , β , γ and δ . Recently, a new polymorphic form of Bi_2O_3 with the A-type rare-earth sesquioxide structure was synthesized by a high-pressure technique [15]. Each of these phases has different electrical and optical properties [16]. The γ -phase bismuth oxide is a very important material for optical applications when stabilized at room temperature. The γ -phase can be stabilized by adding some ions to its crystalline structure. When this is done, the resulting compounds are known as sillenite, named after Sillen, who discovered this special class of materials [17,18].

Sillenite crystals are of the $\text{Bi}_{12}\text{MO}_{20}$ type, where M = Si, Ge, Ti and others, and crystallize in the I23 space group. They have a number of interesting properties, including piezoelectric, electro-optical, elasto-optical, optical activity and photoconductivity. Of particular interest is the combination of electro-optical and photoconductivity properties, which results in the so-called photorefractive effect, consisting of a reversible light-induced change in the refractive index [19]. Because of these properties, sillenite crystals are useful for many advanced and potentially promising applications, such as a reversible recording medium for real-time holography or for image processing applications [20,21]. Bismuth titanium oxide, $\text{Bi}_{12}\text{TiO}_{20}$ (BTO), has some practical advantages in terms of its isomorphous $\text{Bi}_{12}\text{SiO}_{20}$ (BSO) and $\text{Bi}_{12}\text{GeO}_{20}$ (BGO), including lower optical activity, higher electro-optic coefficient and increased sensitivity to red light [21].

2.1- Crystal growth

Few studies have been made of the BTO

crystal [22-26], which is probably due to the difficulties associated with the preparation of this crystal. BTO melts incongruently and its growth presents specific characteristics and additional difficulties when compared to BGO and BSO. Consequently, the definition and control of growth parameters to obtain good single crystals are more critical.

We prepared BTO crystals using a resistive heating furnace equipped with an 808 Eurotherm microprocessor-based digital temperature controller unit attached to a Pt-Pt10%Rh thermocouple. The temperature fluctuations were typically lower than 0.2°C, as measured near the crucible. To evaluate the temperature gradient in the solid-liquid interface we measured the axial temperature profile through the crystal during growth. A measurement configuration was used in which the thermocouple was attached to the cold-finger with its extremity centralized below the seed and the set dipped in the liquid and then quickly pulled with the thermocouple attached to the growing crystal. The axial temperature gradient at the crystal-melt interface determined was about 16 °C/cm.

BTO single crystals were grown by the pulling technique from high temperature nonstoichiometric solutions, with the composition $10\text{Bi}_2\text{O}_3\cdot1\text{TiO}_2$ [27,28], using high purity cylindrical platinum crucibles. BTO seeds oriented along the [001] direction, held in a pure platinum seed holder, were used to initiate the crystal growth. All runs were carried out in air. Pulling rates between 0.10 and 0.25 mm/h and 20 to 30 rpm rotation rates were used.

2.2 – Crystal defects

The BTO growth process can be divided

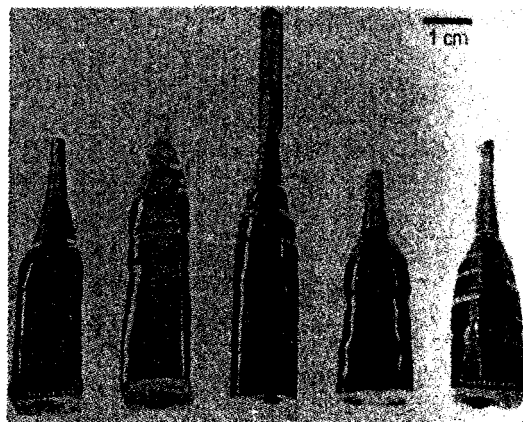


Figure 6 - BTO single crystals grown by the pulling technique from high temperature nonstoichiometric solutions, with the composition $10\text{Bi}_2\text{O}_3\cdot1\text{TiO}_2$.

according to the different stages of evolution of the solid-liquid interface shape. In the initial stage, during the crystal shoulder formation, the interface is faceted and convex toward the liquid. In this stage, crystals grown in the <100> direction typically showed the (110) and (100) facets at the solid-liquid interface, with the (110) facets being more developed. After this stage, the as yet convex interface changes from a faceted to a rounded shape. This is the last geometry of the interface before the transition to the convex-flat interface shape. The interface shape remains flat during the stationary diameter phase, but it can change to a slightly concave shape, depending on the diameter and length of the crystal. **Figure 7** shows a picture of a BTO obtained using an optical microscope with polarized light, where the striation pattern shows the interface shape in the stage where it is convex and faceted. The interface shape transition generally occurs abruptly with re-melt of the crystal,

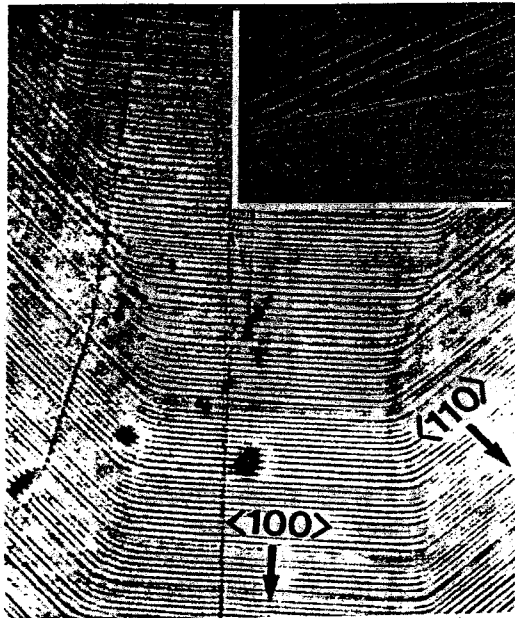


Figure 7. - The interface shape in the stage where it is convex and faceted, as revealed by the striation pattern. *Inset:* discontinuity of the striation pattern, revealing an abrupt interface shape transition. The pictures were obtained with an optical microscope with low intensity polarized light.

as was revealed by the discontinuity of the striation pattern (see insert in figure 7). In some cases, the transition can occur without evidence of an abrupt change in the interface shape. The transition tends to be smoother for crystals with larger shoulders, that is, with a lesser angle of the meniscus and with a crystal/crucible radius ratio under 0.5. Without these experimental conditions, an abrupt interface shape transition occurs and inclusions can appear in the crystal's periphery.

In agreement with previous BSO and BGO [29,30] results, we verified that the core

occurs in BTO crystals only when the interface is convex toward to the liquid. There was a darker central column in the growth direction [100] with the same diameter of the facet (100) that was present in the crystallization front. The core disappeared after the interface shape transition from convex to flat. Typically, the core presented a diameter of 1 to 3 mm in the first 15 to 20 mm of crystal length, which was eliminated only with a flat growth interface.

3. SEMIORGANIC CRYSTAL

L-arginine phosphate monohydrate ($C_6H_{14}N_4O_2H_3PO_4 \cdot H_2O$, known as LAP) is a highly transparent monoclinic crystal (space group $P2_1$; $a = 10.85 \text{ \AA}$; $b = 7.91 \text{ \AA}$; $c = 7.32 \text{ \AA}$; $\beta = 98^\circ$; $Z = 2$ [31]) with attractive properties for the efficient frequency conversion of infrared lasers [32,33]. LAP has been proposed as a replacement for KDP in many applications due to its higher nonlinearity, high damage threshold and low level of hygroscopicity [34]. However, since L-arginine is an amino acid, it is a very good biological nutrient for microorganisms. Therefore, solutions of LAP are a natural food reservoir for these microorganisms and their presence in the growth chamber leads to problems such as the coloration of the solution and a reduction in the quality of the crystals obtained [34, 35]. We have defined a chemical doping, sodium azide (NaN_3), that ensure the absence of any microorganism colonies for long periods (up to six months) without any solution maintenance [36,37].

3.1 - Crystal growth system

The crystals were grown by the isothermal solvent evaporation method, using an

accurately controlled solvent evaporation technique (ACSET). Figure 8 shows a schematic diagram of the crystal growth chamber. The crystal growth vessel in our system consists of a quartz crucible with a volume of 1000 cm^3 for the solution and a condensation head consisting of a conical surface located at the top of the growth chamber. A flux of cooling water at the top of the head keeps the temperature at a level suitable for solvent condensation. The condensed solvent slides down the internal condenser wall until it reaches a roof gutter in the conic base, when it is removed to a graduate burette (0.05 ml precision), which enables the volume of the evaporated

solvent to be measured. The rate of solvent evaporation is determined by measuring the time it takes for the volume to evaporate.

In ACSET, the solution is at the thermal bath (T_b) temperature while the condensation head is at a lower temperature (T_c). The solvent evaporated from the higher vapor pressure region near the solution surface, at a T_b temperature, moves toward the lower vapor pressure region in the condensation head, at the T_c temperature, where it is condensed. Solvent evaporation is controlled by conveniently adjusting the temperature difference ($T_b - T_c$). Since the bath temperature is kept constant, which is convenient for minimizing thermal stress in the LAP crystals, crystal growth rate control is achieved by adjusting the T_c temperature of the condensation head.

A seed holder with a cross-shaped profile allows one to sink four seeds into the solution, allowing four crystals to be grown simultaneously. The seed holder is permanently rotated back and forth by a transmission rod mechanically attached to an electric motor that provides rotating and stirring movements.

3.2 - Solution preparation

LAP saturated solutions were prepared by dissolving equimolar amounts of the components in 0.03 M of an azide aqueous solution. The pH value of the stoichiometric solution was adjusted at 4.25 and no purification process was made prior to the growth run. The solutions were filtered and, before being placed in the growth chamber (GC) located in a thermostatic bath, they were kept for one hour at a temperature above that of saturation. The seed holder, containing four high quality seeds, was placed in the GC without any initial contact

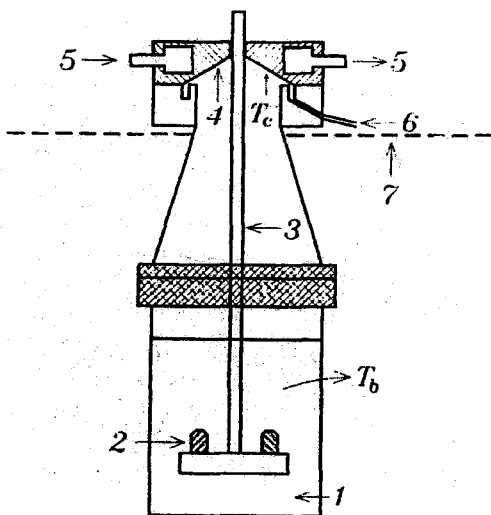


Figure 8 – Schematic diagram of the crystal growth chamber. 1: saturated solution, 2: crystal, 3: seed holder, 4: conical condensation surface, 5: water flux to control the temperature T_c , 6: exit of evaporated water to graduated burette, 7: level of thermal bath (T_b).

with the solution. After the system achieved thermal equilibrium, the seeds were slowly lowered into the solution and rotation was initiated. The seeds used in all runs were previously prepared by spontaneous nucleation at room temperature.

To verify the efficiency of sodium azide in LAP growing experiments, we prepared solutions with different sodium azide concentrations and allowed them to evaporate at room atmosphere. For the LAP solution without sodium azide, a large number of colonies appeared in a period of 20 to 30 days while, with sodium azide, the solutions remained free of microorganisms for a period of over 150 days. No maintenance was provided for the solutions during this time.

3.3 - Crystal growth

A typical evaporation curve for the growth of LAP crystals is shown in figure 9. At first, a small constant temperature difference ($T_b - T_c$) was carefully maintained to avoid unstable growth due to small free areas of the seeds and spurious nucleation. During

the growth process, the difference was slowly increased to keep the solution supersaturated. The optimum evaporation program was adjusted after a few experiments, according to the solubility data previously obtained.

The LAP crystals obtained were colorless, as shown in figure 10, and morphologically very similar to those of references [35] and [38]. In general, the LAP crystals exhibit fourteen faces, with their relative development in the order of {100} > {101} > {110} > {011} > {001} > {201} > {001} > {111}. LAP crystals grown using sodium azide as a microorganism inhibitor indicate that no detectable change in the optical physical properties occurred [36].

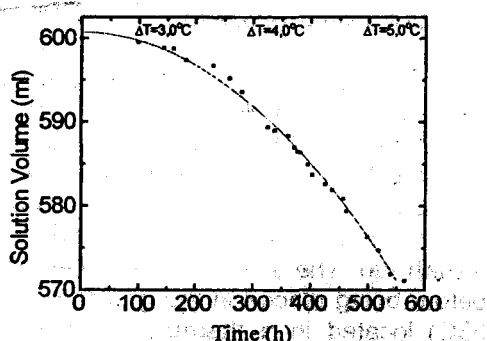


Figure 9 - Typical evaporation curve of the LAP crystal growth process. ΔT stands for $(T_b - T_c)$, see text. The line serves to guide one's eyes.

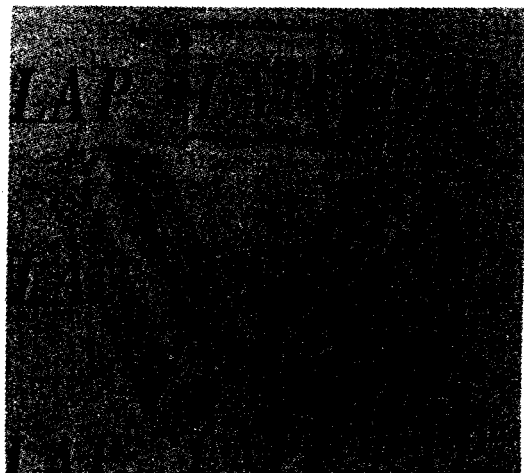


Figure 10 - LAP single crystal grown from the aqueous solution.

ACKNOWLEDGEMENTS

I would like to express my appreciation to the Brazilian agencies FAPESP, FINEP, CAPES and CNPq for their financial support

of our research work and of the development projects of the Crystal Growth Group, University of São Paulo. I also extend my sincere thanks to my students and collaborators, to whose efforts and dedication I attribute our success.

REFERENCES

- (1) Burrus, C. A., Stone, J. 1975, *Appl. Phys. Lett.*, 26, 318.
- (2) Feigelson, R. S. 1985, Growth of fiber crystals, in: "Crystal Growth of Electronic Materials", ed. Kaldus E., North-Holland, 127.
- (3) Fejer, M. M., Byer, R. L., Feigelson R., Kway W. 1982, Proc. SPIE, Advances in Infrared Fibers II, 320, 50.
- (4) Prokofiev V. V., Lima, C. J., Andreeata, M. R. B., Hernandes, A. C., Carvalho, Andreeata, J. P., Kamshilin, A. A., e Jaaskelainen, T. 1994, *J. Crystal Growth*, 137, 528.
- (5) Ardila, D. R., Andreeata, M. R. B.; Cuffini, S. L., Hernandes, A. C., Andreeata, J.P., Mascarenhas, Y. P. 1997, *J. Crystal Growth*, 177, 52.
- (6) Prokofiev V. V., Lima, C. J., Andreeata, M. R. B., Hernandes, A. C., Carvalho, J.F., Andreeata, J. P., Kamshilin, A. A., Jaaskelainen, T. 1995, *Optical Material*, 4, 433.
- (7) Prokofiev, V.V., Lima C. J., Andreeata M. R. B., Hernandes A. C., Carvalho J.F., Kamshilin A. A., Jaaskelainen T. 1995, *Optical Materials*, 4, 521.
- (8) D. Reyes Ardila, M.R.B. Andreeata, S.L.Cuffini, A.C.Hernandes, J.P. Andreeata, Y.P. Mascarenhas. 1998, *Materials Research*, 1, 11.
- (9) Tiller, W. A. 1991, "The science of crystallization - Macroscopic phenomena and defect generation", Cambridge University Press.
- (10) Brice, J. C. 1997, *Phyllips tech. Rev.*, 37, n.9/10, 250.
- (11) Saifi, M., Dubois, B., Vogel, E.M., Thiel, F. A. 1986, *J. Mater. Sci.*, 452.
- (12) Andreeata, M.R.B. 1996, Master thesis, IFSC/Universidade de São Paulo.
- (13) Andreeata, M.R.B. 1999, Materials Research, submitted.
- (14) M.Schuisky, A.Härsta. 1996, *Chem. Vapor Deposition*, 2, 235.
- (15) T.Ato, H.Faqir, M. Kikuchi, H. Chiba and Y. Syono. 1998, *Mat. Res. Bull.*, 33, 289.
- (16) G.Bandoli, D.Barreca, E.Brescacin, G.A.Rizzi and E.Tondello. 1996, *Chem. Vapor Deposition*, 2, 238.
- (17) E.M.Levin and R.S.Roth. J. 1964, Res. Nat. Bureau of Standards- A. Physics and Chemistry, 68A, n.2, 189.
- (18) E.M.Levin and R.S.Roth. 1964, J. Res. Nat. Bureau of Standards- A. Physics and Chemistry, 68A, n.2, 197.
- (19) K.Buse. 1997, *Appl. Phys. B*, 64, 273.
- (20) K.Buse. 1997, *Appl. Phys. B*, 64, 391.
- (21) L.Arizmendi, J.M.Cabrera and F.Agulló-López. 1992, *Internat. J. Optoelectronics*, 7, 149.
- (22) Y. Okano, H. Wada, T. Fukuda, S. Miyazawa. 1991, *Jap. J. Applied Physics*, 30, L1307.
- (23) M.Gospodinov, S.Haussihi, P.Sueshtarov, S.Dobreva, A.Sampil. 1992, *Mat. Res. Bull.*, 27, 1415
- (24) T.S.Yeh, L.J.Hu, S.L.Tu, S.J.Yang, S.E.Hsu. 1993, *J.Appl.Phys.* 73, 7872.
- (25) F.Mersch, K.Buse, W.Sauf, H.Hesse, E.Kratzig. 1993, *Phys.Stat.Sol. (a)*, 140, 273.
- (26) Carvalho, J.F., Hernandes, A.C., 1999, *J. Crystal Growth*, submitted.
- (27) J.Frejlich,E.deCarvalho,A.A.Freschi,J. P.Andreeata,A.C.Hernandes,J.F.Carvalho,N.J.H.Gallo.1996, *Proceedings of the SPIE*, 2868, 205.

- (28) V.V.Prokofiev, J.F.Carvalho, J.P.Nadreeta, N.J.H.Gallo, A.C.Hernandes, J.Frejlich, A.A.Freschi, P.M.Garcia, J.Maracaiba, A.A.Kamshilin, T.Jaaskelainen. 1995, Cryst. Res. Technol., 30, 171.
- (29) P.J.Picone, J. 1988, J.Crystal Growth, 87, 421.
- (30) M.T.Santos, L.Arizmendi, D.Bravo, E.Diéguex. 1996, Mat. Res. Bull., 31, 389.
- (31) K. Aoki, K. Nagano, Y. Itaka. 1971, Acta Cryst., B27, 11.
- (32) S.B. Monaco, L.E. Davis, S.P. Velsko, F.T.Wang; D. Eimrel. 1987, J. Crystal Growth, 85, 252.
- (33) D. Eimrel, S. Velsko, L. Davis, F. Wang, G. Loiacono, G. Kennedy, IEEE J. Quantum Electron. 25, (1989), 179.
- (34) A. Yokotani, T. Sasaki, K. Fujioka, S. Nakai, C. Yamanaka, J. Crystal Growth, 99, (1990), 815.
- (35) G. Dhanaraj, T. Shripathi, H.L.Bhat, J. Crystal Growth, 113, (1991), 456.
- (36) J.F. Carvalho, A.C.Hernandes, F.D. Nunes, L.B.O.A. de Moraes, L. Misoguti, S.C. Zilio. 1997, J. Crystal Growth, 173, 487.
- (37) L.B.O.A. de Moraes. 1998, Master thesis, IFSC/Universidade de São Paulo.
- (38) K. Sangwal, S. Veintemillas-Verdaguer, J. Torrent-Burgués. 1995, J. Crystal Growth, 154, 364.

De acordo com as políticas editoriais, estes artigos não podem ser depositados em repositório de acesso aberto. Para acesso aos artigos completos entre em contato com o(a) autor(a) ou com o Serviço de Biblioteca e Informação IFSC - USP (bib@ifsc.usp.br).

PROKOFIEV, V. V.; ANDREETA, J. P.; LIMA, C. J.; ANDREETA, M. R. B.; HERNANDES, A. C.; CARVALHO, J. F.; KAMSHILIN, A. A.; JAASKELAINEN, T. Growth of single- crystal photorefractive fibers of $\text{Bi}_{12}\text{SiO}_{20}$ and $\text{Bi}_{12}\text{TiO}_{20}$ by the laser-heated pedestal growth method. **Journal of Crystal Growth**, Amsterdam, v.137, p.528-34, 1994.

ANDREETA, M. R. B.; HERNANDES, A. C.; CUFFINI, S. L.; GUEVARA, J. A.; MASCARENHAS, Y. P. Laser heated pedestal growth of orthorhombic SrHfO_3 single crystal fiber. **Journal of Crystal Growth**, Amsterdam, v. 200, p. 621-624, 1999.

CAPÍTULO 5

SOLIDIFICAÇÃO DIRECIONAL PELA TÉCNICA DE BRIDGMAN

V. Solidificação direcional pela técnica de Bridgman

Nessa técnica, o material é contido num cadiño e a solidificação acontece, geralmente, através de sua translação relativa num gradiente de temperatura axial. A interface cristal/líquido avança através do gradiente de temperatura que então dissipa o calor latente de fusão.

A escolha do cadiño é de grande importância no processo, e algumas de suas características fundamentais para a realização de um experimento de crescimento são:

- I) o cadiño não deve contaminar o material;
- II) a contração diferencial entre cristal e cadiño durante o resfriamento pós-solidificação não deve tensionar o cristal. Portanto o coeficiente de expansão do cadiño deve ser menor do que o do cristal;
- III) é desejável que não haja aderência do cristal ao cadiño o que pode também introduzir tensões mecânicas no cristal;
- IV) é desejável que haja bom casamento entre as condutividades térmicas do cristal e cadiño para não existirem efeitos sobre a forma da interface sólido-líquido.

5.1 – Artigo: Tellurium-rich phase in n-type bismuth telluride crystals grown by the Bridgman technique

5.2 – Artigo: Growth and characterization of HgI_2 , PbI_2 and $PbI_2:HgI_2$ layered semiconductors

Bibliografia

- [1] MARIA CLÁUDIA CERCHIARI CUSTÓDIO - "Síntese e crescimento de materiais termoelétricos: Bi_2Te_3 e soluções sólidas de $(\text{Bi}_{(1-x)}\text{Sb}_x)_2\text{Te}_3$ ". Tese de doutoramento, IFUSP, São Paulo, 1997.
- [2] LUCIARA BENEDITA BARBOSA - "Preparação e propriedades elétricas e ópticas de cristais de PbI_2 ". Dissertação de mestrado, IFSC-USP, 1999.
- [3] ÉRIKA REGINA MANOEL - "Crescimento de cristais de HgI_2 , PbI_2 e $\text{PbI}_2\text{:HgI}_2$ para aplicações em detetores de radiação ionizante". Dissertação de mestrado, IFSC-USP, 1997.
- [4] JOSÉ PEDRO ANDREETA – Crescimento de cristais uma abordagem fenomenológica. Tese de Livre-Docência, Universidade de São Paulo, IFSC, 1997.
- [5] W.A. TILLER – The science of crystallization – Macroscopic phenomena and defect generation. Cambridge University Press, Cambridge, 1991.
- [6] FRANCISCO E.G. GUIMARÃES, ÉRIKA R. MANOEL, JOSÉ R. SABINO, ANTONIO C. HERNANDES - "Optical properties of tetragonal HgI_2 and PbI_2 : the relationship with crystalline quality". Brazilian Journal Physics, 27/A(4) : 340-344, 1997.
- [7] M.C.C. CUSTÓDIO, S.R. RABANI, A.C. HERNANDES, J.P. ANDREETA - "Homogeneidade dos parâmetros termoelétricos em cristais de Bi_2Te_3 crescidos pela técnica de Bridgman" - Pesq. Desenv. tecnol., 19 : 55 - 56, 1995.
- [8] BARBOSA, L B; CUSTODIO, M C C; HERNANDES, A C. Purificação e crescimento de cristais de PbI_2 . In: ENCONTRO DA SOCIEDADE BRASILEIRA DE CRESCIMENTO DE CRISTAIS, 3, São Carlos, 1998. Anais. São Carlos, IFSC, 1998. p.22-5.

De acordo com as políticas editoriais, este artigo não pode ser depositado em repositório de acesso aberto. Para acesso ao artigo completo entre em contato com o(a) autor(a) ou com o Serviço de Biblioteca e Informação IFSC - USP (bib@ifsc.usp.br)

CUSTÓDIO, M. C. C.; HERNANDES, A. C. Tellurium-rich phase in n-type bismuth telluride crystals grown by the Bridgman technique. *Journal of Crystal Growth*, Amsterdam, v.205, p.523-530, 1999.

Growth and Characterization of HgI_2 , PbI_2 and $\text{PbI}_2:\text{HgI}_2$ Layered Semiconductors

E.R. Manoel, M.C.C. Custódio, F.E.G. Guimarães,

*R.F. Bianchi, A.C. Hernandes**

Universidade de São Paulo, Instituto de Física de São Carlos,

C.P. 369, 13560-970 São Carlos - SP, Brazil

**e-mail: hernandes@ifsc.sc.usp.br*

Received: February 27, 1998; Revised: March 23, 1999

This paper presents a methodology for the preparation of $\alpha\text{-HgI}_2$ by Physical Vapor Transport and of PbI_2 crystals using the Bridgman technique. The results of the growth of HgI_2 diluted in PbI_2 by the Bridgman technique are shown for the first time, its limit of solubility having been determined at 600 ppm of HgI_2 in the PbI_2 matrix. Optical absorption, photoluminescence and electrical conductivity measurements show that the crystals prepared are of good crystalline quality.

Keywords: *mercuric iodide, lead iodide, crystal growth*

1. Introduction

Increasing interest has been focusing on the search for high-energy resolution room temperature X-ray detectors. The development of single detector spectrometers and, lately, of multidetector array systems has been driven by the specific needs of space exploration and synchrotron radiation applications. Recently, layered semiconductors materials have been found to possess a number of properties that make them quite attractive for such applications. Mercuric iodide (HgI_2) and lead iodide (PbI_2) crystals present an excellent response as X-ray and γ -ray detectors at room temperature. Their high density and high atomic number allow one to manufacture small, compact detectors with a very good volume-efficiency ratio¹⁻⁴. The major advantage in using an HgI_2 or PbI_2 system in many applications is that they do not require liquid nitrogen for cooling, as opposed to most commercially available systems, which are composed of cryogenically cooled silicon or germanium X-ray detectors.

Several studies have been carried out on the properties, preparation and application of the HgI_2 layered semiconductor compound and much progress has been made through improved purification of starting materials and growth techniques⁵⁻⁷. However, good PbI_2 crystals have only recently been prepared⁸. In this work, we present a methodology for the preparation of $\alpha\text{-HgI}_2$ by Physical Vapor Transport and for PbI_2 crystals using the Bridgman

technique. We also show, for the first time, the results of the growth of HgI_2 diluted in PbI_2 by the Bridgman technique. In this specific case, the solubility limit was determined and some electric, structural and optical properties were measured.

2. Experimental Procedure

2.1. Purification and crystal growth

$\alpha\text{-HgI}_2$

Successful growth of high optical and structural quality $\alpha\text{-HgI}_2$ single crystals is largely dependent on the purity of the materials used. Amorphous carbon and carbon complex compounds are present in mercuric iodide and it is necessary to purify the starting materials. All the purification experiments carried out used red HgI_2 from Fluka Chemika (99.5% pure) and from Aldrich Chemical Co. (99.999% pure). The repeated sublimation technique was employed due to the high vapor pressure of mercuric iodide (0.1 Torr at 120 °C). In this technique, the starting materials were placed inside a cylindrical glass ampoule specifically designed to repeat the sublimation cycles after the chemical and vacuum cleaning process. Approximately 15 g of red HgI_2 was used in each experiment. The ampoule was then sealed under high vacuum conditions, and a sublimation cycle was initiated in a homemade vertical furnace. An axial temperature gradient, typically of 20 °C/cm, was imposed to evaporate the mercuric iodide. Approximately

70 h were necessary to evaporate all the HgI_2 , which was then deposited in the cold extremity of the ampoule. In each cycle, the impurities (black from red HgI_2 Fluka and grayish from Aldrich) deposited at the hot extremity were eliminated by sealing off part of the glass ampoule. After each cycle, the amount of the impurities decreased drastically. Black and grayish impurities were associated to amorphous carbon and hydrocarbon, as suggested by Piechotka and Kaldis⁶.

After the purification process, the mercuric iodide was used as a source in crystal growth runs. Every growth experiments were performed by the Physical Vapor Transport (PVT) technique⁹, in a homemade equipment shown in Fig. 1A. This system consisted of a transparent resistive furnace equipped with an 808 Eurotherm temperature controller. Vacuum was used as thermal insulation and the typical temperature fluctuation was 0.5° Celsius. A cold finger was used as a heat exchanger with a temperature control better than ± 0.3 °C. The temperature profile of our crystal growth system (Fig. 1B) was measured using a Chromel-Alumel thermocouple when the furnace was empty, that is, without the ampoule. The ampoule with red mercuric iodide was placed in an area of the furnace where the temperature was approximately constant (Fig. 1B). A small area of the cold finger was put in contact with the growth ampoule in a predetermined position. The temperature gradient established in this area was responsible for the nucleation process. Seed selection was carried out by the trial and error procedure. The following growth of the red HgI_2 crystal was possible through a cooling temperature program applied to the cold finger. The optimal mass transport responsible for growth was achieved through maximization of the aspect ratio (height/ radius of ampoule). After some tests, we were able to grow good quality crystals of reasonable size (0.6 cm^3) and with a very well defined external morphology. Figure 2A shows one of the crystals obtained by this technique.

PbI_2 and $\text{PbI}_2:\text{HgI}_2$

Lead iodide is a more stable compound than mercuric iodide due to its lower vapor pressure and its stable crystalline structure up to its melting point. These two characteristics make it easier to prepare than red HgI_2 . In our experiments we used PbI_2 from Johnson Matthey Co. (99.999% metal pure) which was purified by recrystallization to avoid organic impurities.

A quartz ampoule (8 mm in internal diameter and 95 mm in length) was used in all the crystal growing runs. It was washed with detergent and distilled water, chemically cleaned in a HF and HNO_3 solution (1:1 in volume) for approximately 15 min and thermally treated at 800 °C under high vacuum conditions. After this step, the recrystallized PbI_2 was placed in the ampoule, sealed under high vacuum ($\sim 10^{-5}$ Torr) and put into the Bridgman furnace.

The Bridgman equipment had previously been built and thermally characterized¹⁰. The axial temperature gradient measured during crystal growth was 35 °C/cm. All the PbI_2 prepared in our system were yellowish and transparent and easily cleaved in the direction perpendicular to the c crystallographic axis. Bubbles appeared only on its external

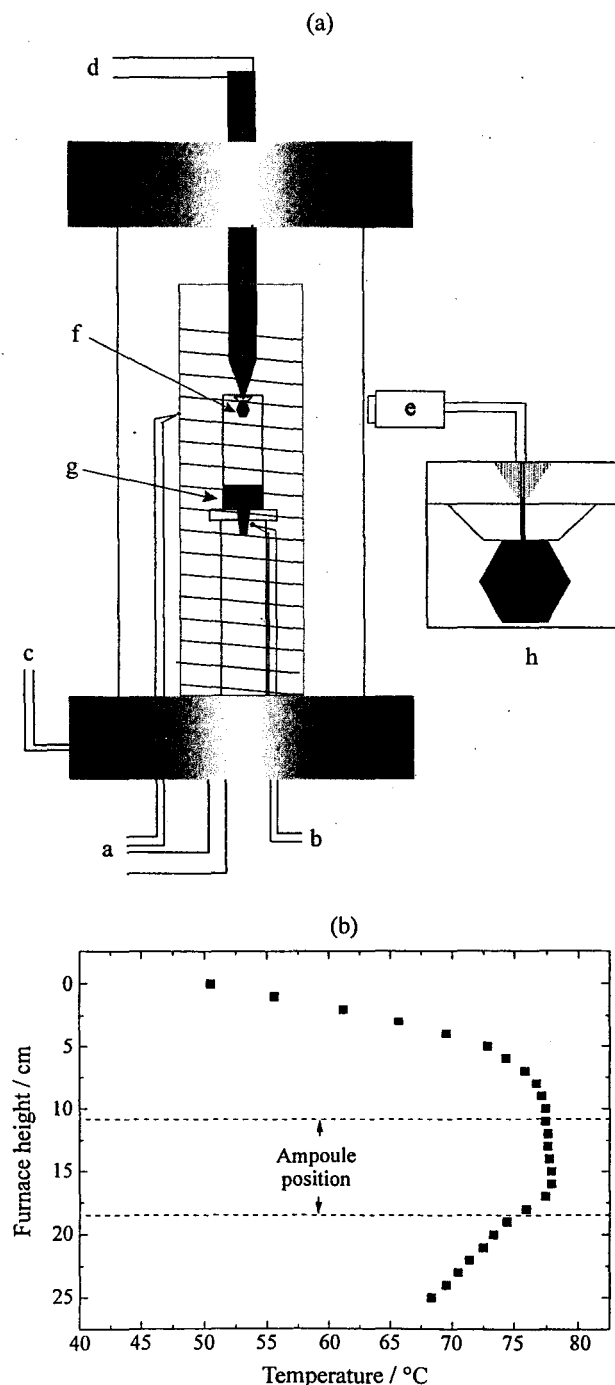


Figure 1. (A) Schematic drawing of the crystal growth furnace. a-temperature controller; b-source material temperature monitoring; c-vacuum system output; d-cold finger temperature controller; e-CCD video camera, f- HgI_2 single crystal, g-source material, h-video monitor. (B) Temperature profile of furnace without the ampoule inside.

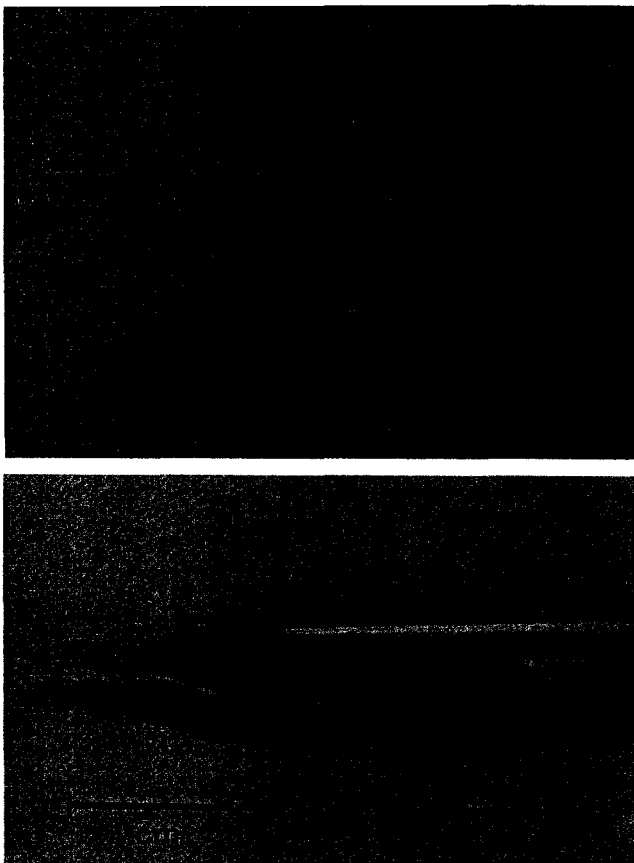


Figure 2. (A) Mercuric iodide single crystal grown by PVT method. (B) PbI_2 crystal grown by Bridgman technique.

surface and there was no adhesion to the quartz ampoule. This last characteristic is an indication of the absence of OH^- impurities in our experiments, as suggested by Eckstein *et al.*¹¹. Figure 2B shows a PbI_2 single crystal grown under the experimental conditions described above.

$\text{PbI}_2\text{:HgI}_2$ crystals were grown at five different nominal concentrations (50000 ppm, 5000 ppm, 1100 ppm, 680 ppm and 600 ppm) also following the experimental routine of the pure lead iodide. A segregated phase of mercuric iodide was observed in most of the experiments, and it was associated to the structural difference between PbI_2 (hexagonal structure) and HgI_2 (tetragonal structure). Indeed, a large amount of HgI_2 in the bulk and on the surface of the grown crystal was detected at a high nominal concentration. A small amount of segregated phase was detected in the experiment with 680 ppm of mercuric iodide. On the other hand, no segregated phase was detected with a nominal concentration of 600 ppm of red HgI_2 . These crystals were transparent and were reddish in color. It was assumed that 600 ppm of HgI_2 in the liquid phase is the solubility limit for PbI_2 crystals.

2.2. Characterization

Photoluminescence (PL) measurements were carried out using an Ar ion laser tuned to 458 nm. The samples

were fixed with teflon tape on a cooled copper finger of a closed-cycle helium cryostat to avoid any chemical reaction, and cooled to a temperature of about 15 K. The PL radiation was dispersed in a 0.5 m monochromator with 0.01 nm resolution and detected by a photomultiplier tube using conventional lock-in detection. All the experiments were carried out under very low excitation intensities to avoid thermal heating of the sample and identical optical paths.

The optical band gap of the crystals was determined by absorption measurements, in the visible spectral range, at room temperature (300 K), using Cary 17 equipment.

The DC conductivity measurements were made of all grown crystals at room temperature using a voltage source and an electrometer to detect the current. The electrical contacts were made by pressing the sample between brass plates.

3. Results and Discussion

The low temperature PL spectra of HgI_2 samples grown after three different purification procedures are shown in Fig. 3. In (a), a seed was obtained after one cycle of purification, in (b) a grain of a polycrystalline material was obtained from two purification cycles, and in (c) a single crystal was obtained from three purification cycles. The last two samples were grown by the PVT method. The results

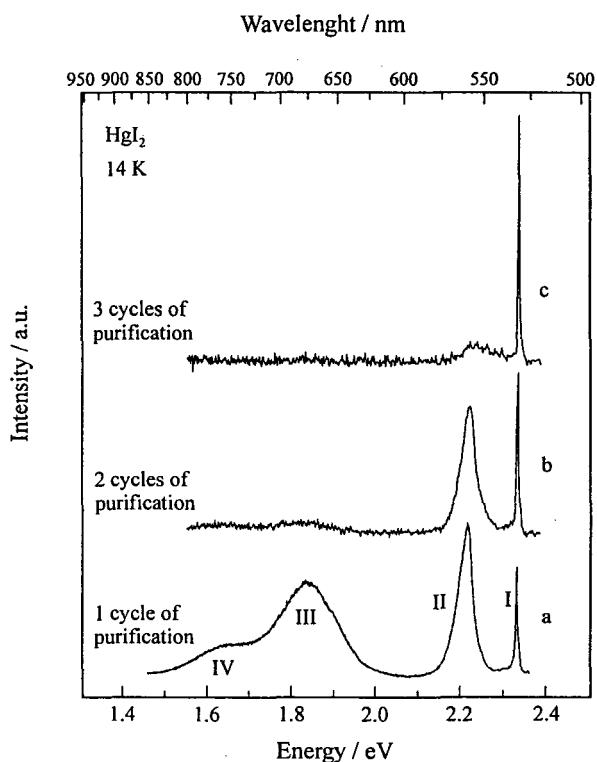


Figure 3. Photoluminescence spectra of $\alpha\text{-HgI}_2$ samples grown after three different purification procedures. Measurements were carried out perpendicularly to the (001) crystallographic plane.

show the effect of purification on crystalline quality. Four bands were observed in the single purification cycle. The broad III and IV bands located at 1.844 eV and 1.646 eV, respectively, are associated to impurities. Band IV and three other bands have already been analyzed by Merz *et al.*¹². A comparison of their spectra shows that our single cycle purification spectrum is very similar, with a coincidence of bands I, (2.335 eV) II (2.216 eV) and IV (1.640 eV). Merz *et al.* also labeled a broad band, present only in raw material and located at 2.000 eV, as B3. This band disappeared after the first purification cycle, and was also absent in our spectra. The major difference in our spectra is the presence of the band located at 1.844 eV. We attributed this band to copper, as a result of an accidental contact of the sample to the copper of the cold finger, although teflon tape was used for isolation. This attribution was based on the study performed by Bao *et al.*¹³, who first attributed this band to copper. They studied the photoluminescence spectra taken from the same spot on an HgI₂ crystal obtained before and after a semitransparent Cu layer was deposited, where a broad band centered at 672.0 nm (1.844 eV) appeared after the deposition.

A comparison of the (a), (b), and (c) spectra (Fig. 3) shows that the sample with two purification cycles does not present the broad band that is further away from the band edge. Moreover, the band II to band I ratio decreased. There was a further decrease in band II to band I ratio with three purification cycles, and the intensity of band II was also considerably lower. The band II to band I ratio and the absolute intensity of band II were associated to changes in stoichiometry by Merz *et al.*¹² and Schieber *et al.*¹⁴. They demonstrated that both factors increased in successive sublimation runs, when each run was performed under dynamic vacuum conditions, which might reduce the iodine concentration by preferential removal of the more volatile species. Thus, our results show that the triple purification cycle sample has no impurity bands and is not iodine deficient, as a result of carrying out the sublimation processes in closed tubes. Another feature of these spectra is that band I is, in fact, the predominant line of a great set of lines in the region near the band edge. This region was studied by several authors^{15,16}, and Bao *et al.*, in 1990¹⁷, identified 26 emission lines from 2.343 eV (529.0 nm) to 2.295 eV (540.0 nm), the predominant line, located at 2.335 eV, being due to zero-phonon line emission of polariton A¹⁵, and other extremely near lines, which are not resolved in our spectrum, are due to bound excitons.

Figure 4 illustrates the PL emissions near the band edge for PbI₂:HgI₂ samples containing nominally 600 ppm, 5000 ppm and 50000 ppm of HgI₂ in the source materials. The same figure also shows a spectrum of pure PbI₂, for comparison. It should be pointed out that although doped PbI₂ samples are more reddish than the pure ones, the PL spectra do not present any detectable red shift. In the 2H polytype

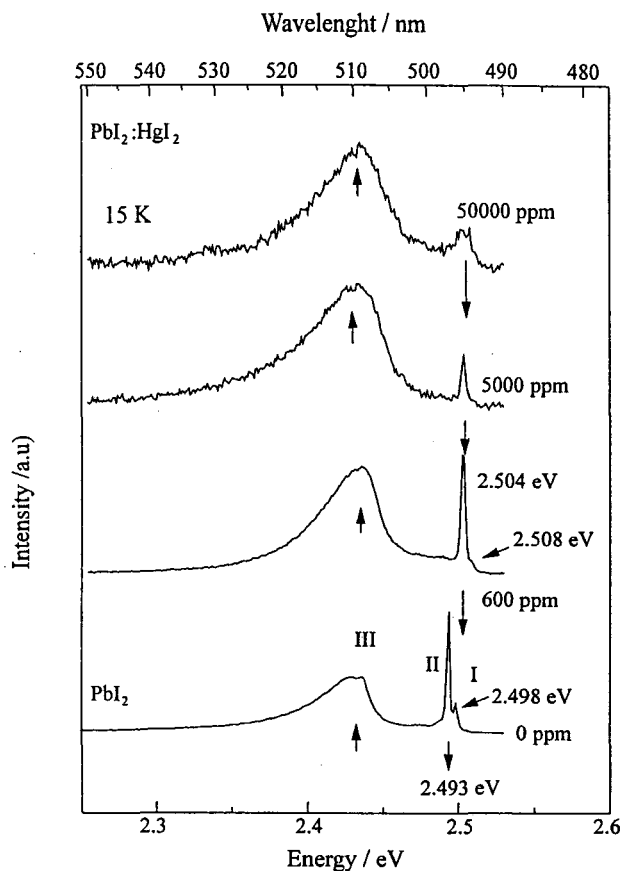


Figure 4. PL emissions near the band edge for PbI₂ and PbI₂:HgI₂ samples.

of PbI₂, the strongest sharp emission line is located at 2.493 eV, corresponding to a bound exciton recombination, an attribution given by Gähwiller and Harbecke¹⁸, and is seen in the pure PbI₂ spectrum. Another thing that can be seen in the same spectrum is the small emission line due to a free exciton recombination, located at 2.498 eV. In the spectrum with 600 ppm of HgI₂ as well as in the other doped PbI₂ spectra, the intense line of bound exciton is shifted to higher energies located at 2.504 eV, which is characteristic of the 4H polytype¹⁹. The free exciton line still can be seen, with a much lower intensity, almost as a shoulder of bound exciton peak, located at 2.508 eV, in the 600 ppm doped PbI₂ spectrum. At higher doping concentrations this line is completely destroyed, there is a steady broadening of the emission and reduction of bound exciton line intensity, indicating the deterioration of crystal quality. The pure PbI₂ was only 2H polytype, as demonstrated in a resolved spectrum published elsewhere²⁰, because it does not have the structures of a sample with more than one polytype, as shown by Levy *et al.*¹⁹. Hence, the transition of the 2H to the 4H polytype was caused by the introduction of the mercuric iodide in the lead iodide lattice. The broad band located at 2.429 eV in pure PbI₂ is associated to a defect

level recombination¹⁹ and this band shifts to 2.438 eV in doped samples.

The results of electrical conductivity obtained for α - HgI_2 and PbI_2 samples were $1 \times 10^{-13} \Omega^{-1} \text{cm}^{-1}$ and $3 \times 10^{-12} \Omega^{-1} \text{cm}^{-1}$, respectively, coinciding with the best values found in the literature²¹. The electrical conductivities at room temperature in the diluted crystals presented a dispersion of three orders of magnitude (10^{-14} to $10^{-11} \Omega^{-1} \text{cm}^{-1}$), and the sample containing 600 ppm of HgI_2 was the most resistive one, with electrical conductivity of $5 \times 10^{-14} \Omega^{-1} \text{cm}^{-1}$, the smallest obtained value for this group of materials. The optical band gap energies determined were 2.10 eV to α - HgI_2 and 2.28 eV to pure PbI_2 . These results are very close to the previously published values¹³. The values obtained for the HgI_2 diluted in PbI_2 crystals do not present any difference in comparison to the pure crystal.

5. Conclusions

α - HgI_2 , PbI_2 and diluted doped PbI_2 samples were grown, the first by Physical Vapor Transport and the second and third by the Bridgman method. The characterization techniques employed showed that the crystals are of good quality. The PL results from the mercuric iodide samples showed that, after 3 purification cycles, the exciton emission line is sharp and with a high intensity. Moreover, no impurity band was observed and the material was not iodine deficient. Analysis of the PL spectra of doped PbI_2 samples indicated that the introduction of mercuric iodide in lead iodide lattice changed the polytype from 2H to 4H and destroyed the structural quality. It was, nonetheless, possible to determine the solubility limit at 600 ppm of HgI_2 , the free exciton line for this sample was still seen in the spectrum and the sample presented the lowest DC conductivity ($5 \times 10^{-14} \Omega^{-1} \text{cm}^{-1}$) of this type of material. All the samples measured were very resistive, with values of $10^{-13} \Omega^{-1} \text{cm}^{-1}$ of mercuric iodide and $3 \times 10^{-12} \Omega^{-1} \text{cm}^{-1}$ of lead iodide, which coincide with the best values reported in the literature. Furthermore, the values obtained for the optical band gap at room temperature are in good agreement with the ones reported previously.

Acknowledgments

The authors wish to express their appreciation for the financial support provided by the Brazilian agencies FAPESP, CNPq, CAPES and FINEP.

References

- Iwanczyk, J.S.; Wang, Y.J.; Bradley, J.G.; Conley, J.M.; Albee, A.L.; Economou; T.E. *IEEE Trans. on Nuclear Sci.*, v. 36, n. 1, p. 841-845, 1989.
- Olmos, P.; Perez, J.M.; Diegues, E.; Serrano, M.D. *J. Phys. D: Appl. Phys.*, v. 27, p. 2251-2257, 1994.
- Eckstein, J.; Erler, B.; Eiche, C.; Benz, K.W. *J. Cryst. Growth*, v. 131, p. 453-456, 1993.
- Li, Z.; Li, W.; Liu, J.; Zhao, B.; Zhu, S.; Xu, H.; Yuan, H. *J. Cryst. Growth*, v. 156, p. 86-90, 1995.
- Manoel, E.R. *Dissertação de Mestrado*, IFSC, USP, 1997.
- Piechotka, M.; Kaldis, E. *Final Report ESA Contract*, Zurich, Switzerland, 1991.
- Piechotka, M.; Kaldis, E. *Nuclear Instr. and Methods in Phys. Research*, v. A322, p. 387, 1992.
- Chaudhary, S.K.; Trigunayat *J. Cryst. Growth*, v. 62, p. 398-400, 1983.
- van den Berg, L.; Schnepple, W.F. *Nuclear Instr. and Methods in Phys. Research*, v. A283, p. 335-338, 1989.
- Custódio, M.C.C. *Tese de Doutoramento*, IF, USP, 1997.
- Eckstein, J.; Erler, B.; Benz, K.W. *Mat. Res. Bull.*, v. 27, p. 533-544, 1992.
- Merz, J.L.; Wu, Z.L.; van den Berg, L.; Scheneppele, W.F. *Nucl. Inst. Meth.*, v. 213, p. 51, 1983.
- Bao, X.J.; Schlesinger, T.E.; James, R.B.; Stulen, R.H.; Ortale, C.; van den Berg, L. *J. Appl. Phys.*, v. 67, n. 12, 1990.
- Schieber, M.; Roth, M.; Scheneppele, W.F. *J. Cryst. Growth*, v. 65, p. 353-364, 1983.
- Goto, T.; Nishina, Y. *Solid State Commun.*, v. 25, p. 123-125, 1978.
- Novikov, B.V.; Pimonenko, M.M. *Sov. Phys. Semic.*, v. 4, p. 1785, 1971.
- Bao, X.J.; Schlesinger, T.E.; James, R.B.; Ortale, C.; van den Berg, L. *J. Appl. Phys.*, v. 68, n. 6, 1990.
- Gähwiller, C.H.; Harbecke, G. *Phys. Rev.*, v. 185, p. 1141, 1969.
- Lévy, F.; Mercier, A.; Voitchovsky, J.P. *Solid State Commun.*, v. 15, p. 819-822, 1974.
- Guimarães, F.E.G.; Manoel, E.R.; Sabino, J.R.; Hernandes, A.C., *Braz. J. Phys.*, v. 27/A, n. 4, 1997.
- Minder, R.; Ottaviani, G.; Canali, C. *J. Phys. Chem. Solids*, v. 37, p. 417-423, 1976.

CAPÍTULO 6

CRESCIMENTO DE CRISTAIS

A PARTIR DE SOLUÇÃO

VI. Crescimento de cristais a partir de solução

O processo de crescimento de cristais a partir de uma solução envolve simultaneamente o transporte de massa e calor entre a superfície do cristal e a solução circunvizinha. Experimentalmente, os métodos de crescimento de cristal a partir de solução são baseados na dependência da solubilidade de uma substância com os parâmetros termodinâmicos do processo: temperatura, pressão e concentração do solvente. A dependência da solubilidade com a temperatura é, na maioria dos casos, mais utilizada, devido a maior facilidade de controle dessa variável.

6.1 – Artigo: LAP single crystals growth free of micro-organisms by accurately controlled solvent evaporation technique.

6.2 – Artigo: Control of the concentration gradient during crystal growth from solution.

6.3 – Artigo: Preparação de monocristais de TGS por solução aquosa.

6.4 – Artigo: Growth and homogeneity fo Cr^{+3} doped GdAlO_3 single crystals.

Bibliografia

- [1] ANTONIO CARLOS HERNANDES – “Estudo in situ do perfil de concentração do soluto durante o processo de crescimento e dissolução de monocrystal de α -HgI₂”. Tese de doutoramento, IFQSC, USP, 1993.
- [2] ANTONIO CARLOS HERNANDES – “Crescimento, caracterização e aplicação de monocrystalis de TGS em detetores de radiação na região do infravermelho”. Dissertação de mestrado, IFQSC, USP, 1988.
- [3] LIANA BUENO OLIVEIRA AMORIM DE MORAES - “Crescimento de cristais orgânicos e a avaliação de suas qualidades para aplicações em óptica não-linear”. Dissertação de mestrado, IFSC, USP, 1998.
- [4] LEMOS, V.; CAMARGO, F.; HERNANDES, A.C.; FREIRE, P.T.C. - "Structural phase transition in RbLiSO₄". Journal of Raman Spectroscopy, 24, 133-137, 1993.
- [5] BEDARIDA, F.; DALL'AGLIO, G.A.; GATTI, L.; HERNANDES, A.C.; PIANO, E.; PONTIGGIA, C.; SOLITRO, F. - "MHOI & DIFFRASOR: Two optical methods for microgravity crystal growth". Proc. 4th International Symposium on Experimental Methods for Microgravity Materials Science Research, San Diego, California, USA - p. 27-32, março, 1992.
- [6] ANDREETA, J.P.; HERNANDES, A.C.; GALLO, N.J.H. - "Growth and homogeneity of Cr⁺³ doped GdAlO₃ single crystals". Mat. Res. Bull., 25 (1) : 51-56, 1990.
- [7] PEREIRA, R.F.R.; AMORIN, H.S.; AMARAL JR., M.R.; HERNANDES, A.C.; GALLO, N.J.H.; ANDREETA, J.P. - "Superconducting BiSrCaCuO system and organic reaction". J. Mat. Science Letters, 9 (8) : 901-903, 1990.
- [8] ANDREETA, J.P.; HERNANDES, A.C. ; GALLO, N.J.H. - "Segregation effects in GdAlO₃ : Cr⁺³ growth by HTS and CZ". Mat. Res. Bull., 24 (1): 83-6, 1989.

De acordo com as políticas editoriais, este artigo não pode ser depositado em repositório de acesso aberto. Para acesso ao artigo completo entre em contato com o(a) autor(a) ou com o Serviço de Biblioteca e Informação IFSC - USP (bib@ifsc.usp.br)

CARVALHO, J. F.; HERNANDES, A. C.; NUNES, F. D.; MORAES, L. B. O. A.; MISOGUTI, L.; ZÍLIO, S. C. LAP single crystal growth free of microorganisms by an accurately controlled solvent evaporation technique. **Journal of Crystal Growth**, Amsterdam, v. 173, p. 487-491, 1997.

CONTROL OF THE CONCENTRATION GRADIENT DURING CRYSTAL GROWTH FROM SOLUTION

F. BEDARIDA¹, G.A. DALL'AGLIO¹, A.C. HERNANDES², E. PIANO³, C. PONTIGGIA³¹ DISTER, Università di Genova, Corso Europa 26, 16132 Genova, Italy² Inst. de Fisica e Quimica de São Carlos, Universidade de São Paulo, Brasil³ Dipartimento di Fisica, Università di Genova, Genova, Italy

ABSTRACT

The growth of a HgI_2 crystal from solution is studied in coherent light with a new optical schema. A laser beam crosses the solution where the crystal is growing. The beam is there diffracted by a slit 25 μ wide and the diffraction pattern is analyzed. It moves according to the gradient of the concentration. By analyzing the pattern movements one can get informations on the phenomena occurring inside the solution. A neat discontinuity in the concentration plot is always present at some distance from the growing crystal surface. This is the signal of an "anomaly" in the concentration behaviour. This method can be used to study crystal growth in microgravity.

Keywords : diffraction, concentration gradients, solution growth, mercuric iodide

1. SCIENTIFIC OBJECTIVES

The properties of a solid which result from its structure can be largely modified by the presence of crystallo-graphic and chemical defects. How these defects appear and develop depends on mass and heat transport conditions on and near a crystal-nutrient interface during crystal-lization. Hence, both the growth of high quality crystals and the preparation of samples with particular predetermined extrinsic properties require a complete understanding of the mechanisms ruling crystallization from vapor, solution and melt.

2. HOW THE DIFFRASOR WORKS

Diffrasor has already been presented in some other papers (Refs. 1, 2); a He-Ne 5 mW laser beam crosses first a vessel containing the solution and the crystal to be studied, then a horizontal slit (10 or 25 microns wide), is placed in the first focal plane of a lens, which generates a light diffraction pattern. In the second focal plane, a photodiode, able to shift up and down under a micromanipulator control, receives the light diffracted by the slit and gives an electric current proportional to it. The signal is elaborated by a PC.

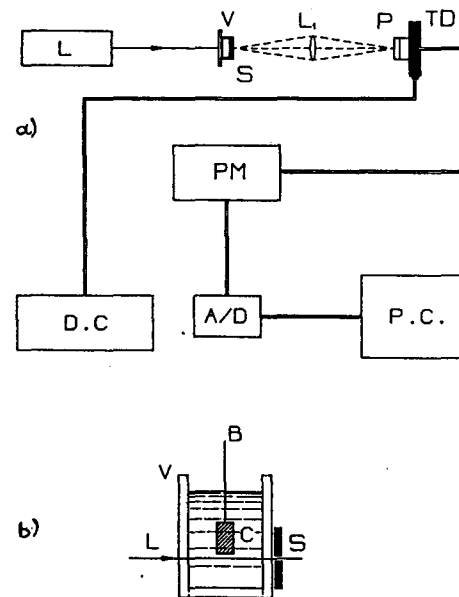


Figure 1: (a) Block diagram of the apparatus: L laser, V vessel, S slit, L₁ lens, P photodiode, TD translating device, DC drive controller, PM photometer, A/D amplificator, PC personal computer; (b) Vessel solution: V glass vessel, C crystal, L laser beam, B rod for the crystal, S slit

This technique relies on a simple physical process: the laser light which has crossed the vessel with the solution, or the vapour, is diffracted by the slit and the photodiode can record the intensity and the profile of the diffraction pattern, also setting the minima and the maxima positions. During crystal growth from solution, or vapour, thermal and concentrational gradients are formed and convective movements inside the solution take place; all of these ones shift the laser beam and modify shape, position and intensity of the diffraction pattern. From measuring these movements one can check the concentration field. With an accurate thermostatation, thermal disturbances are cut out, and hydrodynamics phenomena due to diffusion and convection are better observable.

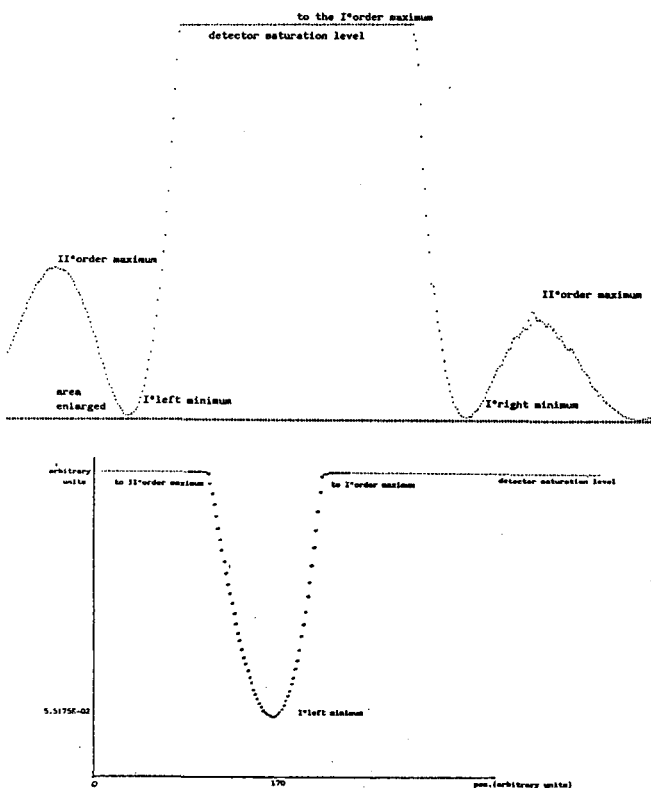


Figure 2: (a) Diffraction pattern profile; crystal growth affects its shape and displaces it; (b) diffraction pattern enlarged area around the first left minimum. Position and intensity changes as growth goes by.

The diffrasor at the moment has allowed us to take measures from the bulk up to 10 microns over the crystal surface, is sensitive to concentration gradients of the order of 10^{-3} , and can be used to investigate a zone very near to the surface not well known yet but of great importance for growth physics.

Data collected by measurements are immediately elaborated to perform a first real time analysis of the phenomena occurring inside the solution; then are obviously memorized to be re-read when the experiment is over.

3. EXPERIMENTS

The attention was devoted to mercuric iodide solution growth, because of its great importance in the present crystallographic research (Refs.3-5), and some interesting results came out.

During measurements a crystal was grown and dissolved at different temperatures and supersaturations; crystal size was about $1.5 \times 2.5 \times 3.0$ mm; it grew in a solution of DMSO (dimethyl sulfoxide) and methanol (MeOH) (Ref.6); the DMSO mole fraction was 0.8. In order to minimize the influence of the cell geometry the investigated crystal was kept in the same fixed position during the whole experimental period of time; it can be said that convection in the solution was strongly dependent by the crystal

position inside the cell and by the shape of the cell itself. First runs were performed with plain solution and no crystal inside; as foreseen they always gave "zero results": diffraction pattern never changed its position, within the experimental error.

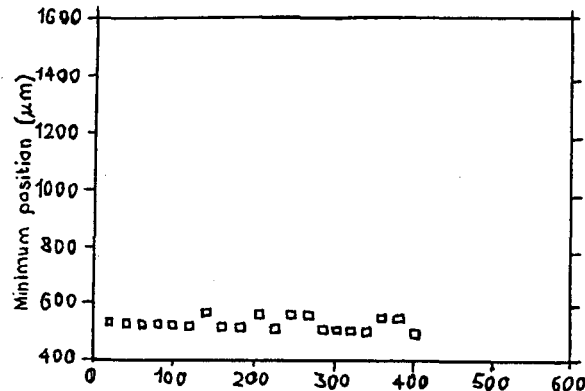


Figure 3: Position of diffraction pattern first left minimum with no crystal inside the solution.
Temperature $T = 29.45 \pm 0.02^\circ\text{C}$

Observations made in presence of the crystal gave typical results; according to them the concentration behaviour versus distance from the crystal fits the theoretical calculations (Ref.7) in first approximation but with a peculiarity: during growth, at different temperatures and supersaturations, there is an inversion zone in the concentration gradient trend, always present at more or less 50 microns above the crystal growing face. This fact could hint the presence of a boundary layer in that area; further studies are needed about this subject, anyway.

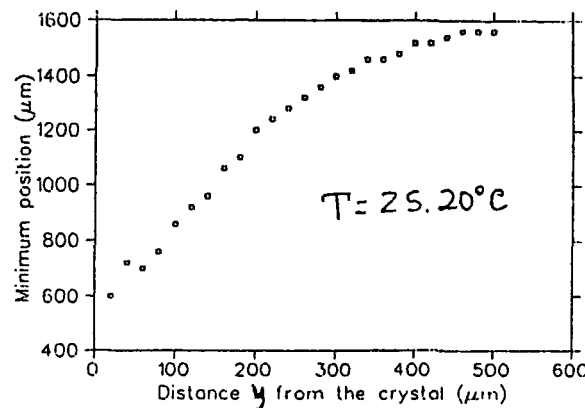


Figure 4: Position of diffraction pattern minimum vs distance from the crystal.
Temperature $T = 25.20 \pm 0.02^\circ\text{C}$
Equilibrium temperature $\approx 30^\circ\text{C}$
Crystal growth rate $\approx 1\mu\text{m}/\text{h}$
Measurement time ≈ 36 min
Inversion zone between 50 and 70 μm

4. DATA ANALYSIS

Given :

$\theta(y)$ = deflection angle
 L = vessel lenght
 f = lens focal lenght
 y = distance from the crystal
 n = refraction index;
 c = concentration of the solution
 $\Delta x''$ = difference in diffraction pattern displacement (given by)

$\Delta x''(y) = x''(\infty) - x''(y)$ where $x''(\infty)$ is the position inside the solution where the displacement is constant. In the case under study the maximum value of the displacement is set in the region where it is constant

we have :

$$\theta(y) = L * (dn/dy) \quad (1)$$

and, using approximation that θ is very small (paraxial rays)

$$\Delta x'' = f * \theta(y) \quad (2)$$

putting :

$$\frac{dc}{dy} = \frac{(dn/dy)}{(dn/dc)} \quad (3)$$

the concentration gradient dc/dy along the direction normal to the face of the crystal is linked to the measurement $\Delta x''$ of the displacement of the diffraction pattern first minimum by :

$$\Delta x'' = (\theta/L) * (dc/dy) = \frac{\Delta x''}{L f * (dn/dc)} \quad (4)$$

$$\text{with } L f * (dn/dc) = \text{cost} = 1/a \quad (5)$$

$$\text{therefore: } \frac{dc}{dy} = a \Delta x'' \quad (6)$$

$$c(y) = c(\infty) - \int_y^{\infty} (dc/dy) dy \quad (7)$$

with $c(\infty)$ = bulk concentration

In the mercuric iodide case, knowing L , f , dn/dc and $x''(\infty)$ one can calculate dc/dy as a function of y .

Experiment 1 :

$$L = 2500 \mu\text{m} \quad f = 6 \cdot 10^4 \mu\text{m}$$

and

$$n(c) = 1.45934 + 6.775 \cdot 10^{-2} c$$

$$c(\infty) = 2.5450 \text{ g/ml}$$

$$\text{at } 25^\circ\text{C (constant) and } \lambda = 632.8 \text{ nm}$$

where c is the mercuric iodide solution concentration.

Then :

$$\frac{dc}{dy} = 9.84 \cdot 10^{-6} \Delta x''(y) \quad (8)$$

Putting this value in Eq. 7 one can obtain the concentration values at different distances from the crystal face.

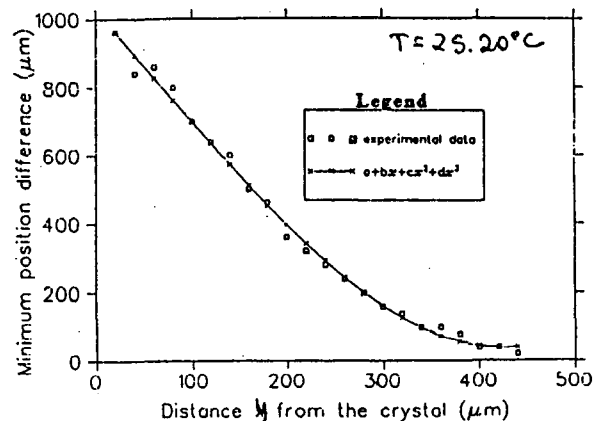


Figure 5: Concentration gradient (linearly dependent by displacement of diffraction pattern minimum) vs distance from the crystal : experimental data & best-fit 4th-order polynomial function.

Polynomial coefficients:

$$a = 1025.21 \quad b = -3.239$$

$$c = -1.0485 \cdot 10^{-3} \quad d = 7.55 \cdot 10^{-6}$$

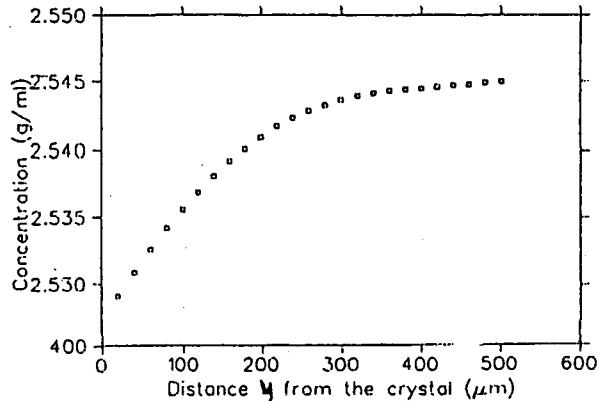


Figure 6: Concentration vs distance from the crystal according to the 4-th order polynomial best-fit.

Bulk concentration $c(\infty) = 2.5450 \text{ g/ml}$

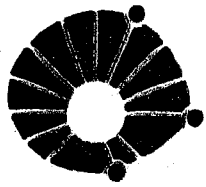
This is a first approximation; by means of a fitting program with polynomial functions good to minimize the standard deviation, the best fit for the set of points is given by a 4th-order polynomial; anyway, some exponential function is supposed to fit the experimental points probably better. Besides, with this polynomial the information about the inversion zone gets lost. The work is in progress.

5. CONCLUSIONS

As far as the state of the art at the moment, this instrument is quite sensitive to hydrodynamics phenomena, can perform measures quite near to the crystal surface and is rather easy to use. It must not be forgotten that diffrasor technique is a completion of multidirectional holographic interferometry because MHOI gives a tomography map of the concentration field along a plane parallel to the crystal face, while diffrasor scans

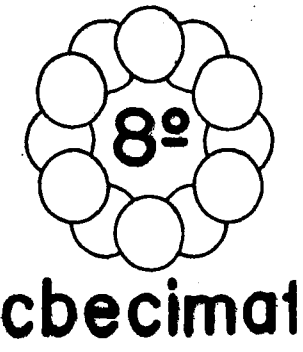
REFERENCES

1. Bedarida F & al 1990, Measurements of concentration profile by diffraction techniques, Journal of Crystal Growth, 106, 217-220.
2. Bedarida F & al 1990, Measurements of concentration profile by diffraction techniques, Proc Annual ELGRA Meeting, Utrecht, The Netherlands, ELGRA News 12, 31.
3. Piechotka M and Kaldis E 1986, Study of Technical Requirements for Vapor Growth Experiments in Microgravity Environment, Final Report, ESA Contract no.5943/84/F/FL, ETH Zürich 240 p.
4. Piechotka M and Kaldis E 1989, Mercuric iodide materials research: some recent developments and open problems, Nuclear Instruments and Methods in Physics Research A283, 111-118.
5. Pietchotka M and Kaldis E 1990, Large single crystals of mercuric iodide from the vapour phase; preparation of a space experiment, Journal of Crystal Growth, 99, 1300-1303.
6. Nicolau I and Joly J F 1980, Journal of Crystal Growth, 48, 61-73.
7. Rosemberger F 1979, Fundamentals of Crystal Growth I, Springer-Verlag, Berlin, 530 p.



PREPARAÇÃO DE MONOCRISTAIS DE TGS POR SOLUÇÃO AQUOSA

UNICAMP

A.C. HERNANDES, J.P. ANDREETA, N.J.H. GALLO
Instituto de Física e Química de São Carlos - USPSUMÁRIO

O método de crescimento de cristal por solução aquosa foi utilizado na preparação de monocrristais de Sulfato de Triglicina de alta qualidade óptica e estrutural. O equipamento usado na obtenção dos cristais permite o decaimento linear na temperatura da solução da ordem de $0,1^{\circ}\text{C}/\text{dia}$. Resultados preliminares obtidos com um protótipo de detetor de radiação infravermelha, desenvolvido com este material, apresentou uma responsividade em voltagem a 15 Hz de 7 V/W e um tempo de resposta de 1mseg.

INTRODUÇÃO

Diversos materiais que possuem grandes interesses científicos e tecnológicos, não podem ser obtidos em suas formas monocristalinas a partir de sua fase líquida (fusão). Isto ocorre, entre outros fatores, porque estes materiais sofrem decomposição térmica antes da temperatura de fusão ou sofrem transições de fases estruturais entre as temperaturas de crescimento e a ambiente. Entretanto, estes materiais podem ser preparados a partir de soluções a temperaturas baixas (0°C a 100°C). Os cristais crescidos por solução devido a lenta velocidade de crescimento, apresentam alta perfeição estrutural e desenvolvem faces planas que facilitam a orientação cristalográfica, condições estas de alta relevância para aplicações ópticas e detectores.

Basicamente, o método de crescimento consiste em efetuar uma separação de fase controlada em uma solução mantida neste estado metaestável, geralmente através da evaporação do solvente ou do abaixamento lento da temperatura. Devido a grande dificuldade em se controlar experimentalmente, a taxa de evaporação do solvente, o método de abaixamento de temperatura torna-se o mais vantajoso para a maioria dos experimentos.

Monocrristais de Sulfato de Triglicina (TGS), $[(\text{NH}_2\text{CH}_2\text{COOH})_3 \cdot \text{H}_2\text{SO}_4]$, apresentam propriedades piroelétricas e ferroelétricas e são de interesse devido as suas aplicações em detectores de radiação infravermelha e em dispositivos de imagem térmica [1, 2]. Como um material piroelétrico à temperaturas inferiores a 490°C , temperatura de transição ferro-paraelétrica, o TGS possui um eixo polar ao longo da direção cristalográfica $\langle 010 \rangle$. Na transição ocorre uma transformação do grupo espacial de P_2 , para P_{21}/m [3]. Os parâmetros de rede a temperatura ambiente são: $a = 9,41 \text{ \AA}$; $b = 12,64 \text{ \AA}$; $c = 5,73 \text{ \AA}$ e $\beta = 110,3^{\circ}$ [4]. Além disto, possui um plano de clivagem natural perpendicular ao eixo polar b .

Resultados dos experimentos de preparação dos monocrristais de TGS e de propriedades elétricas serão apresentados juntamente com algumas características de um protótipo de detetor de radiação infravermelha.

EXPERIMENTAL

O equipamento utilizado para o crescimento

rar em um intervalo de temperatura de 25°C a 80°C , com flutuações térmicas menores que $0,05^{\circ}\text{C}$. A função dos sistemas de rotação usados na solução e no banho térmico estão relacionados com o controle da hidrodinâmica nos processos de crescimento e com a homogeneidade conveniente da temperatura. O sistema móvel de contacto (figura 1-S) proporciona um decréscimo constante e linear na temperatura de $0,1^{\circ}\text{C}/\text{dia}$. Este decréscimo causa um fluxo de massa constante da fase líquida para a fase sólida, não levando em consideração o aumento da área de adsorção do cristal durante o processo, o que leva a um crescimento inicial instável.

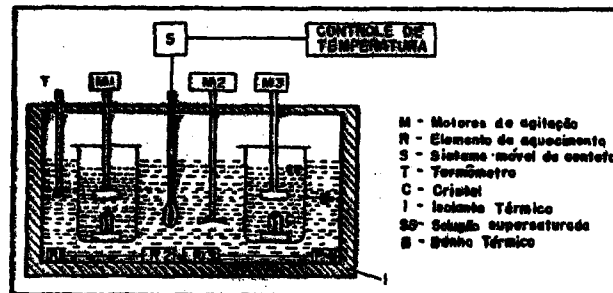
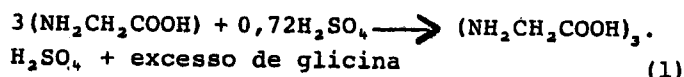


Figura 1: Representação esquemática do equipamento de crescimento de cristais por solução aquosa

Os métodos de crescimento de cristais por solução, na maioria dos casos, são baseados na dependência da solubilidade da substância com a temperatura e para o TGS é mostrado na figura 2. Com estas informações preparamos soluções saturadas, não estequiométricas, utilizando reagentes de grau P.A., baseando-se na reação de síntese:



O desvio da estequiometria faz-se necessário para garantir a obtenção de somente cristais de TGS, pois na proporção estequiométrica, em alguns casos, ocorre precipitação simultânea de duas fases sólidas constituídas de TGS e DGS (Sulfato de Diglicina). O Sulfato de Diglicina

semente do cristal introduzida na solução.

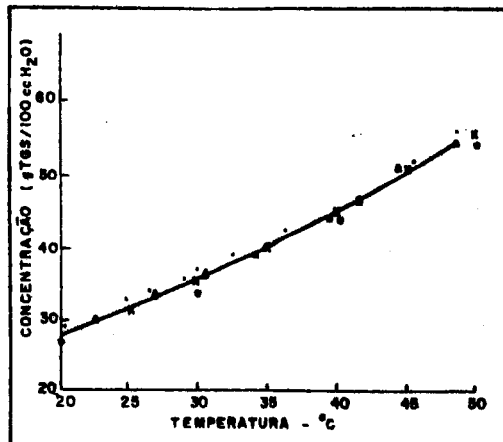


Figura 2: Curva de solubilidade para solução de TGS

RESULTADOS E DISCUSSÕES

Os monocrystalis de TGS obtidos apresentam uma alta qualidade óptica e estrutural. A figura 3 mostra o hábito de um dos cristais obtidos. Os resultados dos melhores experimentos são apresentados na tabela 1, sendo que a velocidade média de crescimento é definida como a taxa de incremento de massa por hora. Para a direção <110> a velocidade linear média obtida foi de $4,0 \times 10^{-7}$ cm/s, para uma supersaturação relativa correspondente a do experimento SA87-01. Análise química quantitativa realizada por Espectroscopia de Absorção Atômica nos monocrystalis, mostrou a presença de traços de impurezas de Na^{+1} e Ca^{+2} provenientes, provavelmente, da matéria-prima. A perfeição estrutural foi verificada por topografia de raios-x de transmissão, utilizando a técnica de Lang.

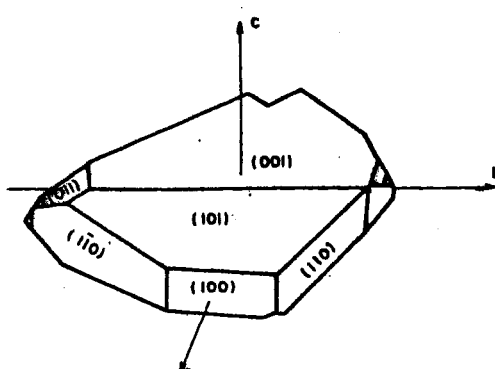


Figura 3: Hábito do monocrystal obtido no experimento nº SA87-01

Tabela 1: Resultados e condições experimentais utilizadas na preparação dos monocrystalis de TGS

Experimento	Temperatura Inicial de Crescimento (°C)	Concentração Inicial (g/ml)	Supersaturação Relativa Média	Massa do Cristal Obtido (g)	Velocidade de Crescimento Média (g/h)
SA87-01	45,0	0,5140	$2,75 \times 10^{-4}$	24,606	$2,6 \times 10^{-2}$
SA87-08	42,0	0,4800	$9,58 \times 10^{-2}$	8,122	$2,2 \times 10^{-2}$
SC87-05	36,1	0,4200	$8,8 \times 10^{-2}$	12,724	$3,5 \times 10^{-2}$

Para as medidas piroelétricas, amostras clivadas de 0,104 cm de espessura foram usadas. Eletrodos de prata de $0,049 \text{ cm}^2$ foram aplicados sobre a superfície (010) da amostra. Um campo elétrico da ordem de 10 kV/cm foi necessário por 30 minutos na temperatura de 308 K, para polarizar o cristal. Após este período, o sistema de aquecimento é desligado e realiza-se um rápido

aquecimento linear de 0,052 K/sec, gerada para um aquecimento linear de 0,052 K/sec, é mostrada na figura 4.

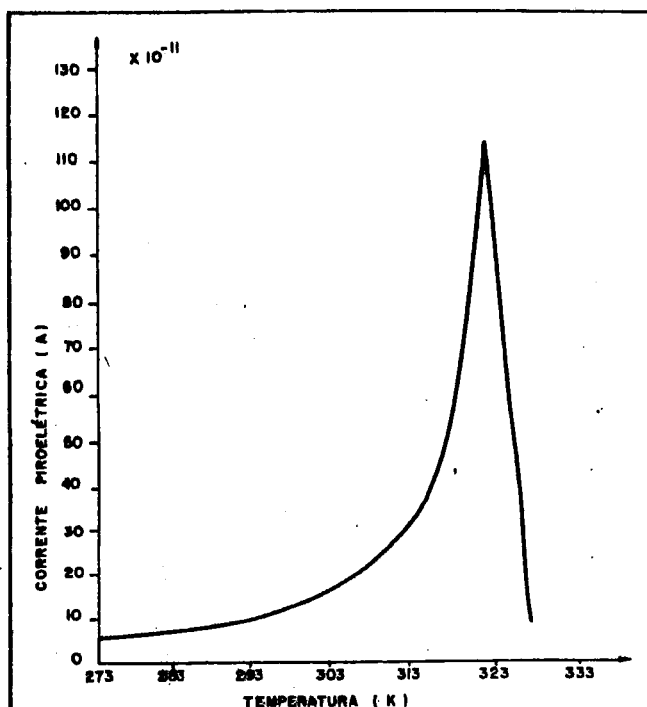


Figura 4: Variação da corrente piroelétrica com a temperatura

O coeficiente piroelétrico de um material é definido como sendo a variação da polarização espontânea com a temperatura [7]. Portanto, podemos escrever que:

$$p(T) = \frac{i(T)}{Ar} \quad (2)$$

onde r é a taxa de aquecimento, na qual a amostra é submetida. Como a variação da corrente piroelétrica com a temperatura pode ser determinada experimentalmente, podemos calcular a variação do coeficiente piroelétrico através da equação (2), como mostra a figura 5.

Protótipos de detectores de radiação infravermelha foram montados com o objetivo de verificar o comportamento dos cristais em situações reais de utilização. Para tanto, lâminas com a espessura de 0,013 cm foram clivadas e cortadas com serra diamantada para fornecer área útil de $0,03 \text{ cm}^2$. Eletrodos de prata de $0,014 \text{ cm}^2$ foram aplicados e o elemento sensível montado em um encapsulamento de transistor TO-33. Os dispositivos assim construídos mostraram uma responsividade em voltagem de 7,0 Volts/Watts na freqüência de modulação de 15 Hz, quando uma janela de KBr de 0,06 cm de espessura foi utilizada na montagem.

Tempo de resposta de 1mseg foi obtido, quando um resistor de carga de 10 ohm e um FET BFW11 atuaram com sistema "casador" de impedância.

Estes resultados mostram, fundamentalmente, que os cristais obtidos possuem um comportamento adequado para que possam ser utilizados com sucesso em qualquer dispositivo de detecção de radiação infravermelha.

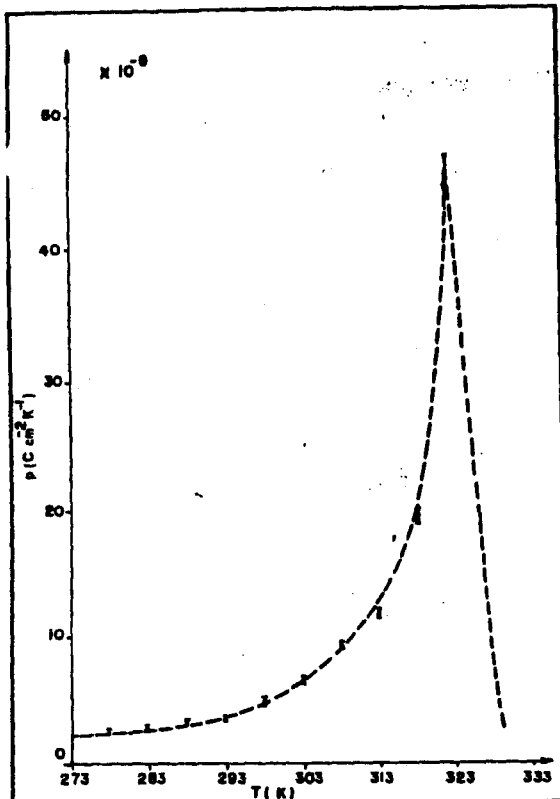


Figura 5: Variação do coeficiente piroelétrico com a temperatura

REFERÊNCIAS

- [1] Porter, S.G. - "Ferroelectrics", 33, 193-206, 1981
- [2] Hadui, A. - "Infrared Phys.", 27 (1), 17-23, 1987
- [3] Flecther, S.R.; Skapski, A.C. and Keve, E.T. "Ferroelectrics", 14, 775-787, 1976
- [4] Itok, K. & Mitsui, T. - "Ferroelectrics", 5, 235-51, 1973
- [5] Pandya, G.R. & Vejas, D.D. - J.Cryst.Growth, 50, 870-72, 1980

SUMMARY

We prepared large single crystals of triglycine sulphate (TGS) using the method of crystal growth from aqueous solution. The results showed a high optical and structural quality basic properties for the future development of infrared radiation detectors. Voltage responsivity and time responses of a detector prototype built with single crystals are presented.

De acordo com as políticas editoriais, este artigo não pode ser depositado em repositório de acesso aberto. Para acesso ao artigo completo entre em contato com o(a) autor(a) ou com o Serviço de Biblioteca e Informação IFSC - USP (bib@ifsc.usp.br)

ANDREETA, J. P.; HERNANDES, A. C.; GALLO, N. J. H. Growth and homogeneity of Cr⁺³ doped GdAlO₃ single crystals. **Materials Research Bulletin**, 1990, v.25, p. 51-56, Aug. 1990.

CAPÍTULO 7

TRABALHOS DE PESQUISA EM ANDAMENTO

VII. Trabalhos de pesquisa em andamento

Os trabalhos de pesquisa em andamento estão principalmente centrados no uso da radiação laser no desenvolvimento de materiais, seja mono ou policristalino. Também estamos determinando as características físicas de alguns minerais e procurando estabelecer uma metodologia para a reutilização dos resíduos.

- 1. Preparação e caracterização de fibras monocristalinas óxidas de compostos ABO_3 e ABO_4 (A= terras-raras; B= Al, V):** Corresponde ao trabalho parcial de doutorado do estudante Marcello Rubens Barsi Andreatta. O referido estudo encontra-se em fase de conclusão. Usando a técnica Laser Heated Pedestal Growth diversas fibras de GdAlO_3 e YAlO_3 puras e dopadas com Nd^{+3} , bem como de YVO_4 , LaVO_4 foram preparadas e caracterizadas opticamente. Dois dos mais importantes resultados alcançados foram a obtenção de emissão espontânea de luz em fibras de $\text{YAlO}_3\text{:Nd}^{+3}$ e o desenvolvimento de um modelo físico que descreve a distribuição de dopante nas fibras monocristalinas.

- 2. Solidificação direcional de compostos eutéticos de óxidos refratários usando o método de fusão a laser:** Corresponde ao trabalho parcial de doutorado da estudante Erika Regina Manoel Andreatta. Objetivamos realizar um estudo sistemático do processo de preparação de fibras eutéticas de compostos óxidos refratários do tipo $\text{Al}_2\text{O}_3/\text{GdAlO}_3$; $\text{ZrO}_2/\text{CaZrO}_3$; $\text{Eu}_2\text{O}_3/\text{EuAlO}_3$. O interesse por estes materiais tem-se acentuado com o desenvolvimento das diferentes formas de solidificação direcional que permitem obter estruturas orientadas. A microestrutura impede a progressão de trincas, aumentando assim o trabalho de fratura. A técnica de crescimento pedestal com aquecimento a laser está sendo utilizada na preparação desses compostos eutéticos.

- 3. Preparação de compostos do tipo AB_2O_6 (A=Mg e Zn; B = Nb e Ta) puros e dopados e a determinação de suas propriedades ópticas e dielétricas:** Corresponde ao trabalho parcial de doutorado da estudante Cynthia Regina Ferrari. Estamos realizando um estudo sistemático do processo de preparação de compostos da família columbita AB_2O_6 (A = Mg, Zn e B = Nb e Ta), na forma monocristalina, e a realização de sua caracterização física. Os materiais a serem pesquisados possuem entre si algumas características físico-químicas comuns, como por exemplo, a tendência em perder oxigênio em altas temperaturas e elevados pontos de fusão ($> 1400 ^\circ C$). O processo de oxidação-redução acredita-se ser similar ao do $LiNbO_3$, mas estudos mais detalhados ainda necessitam ser efetuados. A técnica Laser Heated Pedestal Growth está sendo usada na preparação das amostras cristalinas.
- 4. Desenvolvimento e sinterização rápida de materiais cerâmicos ferroelétricos via radiação laser:** Corresponde ao trabalho parcial de doutorado da estudante Zélia Soares Macedo. O referido estudo consiste em determinar as condições experimentais ótimas para a produção de cerâmicas ferroelétricas com microestrutura definida. O estudo das propriedades físicas relevantes de materiais ferroelétricos será efetuado, principalmente, por meio da técnica de espectroscopia de impedância. A possibilidade de se obter cerâmicas translúcidas de forma rápida e com microestrutura controlada definirá uma nova metodologia para o desenvolvimento de dispositivos do estado sólido.
- 5. Desenvolvimento e controle da cristalização em materiais vítreos com potencialidades para a optoeletrônica:** Corresponde ao trabalho parcial de mestrado do estudante André Luiz Martinez. O referido estudo está em fase final de conclusão. Os principais resultados alcançados foram a produção de materiais vítreos e vitro-cerâmicas de compostos óxidos e oxi-fluoretos. Particularmente, a produção de vitro-cerâmicas de $\beta-BaB_2O_4$ apresentaram o fenômeno de geração de segundo harmônico (GSH). O controle do processo de

cristalização superficial e os resultados de GSH levou-nos a manter essa linha de pesquisa e estudar novos materiais que apresentam, em sua fase cristalina, importantes aplicações em óptica.

6. Cristalização de materiais vítreos usando radiação laser:

Corresponde ao trabalho parcial de mestrado do estudante Fábio Ribeiro Dias. Esse estudo é uma continuação do trabalho de pesquisa iniciado pelo estudante André Luiz Martinez. O estudante Fábio ingressou no programa de pós-graduação nesse primeiro semestre corrente. A fundamental diferença desse estudo com o realizado anteriormente está no uso da radiação laser para a realização do processo de cristalização. O estudo da interação laser/material vítreo, bem como do fenômeno de cristalização em condições de resfriamentos rápidos será muito importante para a definição do uso do laser como uma ferramenta para a produção de vitro-cerâmicas.

7. Simulação numérica da propagação de calor em materiais cerâmicos sinterizados via radiação laser: Corresponde ao trabalho parcial de mestrado da estudante Cristiane Nascimento Santos.

A estudante ingressou nesse semestre no programa de mestrado do Instituto de Física, sub-área Física Aplicada. O estudo refere-se a realização da simulação computacional dos perfis de temperatura em corpos cerâmicos irradiados com luz laser e a procura de uma descrição da evolução da onda térmica no material. Numa última etapa, tentar relacionar a evolução da energia térmica com o processo de sinterização.

8. Preparação de cerâmica, caracterização elétrica e dielétrica por espectroscopia de impedância da turmalina negra: Esse estudo refere-se ao trabalho de pós-doutoramento que está sendo realizado pela Dra. Silvana Lanfredi. O objetivo principal desse estudo é determinar a condutividade elétrica e a constante dielétrica de cerâmica produzidas a partir de resíduos de turmalina negra.

Os demais trabalhos que se encontram em andamento, sob minha supervisão e orientação, estão relacionados a formação de estudantes de Iniciação Científica e a projetos de desenvolvimento em parceria com empresas.

Os estudantes de iniciação científica, **Paula S. Saia (IFSC), Fernanda C. Camargo (IFSC), Letícia Soldi Alves (EESC), José Ezequiel de Souza (IFSC) e Ronaldo Regobello (EESC)** estão realizando trabalhos de processamento cerâmico e caracterização de minerais de granada e esmeralda, a exceção da estudante Fernanda, aluna do curso de licenciatura noturno do IFSC, que está trabalhando na sistematização de um texto sobre materiais vítreos a ser usado por estudantes do 2º Grau.

Os trabalhos em parceria com empresas realizados dentro do Programa **πUSP** referem-se ao desenvolvimento de sistema de refrigeração de água para bebedouros domésticos a base do efeito Peltier, a viabilização de um sistema de visão artificial aplicado a objetos em movimento, a otimização da produção de materiais vítreos a partir de resíduos de minerais e a execução de pesquisa e análise de cobre e algumas ligas, visando o controle da microestrutura. Esses trabalhos são realizados nos laboratórios de nosso grupo de pesquisa, sem a participação de formação de estudantes de pós-graduação.

CAPÍTULO 8

CONCLUSÕES

VIII. Conclusões

Os estudos e o desenvolvimento de materiais cristalinos, por nós realizados, nos possibilitaram o entendimento de alguns importantes aspectos microscópicos relativos aos processos de crescimento de cristais, a partir da fase líquida, principalmente dos compostos óxidos. Alterações na forma da interface de cristalização associadas com o padrão de fluxos convectivos, segregação de impurezas e a precipitação de fases eutéticas devido ao superresfriamento constitucional são alguns desses aspectos estudados e que foram abordados nesse trabalho. Como consequência desses estudos, nos foi possível compatibilizar o entendimento teórico dos processos de preparação com a produção de amostras monocristalinas homogêneas e de alta qualidade estrutural, que são de enorme importância para os pesquisadores brasileiros de física do estado sólido.

O domínio dos parâmetros macroscópicos dos processos de preparação de monocristais, especialmente aos relacionados com a técnica de solidificação direcional com aquecimento a laser, permitiu ao Grupo de Pesquisa, sob nossa orientação, consolidar-se como um dos mais importantes da América Latina. Além disso, esses conhecimentos adquiridos nos possibilitaram a abrir novas linhas de pesquisas com o objetivo de estudar os fenômenos de cristalização e de sinterização de materiais cerâmicos sob irradiação de luz laser, desenvolvido pioneiramente em nossos laboratórios.